

A STUDY OF MIXED-MODE DYNAMIC FRACTURE IN ADVANCED PARTICULATE
COMPOSITES BY OPTICAL INTERFEROMETRY, DIGITAL IMAGE
CORRELATION AND FINITE ELEMENT METHODS

Except where reference is made to the work of others, the work described in this dissertation is my own or was done in collaboration with my advisory committee. This dissertation does not include proprietary or classified information.

Madhusudhana S. Kirugulige

Certificate of Approval:

Thomas S. Denney Jr.
Professor
Electrical and Computer Engineering

Hareesh V. Tippur, Chair
Alumni Professor
Mechanical Engineering

Jeffrey C. Suhling
Quina Distinguished Professor
Mechanical Engineering

Winfred A. Foster
Professor
Aerospace Engineering

Joe F. Pittman
Interim Dean, Graduate School

A STUDY OF MIXED-MODE DYNAMIC FRACTURE IN ADVANCED PARTICULATE
COMPOSITES BY OPTICAL INTERFEROMETRY, DIGITAL IMAGE
CORRELATION AND FINITE ELEMENT METHODS

Madhusudhana S. Kirugulige

A Dissertation

Submitted to

the Graduate Faculty of

Auburn University

in Partial Fulfillment of the

Requirements for the

Degree of

Doctor of Philosophy

Auburn, Alabama
August 04, 2007

A STUDY OF MIXED-MODE DYNAMIC FRACTURE IN ADVANCED PARTICULATE
COMPOSITES BY OPTICAL INTERFEROMETRY, DIGITAL IMAGE
CORRELATION AND FINITE ELEMENT METHODS

Madhusudhana S. Kirugulige

Permission is granted to Auburn University to make copies of this dissertation at its discretion, upon the request of individuals or institutions and at their expense. The author reserves all publication rights.

Signature of Author

Date of Graduation

VITA

Madhusudhana Kirugulige was born on January 25, 1975 in Shimoga, India. He graduated with Bachelor of Engineering degree in Mechanical Engineering major from M. S. Ramaiah Institute of Technology, Bangalore University, Bangalore, India in 1997. In 1998, he joined Indian Institute of Science, Bangalore, India for masters program in Mechanical Engineering. He was awarded Master of Science degree for his thesis entitled “Experimental and Numerical Investigations of Stable Crack Propagation in Adhesively Bonded Joints ”in 2001. Following graduation, he worked in two private sector companies, Turbotech Precision Engineering Private Limited, Bangalore and General Electric Global Research Center in Bangalore. In the former he was involved in design, analysis and testing of steam turbines, gas turbines and centrifugal compressors. In the latter, he worked on finite element modeling of entire gas turbine engine casing in order to evaluate running clearance between stator and rotor. He joined Auburn University in spring 2003 as a Ph.D. candidate in Mechanical Engineering where he conducted research on mixed-mode dynamic fracture of novel materials using optical interferometry, digital image correlation and finite element methods.

DISSERTATION ABSTRACT

A STUDY OF MIXED-MODE DYNAMIC FRACTURE IN ADVANCED PARTICULATE
COMPOSITES BY OPTICAL INTERFEROMETRY, DIGITAL IMAGE
CORRELATION AND FINITE ELEMENT METHODS

Madhusudhana S. Kirugulige

Doctor of Philosophy, August 04, 2007
(M.S., Indian Institute of Science, Bangalore, India, 2001)
(B.E., Bangalore University, Bangalore, India, 1997)

204 Typed Pages

Directed by Hareesh V. Tippur

Understanding the fracture mechanics of materials under stress wave loading is essential for impact resistant design of structures. In this context, mixed-mode dynamic fracture behavior of two-phase composites - a functionally graded material (FGM) and a syntactic structural foam are investigated experimentally and numerically. FGMs are macroscopically nonhomogeneous engineered materials with spatially varying volume fraction of the constituents. They are used as thermal barrier coatings in high temperature components, as core materials in sandwich structures, as inter layers in micro-electronic packages, to name a few. Syntactic foams are homogeneous buoyant materials used in naval/marine applications as well as for energy dissipation in military and industrial environments. Catastrophic failure in these materials is often observed to occur in a mixed-mode fashion involving a combination of tensile and shear fractures. Real-time and full-field measurement of crack tip deformations in these circumstances is rather challenging because the events typically last only a couple of hundred microseconds, and need optical tools coupled with ultra-high

speed imaging devices to understand the associated failure mechanisms. To date very few methods are available for performing direct measurements of crack tip fields. This dissertation aims to address these by studying the dynamic fracture behavior of such novel materials by developing suitable measurement and modeling tools.

The first part of this research extends the optical method of Coherent Gradient Sensing (CGS) to the study of mixed-mode dynamic fracture behavior of functionally graded materials. FGMs studied are the ones with a continuously varying volume fraction of ceramic filler particles in a polymer matrix having edge cracks initially along the property gradient and subjected to impact loading. The mixed-mode loading is generated by loading samples eccentrically relative to the initial crack plane. CGS and high-speed photography are used to map transient crack tip deformations. Two configurations, one with a crack on the stiffer side of a graded sheet and the second with a crack on the compliant side, are examined experimentally. Differences in both pre- and post-crack initiation behaviors are observed in terms of crack initiation time, crack path, crack speed and stress intensity factor histories. A crack kinks by a much larger angle when it originates from the stiffer side of the FGM compared to the compliant side. Crack speeds, however, are higher in the latter configuration by nearly 100 m/sec. Prevailing crack tip field descriptions do successfully predict the observed crack path differences.

In the second part of this work, the method of digital image correlation is developed to study transient deformations associated with rapid mixed-mode crack growth in materials. Edge cracked polymer beams and syntactic foam samples are studied under low-velocity impact loading conditions. Decorated random speckle patterns in the crack tip vicinity are recorded using an ultra high-speed CCD camera at framing rates of 200,000 frames

per second. A three-step digital image correlation technique is developed and implemented in a MATLAB environment for evaluating crack opening/sliding displacements and the associated strains. Using this approach, the entire crack tip deformation history, from the time of impact to complete fracture, is mapped successfully. Over-deterministic least-squares analyses of crack tip displacements are performed to extract dynamic stress intensity factor (SIF) histories. The current work being the first of its kind using a rotating mirror type multi-channel high-speed digital camera system, calibration tests and procedures are established by carrying out a series of benchmark experiments. The accuracy of measured displacements is in the range 2 to 6% of a pixel (0.6 to 1.8 μm) and that of the dominant strain is about 150-300 micro strains.

In the last part, finite element modeling of mixed-mode dynamic crack growth in FGM using cohesive element formulations is performed. The formation of new surfaces is accomplished by using bilinear tensile and shear traction-separation laws. A user-defined subroutine is developed and linked with ABAQUS implicit procedure. The spatial variations of material properties are incorporated into the continuum elements by performing a thermal analysis first and then by applying temperature dependant material properties to the model. Measured mode-I crack initiation toughness data from homogeneous samples of various volume fractions of the filler are used to introduce spatial variation of cohesive element properties to the model. The simulated crack paths are in agreement with the experimental ones. The computed results prior to crack initiation show the presence of larger negative constraining stresses (T -stresses) near the crack tip when the crack is situated on the compliant side of the FGM. The simulations reveal that more energy is dissipated when the crack is situated on the compliant side of the sample compared to when it is on the

stiffer side. This is in consistent with the higher crack speeds observed when the crack initiates from the complaint side.

ACKNOWLEDGMENTS

I would like to thank my research supervisor, Dr. Hareesh V. Tippur for his valuable guidance, constant encouragement and advice extended throughout the research work of this thesis. I am grateful to him for providing excellent experimental and computational facilities to work on and encouraging me to present the research work at various forums. Special thanks to Dr. Thomas S. Denney for his valuable help and guidance with image processing issues of this research work. Thanks to Dr. Jeffrey C. Suhling and Dr. Winfred A. Foster for having kindly agreed to serve on my committee. My sincere thanks to thank Dr. Michael J. Stallings for agreeing to become the external reader for my thesis. Thanks are also due to Dr. Michael E. Miller of Auburn University Research Instrumentation Facility (AURIF) department for allowing me to use his vacuum evaporator. I would like to thank US Army Research Office (grants # W911NF-04-10257, DAAD19-02-1-0126 and DAAD19-01-1-0745) and for extending financial and equipment support for this work.

I would like to acknowledge my colleagues and friends in Auburn for the memorable and enjoyable time I spent with them. I had very good time in the lab with Rajesh, Mike, Piyush, Taylor, Dong and Rahul. Especially the lively atmosphere of the lab in the presence of Piyush, Rajesh and Taylor was really enjoyable.

Finally, the support, encouragement and love I had from my wife Asha Dixit is something invaluable. I dedicate this work to her.

Style manual or journal used Journal of Approximation Theory (together with the style known as “aums”). Bibliography follows van Leunen’s *A Handbook for Scholars*.

Computer software used The document preparation package T_EX (specifically L^AT_EX) together with the departmental style-file `aums.sty`.

TABLE OF CONTENTS

LIST OF FIGURES		xiv
LIST OF TABLES		xxi
1	INTRODUCTION	1
1.1	Motivation and Literature Review	5
1.1.1	Review of failure characterization of FGM	7
1.1.2	Review of optical methods to study fracture	8
1.1.3	Review of numerical methods to simulate fracture	10
1.2	Objectives	13
1.3	Organization of Dissertation	14
2	EXPERIMENTAL METHOD OF CGS TO STUDY DYNAMIC FRACTURE	17
2.1	Optical set-up	17
2.2	Working principle of CGS	18
2.3	Experimental procedure	23
2.4	Extraction of stress intensity factors from interferograms	24
2.4.1	Pre-crack initiation period	25
2.4.2	Post-crack initiation period	26
2.5	Computation of crack speed	29
2.6	Crack tip fields in FGM with linear material property variation	30
2.6.1	Crack along the direction of property gradation	30
2.6.2	Crack inclined to the direction of property gradation	32
2.7	Extraction of SIFs with difference formulation	33
3	MIXED-MODE DYNAMIC FRACTURE OF FGM USING CGS	35
3.1	Material Preparation	35
3.2	Material characterization	36
3.3	Specimen surface preparation	38
3.4	Results	39
3.4.1	Experimental details	40
3.4.2	Crack growth and crack speed histories	43
3.4.3	Mixed-mode stress intensity factor histories	44
3.4.4	Initial crack path prediction	50
3.5	Mixed-mode SIF history from FGM crack tip fields	52

4	THE METHOD OF DIGITAL IMAGE CORRELATION	56
4.1	The approach	56
4.1.1	Initial estimation of displacements (Step-1)	57
4.1.2	Refining displacements (Step-2)	59
4.1.3	Smoothing of displacements and estimation of strains (Step-3)	60
4.2	Static experiments	62
4.3	Dynamic experimental set-up	67
4.4	High-speed camera calibration	69
4.5	Benchmark experiments for high-speed camera	74
4.5.1	Intensity variability test	76
4.5.2	Translation test	79
4.5.3	Rotation test	86
4.6	Flash lamp light characteristics	87
5	DYNAMIC FRACTURE STUDIES USING DIC METHOD	91
5.1	Sample preparation	91
5.2	Experimental procedure	93
5.3	Finite element simulations	94
5.3.1	Mixed-mode fracture of syntactic foam	94
5.3.2	Mode-I fracture of epoxy	96
5.4	Results - Mixed-mode dynamic fracture of syntactic foam	97
5.4.1	Extraction of stress intensity factors	99
5.4.2	Estimation of strains	105
5.5	Results - Mode-I dynamic fracture of epoxy	107
5.5.1	Extraction of stress intensity factors	109
5.5.2	Estimation of strains	113
6	NUMERICAL PROCEDURES FOR MODELING DYNAMIC FRACTURE IN FGM	116
6.1	Elastodynamic governing equations	116
6.2	Implicit integration of dynamic equations in ABAQUS	119
6.3	Formulation of an element in ABAQUS	120
6.4	Cohesive element formulation	121
6.4.1	Exponential traction-separation law	123
6.4.2	Bilinear traction-separation law	126
6.5	Implementation details	129
6.6	Implicit dynamic scheme and time step control	130
7	NUMERICAL SIMULATION OF MODE-I AND MIXED-MODE DYNAMIC FRACTURE IN FGM	133
7.1	Modeling aspects	133
7.2	Application graded material properties to continuum elements	136
7.3	Application of material properties to cohesive elements	137

7.4	Results	140
7.4.1	Energy computations	140
7.4.2	Effect of the initial slope of traction-separation law	141
7.4.3	Crack path history	145
7.4.4	T -stress history	148
8	CONCLUSIONS	150
8.1	Future Directions	154
	BIBLIOGRAPHY	156
	APPENDICES	164
A	A NOTE ON ACCURACY OF STRAINS AND TIME RESOLVED DISPLACEMENTS	164
A.1	A note on accuracy of strains	164
A.2	Time resolved displacements	165
B	COMPUTATION OF STIFFNESS COEFFICIENTS IN TRACTION-SEPARATION LAWS	170
B.1	Exponential traction-separation law	170
B.2	Bilinear traction-separation law	173
C	FINITE ELEMENT SIMULATION OF MODE-I DYNAMIC FRACTURE OF FGM	175
C.0.1	Material preparation and characterization	175
C.0.2	Experimental results	177
C.0.3	Modeling details	180
C.0.4	Finite element results	180

LIST OF FIGURES

1.1	Schematic of a functionally graded material showing variation in elastic, failure and fracture properties when constituent volume fraction is varied. . . .	2
1.2	Applications of syntactic foams, (a) deepwater insulated oil and gas pipelines (Courtesy: Cuminc corporation), (b) buoyancy foam for deep underwater floatation (Courtesy: Syntech materials, Inc.) and (c) Impact resistant sandwich structures (Courtesy: Goodrich Corporation)	3
1.3	Schematic illustrating modes of fracture	4
1.4	Mixed-mode dynamic fracture evidences, (a) environmentally assisted crack propagation from leading edge to the inside cooling surface of a gas turbine blade (Courtesy: Gas Turbine technology) and (b) Concrete damage after missile impact (Courtesy: Dept. of Civil and Structural Engineering, University of Sheffield, UK.)	5
2.1	Schematic for reflection-mode CGS set-up with a high-speed camera	18
2.2	Working principle of CGS, (a) Diffraction of a collimated beam through two parallel Ronchi gratings, (b) undeformed object wave front and (c) deformed object wave front.	19
2.3	Global and local crack tip coordinate systems for (a) stationary crack and (b) propagating crack	25
2.4	(a) Schematic of FGM sample with linear material property variation, (b) elastic modulus variation in graded samples (broken line denotes the crack tip location)	31
3.1	Schematic of FGM sample used in experiments	36
3.2	Variation of longitudinal and shear wave speeds along the width of the sample	37
3.3	Variation of elastic modulus and mass density along the width of the sample	39
3.4	Variation of dynamic initiation toughness (impact velocity = 5.4 m/sec) with Elastic modulus. (Broken line is a trend line)	40

3.5	Selected CGS interferograms representing contours of $\delta w/\delta x$ in FGM and homogeneous samples. (The vertical line is at 10 mm from the crack). (a) crack on the compliant side and (b) crack on the stiffer side (c) homogeneous (Plexiglas) sample.	42
3.6	Crack growth behavior in FGM samples under mixed-mode dynamic loading. (a) Crack growth history, (b) normalized crack speed history. (V_R : local Rayleigh wave speed)	43
3.7	Mixed-mode dynamic stress intensity factor histories (impact velocity=5.2 m/sec). (Circles: $E_1 < E_2$, triangles: $E_1 > E_2$). (Time base is altered such that $t - t_i = 0$ corresponds to crack initiation)	45
3.8	Photographs showing multiple fractured specimens (right half) demonstrating experimental repeatability (a) FGM with a crack on the compliant side ($E_1 < E_2$), (b) FGM with a crack on the stiffer side ($E_1 > E_2$).	47
3.9	Photographs showing fractured specimens for (a) FGM with a crack on the compliant side ($E_1 < E_2$), (b) FGM with a crack on the stiffer side ($E_1 > E_2$) and (c) a homogeneous specimen. Impact point is indicated by letter 'I' and initial crack tip by letter 'C'	48
3.10	Crack growth behavior in FGM samples under mixed-mode dynamic loading. (a) Crack growth history, (b) normalized crack speed history. (V_R : local Rayleigh wave speed)	49
3.11	Stress intensity factors extracted from CGS interferograms by performing over-deterministic least-squares analysis on difference formulation of CGS governing equation formulated by using crack tip stress fields obtained for FGM with linear elastic modulus variation.	54
3.12	The quality of least-squares fit (plots of synthetic contours generated from Eq. 2.34 superimposed on collected data points) for (a) $E_1 < E_2$ ($t - t_i = 20 \mu\text{s}$) and (b) $E_1 > E_2$ ($t - t_i = -20 \mu\text{s}$).	55
4.1	(a) Undeformed and deformed sub-images chosen from images before and after deformation, respectively and (b) typical plot of impulse response $G_{\alpha_p}(k_x - u, k_y - v)$ generated from cross-correlation between two sub-images.	58
4.2	(a) Schematic of the experimental set-up for static experiment, (b) specimen and loading details	63
4.3	Photograph of the static experimental set-up	64

4.4	In-plane displacements obtained from Step-1, 2 and 3 of the image correlation process. The interval between contours is $7 \mu\text{m}$	65
4.5	Static experimental results. (a) and (c) u -displacement (mm) from DIC and FEA, (b) and (d) ϵ_{xx} (μ -strain) from DIC and FEA, (e) and (f) u -displacement and ϵ_{xx} -strain at section AA and BB . Rigid body displacements have been subtracted out both in (a) and (c)	66
4.6	Schematic of the dynamic experimental set-up	67
4.7	Photograph of the dynamic experimental set-up	68
4.8	Optical schematic of cordin-550 camera: M_1, M_2, M_3, M_4, M_5 are mirrors; R_1 and R_2 are relay lenses; r_1, r_2, \dots, r_{32} are relay lenses for CCDs; c_1, c_2, \dots, c_{32} are CCD sensors	70
4.9	(a) Image of the 5×5 dot pattern template used for calibration experiment and (b) Inverted binary image of the template in order to find the control points	72
4.10	Mean and standard deviations of intensity values of images acquired in total darkness (with lens cap on). Images were recorded at 50,000 frames per second in experiment 1 and at 200,000 frames per second in experiment 2.	77
4.11	Experimental set-up for conducting translation test for high-speed digital camera	79
4.12	Translation test results for $D=400$ mm and 200 mm (see Fig. 4.8. (a) mean and (b) standard deviations of u - and v - displacement fields for X - and Y - translations of $\sim 60 \pm 2\mu\text{m}$ (c) mean and (d) standard deviations of u - and v -displacement fields for X - and Y - translations of $300 \pm 2\mu\text{m}$. Magnification = $35.6 \mu\text{m}/\text{pixel}$ for $D=400$ mm and $27 \mu\text{m}/\text{pixel}$ for $D=200$ mm.	82
4.13	Translation test results for $D = 400$ mm (see Fig. 4.8) and out-of-plane displacement (w) = $30 \mu\text{m}$. (a) mean and (b) standard deviation of u - and v -displacement field.	84
4.14	Estimated full-field quantity ω_{xy} from one pair of the images taken from camera # 1 in a rotation experiment (Imposed rotation = 0.0056 ± 0.00035 radians).	87
4.15	Results from rotation test (applied rotation = 0.0056 ± 0.00035 radians). (a) mean and (c) standard deviation of rotation field estimated from image correlation. (b) mean (d) standard deviations of in-plane strains estimated (ideally these strains need to be zeros).	88

4.16	Photo detector output proportional to flash lamp light intensity, A_1 , A_2 and B_1 , B_2 are two repeated acquisitions when photodiode was placed one inch away in the plane perpendicular to optical axis of the camera.	89
5.1	Specimen configuration for (a) mixed-mode test of syntactic foam and (b) mode-I test of epoxy. Impactor force history and support reaction histories recorded by Instron Dynatup 9250 HV drop tower for (c) mixed-mode experiment and (d) mode-I experiment. The sample dimensions are $a = 10$ mm, $W = 50$ mm, $S = 25.4$ mm, $L = 200$ mm, $B = 8.75$ mm, Impact velocities, $V_1 = 4.5$ m/sec and $V_2 = 4.0$ m/sec.	92
5.2	Finite element mesh used for elsto-dynamic finite element analysis of (a) mixed-mode problem and (b) mode-I problem.	95
5.3	Acquired speckle images of 31×31 mm ² region at various times instants. (Crack tip location is shown by an arrow.)	98
5.4	Crack growth behavior in syntactic foam sample under mixed-mode dynamic loading.	99
5.5	Crack opening and sliding displacements (in mm) for pre- and post-crack initiation instants. (a) v -displacement and (c) u -displacement before crack initiation (at $t=150 \mu s$); (b) v -displacement and (d) u -displacement after crack initiation ($t=220 \mu s$). Crack initiation time $\sim 175 \mu s$. (A large rigid body displacement can be seen in (c) an (d) due to movement of the sample.	100
5.6	Stress intensity factors extracted from displacement fields obtained from image correlation. SIF history obtained from finite element simulation up to crack initiation is also shown.	104
5.7	The mode-mixity, ψ obtained from experiments and finite element simulation. The broken line corresponds to crack initiation time.	105
5.8	Crack tip normal strains (in micro strains) at $t = 150 \mu s$. (a) from experiment and (b) From FEA. Crack initiation time = $175 \mu s$	107
5.9	Acquired speckle images of 31×31 mm ² region at various times instances. Current crack tip location is shown by an arrow.	108
5.10	Crack growth behavior in epoxy sample under mode-I dynamic loading. Crack length history and crack speed history	109

5.11	Crack opening and sliding displacements (in μm) for pre- and post-crack initiation instants. (a) v -displacement and (c) u -displacement before crack initiation (at $t = 120 \mu\text{s}$); (b) v -displacement and (d) u -displacement after crack initiation ($t = 151 \mu\text{s}$). Crack initiation time $\sim 133 \mu\text{s}$	110
5.12	Examples showing quality of least-squares fit of displacement data; Crack opening displacement field (μm) obtained from DIC and synthetic contours for (a) $t = 124 \mu\text{s}$ (before crack initiation) and (b) $t = 151 \mu\text{s}$ (after crack initiation). Crack initiation time = $133 \mu\text{s}$	112
5.13	Stress intensity factors extracted from displacement field obtained from image correlation. SIF history obtained from finite element simulation up to crack initiation is also shown.	113
5.14	Crack tip in-plane constraint, β obtained from experiments and finite element simulation. The broken line corresponds to crack initiation time.	114
5.15	Crack tip normal strains (in micro strains) for pre- and post-crack initiation. Normal strain ϵ_{yy} at (a) $t = 120 \mu\text{s}$ and (b) at $t = 151 \mu\text{s}$ and (c) ϵ_{yy} from finite element analysis at $t = 120 \mu\text{s}$. Crack initiation time = $133 \mu\text{s}$	115
6.1	(a) Undeformed and (b) deformed finite element mesh near a notch tip, (c) Schematic showing separation of nodes in a cohesive element and (d) local and global coordinate system used for a cohesive element.	122
6.2	Exponential traction-separation law showing uncoupled loading: variations of (a) pure normal traction with normal separation and (b) pure tangential traction with tangential separation.	125
6.3	Exponential traction-separation law showing coupled loading: variations of (a) normal traction and (b) tangential traction.	126
6.4	Prescribed bilinear traction-separation law for (a) pure normal traction versus normal separation and (b) pure tangential traction versus tangential separation.	128
6.5	Steps involved in implementing a cohesive element as user-defined element in ABAQUS	131
7.1	(a) Overall view of the finite element mesh used for the analysis (b) Magnified view of mesh showing region 1 and region 2 (c) Enlarged view of the mesh at the interface where the elements from region 1 and region 2 meet. .	134

7.2	(a) Nodal temperature results from thermal analysis, (b) magnified view of the cohesive element region.	138
7.3	Mixed mode dynamic fracture of plxiglas sample. (a) Crack path observed in experiments and (b) initial crack path from finite element simulations . .	139
7.4	Evolution of different energy components in dynamic simulation for both FGM configurations: (a) kinetic energy and strain energy and (b) energy dissipated by cohesive elements	142
7.5	Effect of initial slope of the traction-separation law on (a) displacement and (b) on stress results in elastodynamic simulation	144
7.6	Snapshots of σ_{yy} stress field at two different time instants, (a) 120 μs and (b) 150 μs for $E_1 < E_2$ (crack initiation time = 129 μs), and (c) 120 μs and (d) 168 μs for $E_1 > E_2$ (crack initiation time = 130 μs).	146
7.7	Snapshots of u_y displacement field at two different time instants, (a) 120 μs and (b) 150 μs for $E_1 < E_2$ (crack initiation time = 129 μs), and (c) 120 μs and (d) 168 μs for $E_1 > E_2$ (crack initiation time = 130 μs).	147
7.8	Crack growth behavior in FGM sample under mixed-mode loading. Absolute crack length history from (a) experiments and (b) finite element simulations, t_i is crack initiation time ($t_i = 155 \mu s$ for $E_1 < E_2$ and 145 μs for $E_1 > E_2$ in experiments, $t_i \sim 130 \mu s$ for both $E_1 < E_2$ and $E_1 > E_2$ in simulations).	148
7.9	(a) Variation of apparent T -stress with crack length at certain time instant before crack initiation (b) T -stress history up to crack initiation for $E_1 < E_2$ and $E_1 > E_2$	149
A.1	Results of benchmark experiment conducted to estimate the accuracy of displacements and strains. (a) full-field u -displacement between image 1 and image 2 before deforming image 2 (ideally u -displacement should be zero). (b) u -displacement after applying a constant strain to image 2 but before smoothing, (c) u -displacement after smoothing and (d) normal strain after stretching image 2 uniformly.	166
A.2	Time resolved crack opening displacements for image # 1 to 12. Time at which each image was acquired after impact, is indicated above each figure. The interval between each contour is 3.5 μm	167
A.3	Time resolved crack opening displacements for image # 13 to 24. Time at which each image was acquired after impact, is indicated above each figure. The interval between each contour is 3.5 μm	168

A.4	Time resolved crack opening displacements for mixed-mode dynamic test, image # 25 to 32. Time at which each image was acquired after the impact, is indicated above each figure. The interval between each contour is $3.5 \mu\text{m}$.	169
B.1	Reversible and irreversible unloading	171
C.1	(a) Schematic of the FGM specimen, (b) Material properties variation along the width of the sample and (c) Variation of dynamic crack initiation toughness along the width of the sample.	178
C.2	Selected CGS interferograms representing contours of $\delta w/\delta x$ in functionally graded epoxy syntactic foam sheet impact loaded on the edge opposing the crack tip. (The vertical line is at a distance of 10 mm from the crack.) (a) Crack on the compliant side $E_1 < E_2$, (b) crack on the stiffer side $E_1 > E_2$. Fringe sensitivity $\sim 0.015^\circ$ /fringe.	179
C.3	Finite element mesh used for the analysis	181
C.4	Snapshots of σ_{yy} stress field at two different time instants, (a) $85 \mu\text{s}$ and (b) $125 \mu\text{s}$ for $E_1 < E_2$ (crack initiation time = $106 \mu\text{s}$), and (c) $105 \mu\text{s}$ and (d) $145 \mu\text{s}$ for $E_1 > E_2$ (crack initiation time = $127 \mu\text{s}$).	182
C.5	Crack growth behavior in syntactic foam FGM samples under mode-I loading. absolute crack length history from (a) experiments and (b) finite element simulations.	183
C.6	Evolution of various energies in mode-I dynamic simulation for both FGM configurations: (a) kinetic energy and strain energy and (b) energy dissipated by cohesive elements	183

LIST OF TABLES

3.1	Nominal bulk properties of the constituent materials	35
3.2	Predicted crack kink angle based on estimated SIF data from CGS interferograms before crack initiation	51
3.3	Observed crack kink angle from three CGS interferograms just after crack initiation	51
4.1	Alignment differences between individual optical channels of Cordin-550 camera; Stretch, rotation and translations of different images with respect to the image taken by camera # 09	75
4.2	Gray scale values at a particular pixel in five repeated sets of images of speckle pattern acquired at 200,000 frames second. Note the repeatability of the gray scale values between different sets of images.	78
4.3	Details of translation tests: Six sets of 32 images were recorded in each configuration. In Configuration-2, the camera was kept twice as close as in Configuration-1.	81
4.4	Mean and standard deviations of in-plane strain fields estimated from measured displacements in translation test	85

CHAPTER 1

INTRODUCTION

Over the last two decades, there has been an increasing demand for stiffer, stronger, light-weight, energy absorbing materials. Aerospace applications have placed some of the stringent requirements on the performance of the materials used in space planes and re-entry vehicles. One of them is to withstand large stress and/or thermal gradients over a small spatial dimension. For example, large temperature gradients in re-entry vehicles generate enormous amount of thermal stresses. This is true with parts exposed to high temperatures in gas turbines and IC engines as well. They are traditionally made by plasma spraying parts [1] made of nickel based alloys using thermal barrier coatings (TBC). These conventional TBCs suffer in terms of durability due to their poor bond strength, oxidation/corrosion resistance, and delamination or spallation. Therefore a new class of materials called functionally graded materials (FGM) having gradual compositional variation from heat resistant ceramic to fracture resistant metals have emerged as potential replacements for discretely layered conventional TBCs. They are manufactured by continuously varying the volume fraction of constituent phases along a spatial direction. Other applications of FGM include surface hardened tribological surfaces, impact resistant structures for armors and ballistics, interlayers in microelectronic and optoelectronic components, heat shields in rockets, to cite a few. Manufacturing methods for FGM have also been evolving over the recent years. The processing techniques such as chemical and physical vapor deposition, powder processing, infiltration techniques, buoyancy assisted casting, and diffusion are commonly used for producing FGM. The study of dynamic failure of FGM becomes important because many of

the aforementioned applications involve dynamic loading including mechanical shock and impact. Figure 1.1 shows schematic of the FGM sample prepared using gravity assisted casting.



Figure 1.1: Schematic of a functionally graded material showing variation in elastic, failure and fracture properties when constituent volume fraction is varied.

There has been steady increase in the usage of sandwich composites in aerospace, marine, transportation and packaging industries. The sandwich composites are made by attaching two thin plates called skin or face sheets to a thick and light-weight material called the core. Syntactic foams (polymers filled with thin walled hollow microballoons) have gained popularity as core materials in sandwich structures due their high energy absorption capability, compressive strength and low moisture absorption. Syntactic foams are also used in a variety of other applications such as buoyancy modules in boat hulls, structural components in helicopters and airplanes, antenna assemblies, thermal insulators in oil and gas industries, to name a few (see Fig. 1.2). Syntactic foams are particulate composites manufactured by dispersing prefabricated microballoons in a matrix material. The porosity in these materials results in lower density and superior thermal, dielectric, fire resistant, hygroscopic properties and sometimes radar or sonar transparency. Syntactic foams can be tailored to suit a particular application by selecting a wide range of microballoons of

different sizes (hollow glass micro spheres, carbon or polymer microballoons, cenospheres, etc.) along with any metallic, polymeric or ceramic matrix material. Since one of the main functions of a syntactic foam is to absorb energy to withstand impact and shock loading, it is important to study the dynamic failure behavior of these materials.

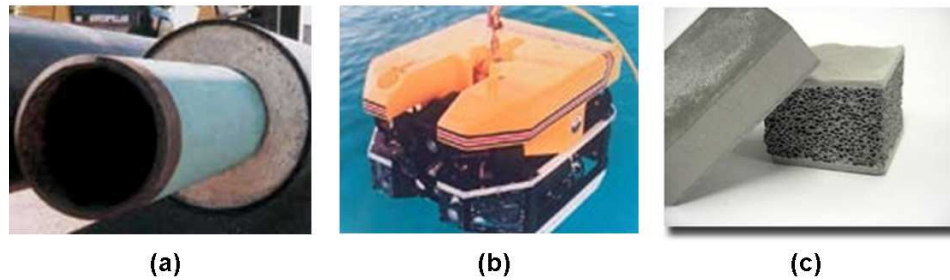


Figure 1.2: Applications of syntactic foams, **(a)** deepwater insulated oil and gas pipelines (Courtesy: Cuming corporation), **(b)** buoyancy foam for deep underwater floatation (Courtesy: Syntech materials, Inc.) and **(c)** Impact resistant sandwich structures (Courtesy: Goodrich Corporation)

The crack initiation and propagation under transient dynamic loading occurs in many engineering applications. Pressure induced shocks in reactor vessels, failure of metallic armor by projectile impact, blast loading in an aircraft are few examples. Although quasi-static fracture is fairly well understood theoretically as well as experimentally [2, 3], many issues still remain unresolved in the area of dynamic fracture of materials in general and heterogeneous materials in particular. A dynamic fracture event can be classified into mode-I or mixed-mode type depending on whether a crack propagates in the direction of initial crack orientation or not. Figure 1.3 shows a schematic of different modes of fracture. Depending on the type of loading and the way in which crack flanks move with respect to each other, three different fracture modes can be identified. They are mode-I (opening mode), mode-II (sliding mode or in-plane shearing mode) and mode-III (tearing mode or

out-of-plane shearing mode). A combination of any of these modes is referred to as a mixed-mode problem. In the current work, the problems involve a combination of mode-I

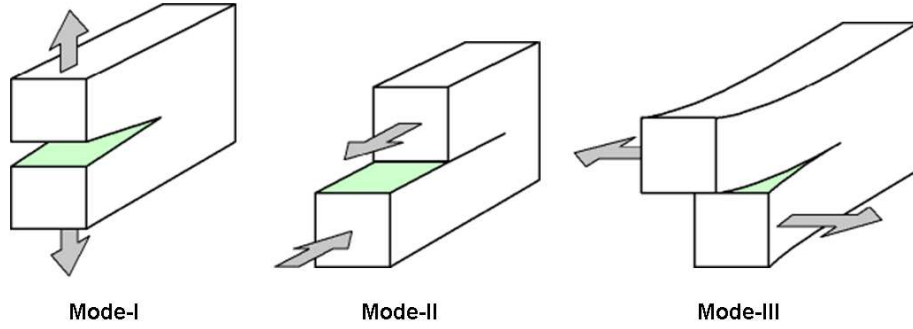


Figure 1.3: Schematic illustrating modes of fracture

and mode-II loading of a crack. Therefore the word ‘mixed-mode’ henceforth refers to a combination of mode-I and mode-II fractures.

As far as mode-I fracture is concerned, it is generally accepted that rapid crack initiation and propagation are governed by an equality between the dynamically evaluated crack driving force and the resistance of a material for crack extension [2, 4]. Consequently, the mode-I dynamic fracture criterion is expressed as

$$K_I^d(a(t), t, P) = K_D(v), \quad (1.1)$$

where $a(t)$ is the time dependent crack length and v is the crack speed. The dynamic stress intensity factor K_I^d measures the strength of the near tip fields which drive crack propagation. The right hand side of the equation, K_D is the so-called dynamic fracture toughness which is identified as a material property. This forms the basis for mode-I dynamic fracture

mechanics. Extensive research has been conducted over the past two decades in order to experimentally measure K_D and to determine whether it indeed is a material property.

Practical problems, however, often belong to a mixed-mode type because advanced materials often fail in a mixed-mode fashion. Physical mechanisms governing the dynamic mixed-mode fracture are not fully understood, especially regarding crack curving and branching. Based on observations from quasi-static mixed-mode fracture in materials, it is assumed that under mixed-mode loading, crack tends to grow according to the local mode-I conditions ($K_{II} = 0$ criterion or Maximum Tangential Stress (MTS) criterion). Some common examples of mixed-mode dynamic fractures are shown in Fig. 1.4.

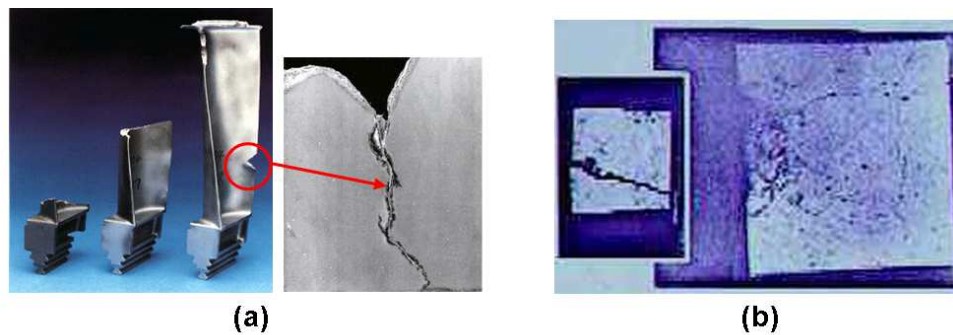


Figure 1.4: Mixed-mode dynamic fracture evidences, (a) environmentally assisted crack propagation from leading edge to the inside cooling surface of a gas turbine blade (Courtesy: Gas Turbine technology) and (b) Concrete damage after missile impact (Courtesy: Dept. of Civil and Structural Engineering, University of Sheffield, UK.)

1.1 Motivation and Literature Review

A great deal of experimental and numerical research has been reported on mode-I dynamic fracture of homogeneous and functionally graded materials. However, as mentioned earlier, practical problems often belong to a mixed-mode type. Further, a mixed-mode

dynamic crack propagation in FGM is more complex than in a homogeneous case because mode-mixity in the former arises not only from geometric and loading conditions, but also from mechanical property gradients. These introduce both normal and shear tractions ahead of the crack tip. Therefore mixed-mode dynamic fracture behavior of FGM needs to be studied. The full-field measurement of crack tip deformations for mixed-mode dynamic fracture studies is rather demanding due to a combination of spatial and temporal resolution challenges involved. Consequently, there is hardly any reported work in the literature about mixed-mode dynamic failure of FGM and structural foams.

In the current work, mixed-mode dynamic crack propagation is studied using two different experimental techniques. An optical interferometer called Coherent Gradient Sensing (CGS) is used to study mixed-mode dynamic failure of FGM. A digital image correlation method with high-speed digital imaging technology is developed to study mixed-mode failure of syntactic foams. Experiments are complemented by finite element simulations of mixed-mode dynamic failure in FGM. Here a cohesive element formulation is implemented to study the formation of new surfaces in nonhomogeneous materials.

In the following, the literature review for the current research is provided in three parts. In the first part, works on failure characterization of FGM is reviewed. In the second part, development of various full-field optical methods particularly the digital image correlation method to study fracture are reviewed. In the third part, numerical methods to simulate mixed-mode crack propagation under dynamic loading are reviewed.

1.1.1 Review of failure characterization of FGM

Delale and Erdogan [5] and Eischen [6] have shown that stress intensity factors in non-homogeneous materials such as FGM are affected by compositional gradients even though the inverse \sqrt{r} singularity near the crack tip is preserved as in homogeneous materials. Issues pertaining to fracture mechanics of FGM under static loading have been addressed in the recent literature. Jin and Batra [7], Gu and Asaro [8] provide quasi-static stress intensity factors for cracks in FGM for different geometry and loading conditions. Konda and Erdogan [9] have provided expressions for stress intensity factors (SIFs) of a mixed-mode fracture problem in a FGM. Abanto-Bueno and Lambros [10] have conducted experiments to study quasi-static mixed-mode crack initiation and growth in FGM. Shukla and coworkers [11, 12, 13] have reported crack tip stress fields for dynamically growing cracks in functionally graded materials for mode-I and mixed-mode loading conditions. They have derived asymptotic expansions for stresses and displacements in FGM with linear and exponential variations of elastic modulus. Tippur and his coworkers [14, 15, 16, 17] have addressed several issues related to mode-I dynamic fracture of FGM. Among the numerical studies related to FGM, Wang and Nakamura [18] have simulated crack propagation in elastic-plastic functionally graded materials using cohesive elements. Kim and Paulino [19] have addressed issues pertaining to crack path trajectories in FGM under mixed-mode and non-proportional loading conditions.

Ramaswamy *et al.*[20] have successfully used Coherent Gradient Sensing (CGS) to study mixed-mode crack tip deformations under static loading using a modified flexural specimen geometry. The problem of a crack located in a homogeneous material but close to an interface between two dissimilar linear elastic materials is examined by Lee and

Krishnaswamy [21]. Mason *et al.*[22] have used CGS to map mode-I and mode-II stress intensity factors in homogeneous polymer sheets under dynamic loading conditions. Prabhu and Lambros [23] have studied mode-I and mixed-mode crack tip fields in homogeneous materials by using the methods of CGS and caustics simultaneously.

Among the experimental investigations on mixed-mode fracture of FGM, works of Butcher *et al.*[24], Rousseau and Tippur [25] and Marur and Tippur [26] are noteworthy. In Ref. [24], feasibility of processing glass-filled epoxy beams for mixed-mode static fracture studies using optical interferometry is demonstrated. The role of material gradation on crack kinking under static loading conditions is presented in Ref. [25]. The possibility of using optimally positioned strain-gages near a crack tip undergoing mixed-mode loading to obtain SIF histories during impact loading is demonstrated in Ref. [26].

1.1.2 Review of optical methods to study fracture

Measuring surface deformations and stresses in real-time during a transient failure event such as dynamic crack initiation and growth in opaque materials is quite challenging due to a combination of spatial and temporal resolution demands involved. One of the very early efforts in this regard dates back to the work of de Graaf [27]. In this work, photoelastic measurement was attempted to witness stress waves around a dynamically growing crack in steel. This method continues to be popular in the study of fast fracture events [28, 29]. In recent years, a lateral shearing interferometer called Coherent Gradient Sensing (CGS) has become a tool of choice for studying dynamic fracture problems of opaque solids because of its robustness and insensitivity to rigid body motions and vibrations [16, 17, 30, 31]. Moiré interferometry has also been used in the past to measure in-plane displacement fields in

dynamic fracture experiments [32]. The electronic speckle pattern interferometry (ESPI) and digital speckle photography [33, 34, 35] methods have been found suitable for measuring both in-plane as well as out-of-plane deformations in opaque solids. The former uses speckle intensity patterns formed by the illumination of an optically rough surface with coherent light. An interferogram containing a fringe pattern is formed when speckle images, recorded before and after deformation, are subtracted digitally or when a photographic film is exposed twice is optically filtered. In the latter, the intensity of speckle images is compared digitally to determine local translations of speckles. This method does not require any reference wave and incoherent light is sufficient making it simple and easy to use. Using these methods, vibration measurements have been attempted by employing a high-speed camera in Refs. [36, 37]. Duffy's double aperture imaging scheme [39] has been modified by Sirohi *et al.*[38] to measure displacement-derivatives using ESPI. Chao, *et al.*[40] have studied deformations around a propagating crack using digital image correlation method with the aid of a Cranz-Schardin film camera. In this work, they have scanned film records obtained from the camera to perform correlation operations between successive images to estimate displacements.

It should be noted here that photoelasticity and interferometric techniques can all measure surface deformations in real time but they require somewhat elaborate surface preparation (transferring of gratings in case of moiré interferometry and preparing a specularly reflective surface in case of CGS, birefringent coatings in reflection photoelasticity, etc.). For cellular materials (syntactic foams, polymer metal foams, cellulosic materials, etc.) such surface preparations are rather challenging and in some cases may not be feasible at all. In those instances, digital image correlation method with white light illumination is a very useful tool due to the relative simplicity in this regard. It involves decorating a

surface with alternate mists of black and white paints. Recent advances in image processing methodologies and ubiquitous computational capabilities have made it possible to apply this technique to a variety of applications - in bio-mechanics to measure displacements of arterial tissues [41, 42], in metal forming to measure deformations during cold rolling [43], to measure displacements and strains in C/C composites [44], - just to name a few. Early contributors to the development of the method include Peters and Ranson, [45] and Sutton and his coworkers [46, 47]. Chen and Chiang [48] have subsequently developed a spectral domain approach to measure displacements of digitized speckle patterns. A stereo-vision methodology for measuring 3D displacement fields has also been introduced in recent times [49, 50].

With the advent of digital high-speed imaging technologies, imaging rates as high as several millions frames per second can be achieved at a relatively high spatial resolution. This has opened the possibility of extending digital image correlation (DIC) method to estimate surface displacements and strains for extracting dynamic fracture/damage parameters. In the current work, the DIC technique is extended to mode-I and mixed-mode dynamic fracture studies under stress wave loading conditions.

1.1.3 Review of numerical methods to simulate fracture

Numerical modeling of crack growth in a mixed-mode dynamic fracture event is very challenging. Material nonhomogeneity adds to the complexity in case of FGM. In order to predict the crack kinking direction in a FGM sample, the numerical scheme should have the following features built-in. The model should be able to represent continuous spatial

variation of material properties and the evolution of crack path must be a natural outcome of the analysis. There are mainly three types of approaches within the framework of finite element method to simulate the current problem of mixed-mode crack growth in nonhomogeneous medium. The first one is automatic moving finite element method with local re-meshing along the crack path. This approach requires that a user defined crack increment be provided and relies on one of the mixed-mode fracture criteria for determining crack growth direction. Ingraffea and co-workers [51] and Nishioka [52] have used this approach to simulate mixed-mode crack propagation in homogeneous materials. Nishioka *et al.*[53] were able to predict crack path of a mixed-mode dynamic fracture experiment using moving singular finite element method based on Delaunay automatic mesh generation. Kim and Paulino [19] have used local re-meshing technique to predict the crack path of the mixed-mode fracture tests conducted by Rousseau and Tippur [25] under static loading conditions. Recently, Tilbrook *et al.*[54] have simulated crack propagation in functionally graded materials under flexural loading. The limitations of this approach are that it requires robust automatic re-meshing algorithm, elaborate book-keeping system of node numbering to re-adjust the mesh pattern periodically and a mesh re-zoning procedure for mapping of the solution fields in the previous mesh onto those in the current mesh. The second approach is to use cohesive elements whose idea dates back to the work of Dugdale [55] and Barenblatt [56]. There are two basic types of cohesive zone models in the literature - intrinsic and extrinsic. The former is characterized by its increasing (hardening) and decreasing (softening) portions of a traction-separation law (TSL) whereas the latter has only the decreasing portion. The intrinsic cohesive formulation was first proposed by Needleman

[57]. Numerous other investigators have used this intrinsic type of formulation with different shapes of TSL. They are exponential [57, 18, 58], bilinear [59, 60, 61], and trapezoidal [62, 63] types. Xu and Needleman [58] have conducted mixed-mode dynamic crack growth simulation in brittle solids using such formulations. Wang and Nakamura [18] have used exponential TSL to simulate dynamic crack propagation in elastic-plastic graded materials. Zhang and Paulino [61] have conducted mode-I and mixed-mode dynamic fracture simulations in FGM samples. Madhusudhana and Narasimhan [63] have used trapezoidal TSL to simulate mixed-mode crack growth in ductile adhesive joints. The extrinsic type of formulation is also used by many researchers [64, 65, 66, 67]. Using extrinsic formulation, Ruiz *et al.*[67] have simulated mixed-mode dynamic fracture experiments of Guo and Kobayashi [32] and captured the experimentally observed crack path and displacement fields. Recently, Belytschko and co-workers [68, 69] have proposed a new method called extended finite element method (X-FEM) to model arbitrary discontinuities in finite element meshes. They added discontinuous enrichment functions to the finite element approximation to account for the presence of a crack while preserving the classical displacement variational setting. This flexibility enables the method to simulate crack growth without re-meshing. Using this method, Rabczuk *et al.*[70] have predicted crack path in a notched beam subjected to asymmetric four-point bending.

Physical mechanisms governing dynamic crack propagation under mixed-mode loading in FGM are not clearly understood. Observations based on mixed-mode quasi-static fracture indicate that under mixed-mode loading, cracks tends to grow according to a local mode-I condition ($K_{II} = 0$ criterion or MTS criterion). Extension of these methods to mixed-mode dynamic fracture of FGM requires evaluation of one of the fracture criterion and

local re-meshing. However, cohesive elements allow crack initiation and kinking to occur spontaneously without defining the crack path *a priori*. Therefore in the current work, intrinsic cohesive element method with bilinear traction-separation law is used to model the mixed-mode dynamic crack growth in FGM.

1.2 Objectives

The literature review suggests that there is a need for experimental and computational techniques to study mixed-mode dynamic fracture of novel heterogeneous material systems. Since most of the practical problems belong to the mixed-mode type, fracture of such materials is studied experimentally and numerically in this work. The following are the primary objectives of the present research:

- Investigate mixed-mode dynamic fracture behavior of FGM under impact loading conditions using optical interferometry and high-speed photography.
- Extract mixed-mode dynamic stress intensity factor histories using CGS interferograms.
- Study the effects of material gradation on crack path, crack speed and stress intensity factor histories.
- Develop an experimental method based on digital image correlation (DIC) and high-speed photography to measure transient surface deformations such as the one associated with a rapid growth of cracks in materials.

- Study mixed-mode dynamic fracture of syntactic foam specimen under impact loading conditions using the method of DIC with high-speed photography, map full-field in-plane displacements, strain and extract mixed-mode SIF histories.
- Perform finite element simulations of mixed-mode dynamic crack growth in FGM using cohesive element formulation.
- Compare the simulation results with experimental observations and explain the failure process.

1.3 Organization of Dissertation

This dissertation is organized into eight chapters including Introduction. In Chapter 2, the optical interferometric method of CGS is explained. The CGS experimental set-up, governing equations and experimental procedure are described. The asymptotic expressions for stresses in FGM considering linear variation elastic modulus are presented. The implementation of these equations into CGS governing equations to extract mixed-mode SIF from CGS interferograms is described.

In Chapter 3, mixed-mode dynamic fracture of glass-filled epoxy beam samples is experimentally studied using CGS. Preparation and characterization of FGM samples are described. The experimental results namely, crack length and crack speed histories and SIF histories are presented. Using the MTS fracture criterion, the initial crack kink angles are predicted and compared with the experimentally observed ones.

In Chapter 4, development of DIC method to measure surface deformations and strains is explained. A three-step digital image correlation technique is formulated for evaluating crack opening displacements and strains. The calibration and benchmark experiments and

their results for a rotating mirror type ultra high-speed digital camera system are presented. Using this method, surface deformations and strains of a specimen loaded in three-point bend configuration under static loading conditions are evaluated and compared with the corresponding finite element simulations.

In Chapter 5, mode-I dynamic fracture of a polymeric sample and mixed-mode dynamic fracture of syntactic foam samples are studied using digital image correlation and high-speed photography. The sample preparation and the experimental procedure are explained in detail. The crack opening and sliding displacements and crack tip dominant strain histories are computed from the speckle images. Dynamic stress intensity factors are extracted by performing over-deterministic least-squares analysis on crack opening and sliding displacements.

In Chapter 6, the details on finite element modeling of mixed-mode dynamic crack propagation in FGM is explained. The cohesive element formulation and its implementation in ABAQUSTM commercial finite element software package under the option of user defined element (UEL) is described. Using this option, exponential and bilinear type of traction separation laws are implemented.

Chapter 7 deals with the simulation of mixed-mode dynamic crack growth in functionally graded materials. Modeling aspects and application of graded material properties to the finite element model are explained. Simulations are carried out for two configurations, crack on the compliant side and crack on the stiffer side of a sample as explained in Chapter 2. The evolution of strain energy, kinetic energy as well as cohesive energies and the T -stress histories up to crack initiation are also computed.

Finally, the main conclusions of this dissertation are summarized in Chapter 8. Few potential topics for future research are highlighted.

CHAPTER 2

EXPERIMENTAL METHOD OF CGS TO STUDY DYNAMIC FRACTURE

In this chapter, the optical interferometric method of Coherent Gradient Sensing (CGS), used to study mixed-mode dynamic fracture of functionally graded materials, is discussed. The attractive features of this technique are relative ease of implementation in conjunction with high-speed camera and insensitivity to rigid body motions of the sample during a test. The crack tip fields for a dynamically loaded stationary crack as well as for a propagating crack are also explained in this chapter. The asymptotic expressions for crack tip stresses in FGM considering linear variation of elastic modulus are presented. The implementation of these equations into CGS governing equations to extract mixed-mode SIF from interferograms is described.

2.1 Optical set-up

CGS measures in-plane gradients of out-of-plane surface displacements (surface slopes) when used to study opaque solids. A schematic of the optical set-up [30, 71] is shown in Fig. 2.1. The measurement system consisted of an impactor, pulse-laser, CGS interferometer and a continuous access high-speed camera. The light beam was processed using a CGS interferometer comprising of a pair of Ronchi gratings (chrome-on-glass gratings) and a Fourier filtering/imaging lens. An argon-ion laser beam (wavelength $\lambda = 514 \text{ nm}$) was expanded and collimated into a 50 mm diameter beam and made to illuminate the opaque specimen with a specularly reflective surface. The reflected object wave front propagates through two Ronchi gratings separated by a distance Δ and undergoes diffraction in several

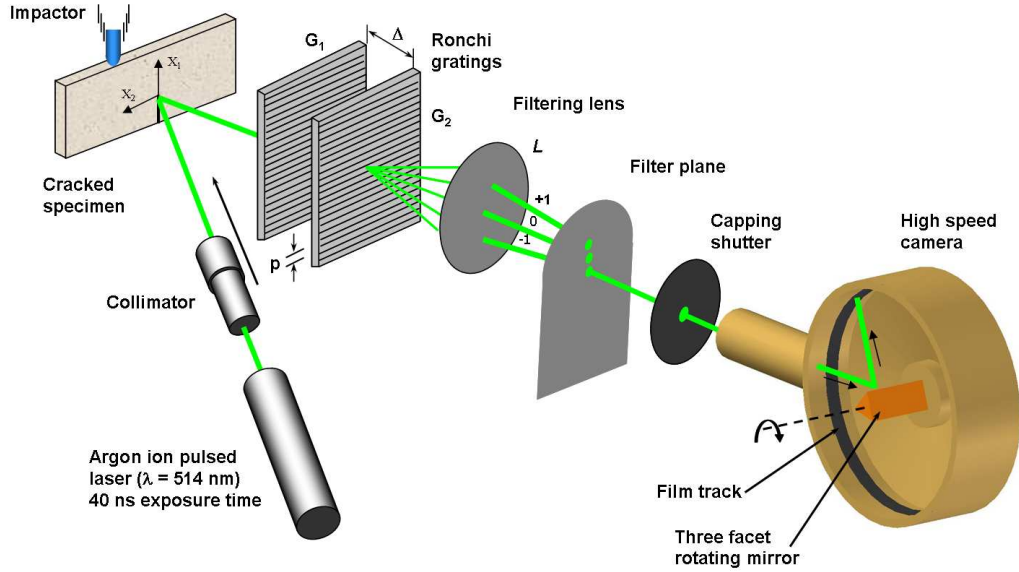


Figure 2.1: Schematic for reflection-mode CGS set-up with a high-speed camera

discrete directions as shown in Fig. 2.1. In this experiment, the principal direction of the gratings is along X_1 direction (in the direction of the crack). This causes the diffraction to occur in X_1 - X_3 plane resulting in surface slopes $\partial u_3/\partial X_1$, where $u_3(X_1, X_2)$ denotes the out-of-plane displacement component. The filtering lens L spatially filters the field distribution emerging from the G_2 plane and the associated spatial frequency content is displayed on its back focal plane (filter plane in the schematic). By locating an aperture around either the ± 1 -diffraction orders, the information corresponding to the displacement gradient is obtained on the image plane of the lens.

2.2 Working principle of CGS

The working principle of CGS interferometer is shown schematically in Fig. 2.2. Consider a plane wave reflected-off of the specimen surface. The incident wave is diffracted into

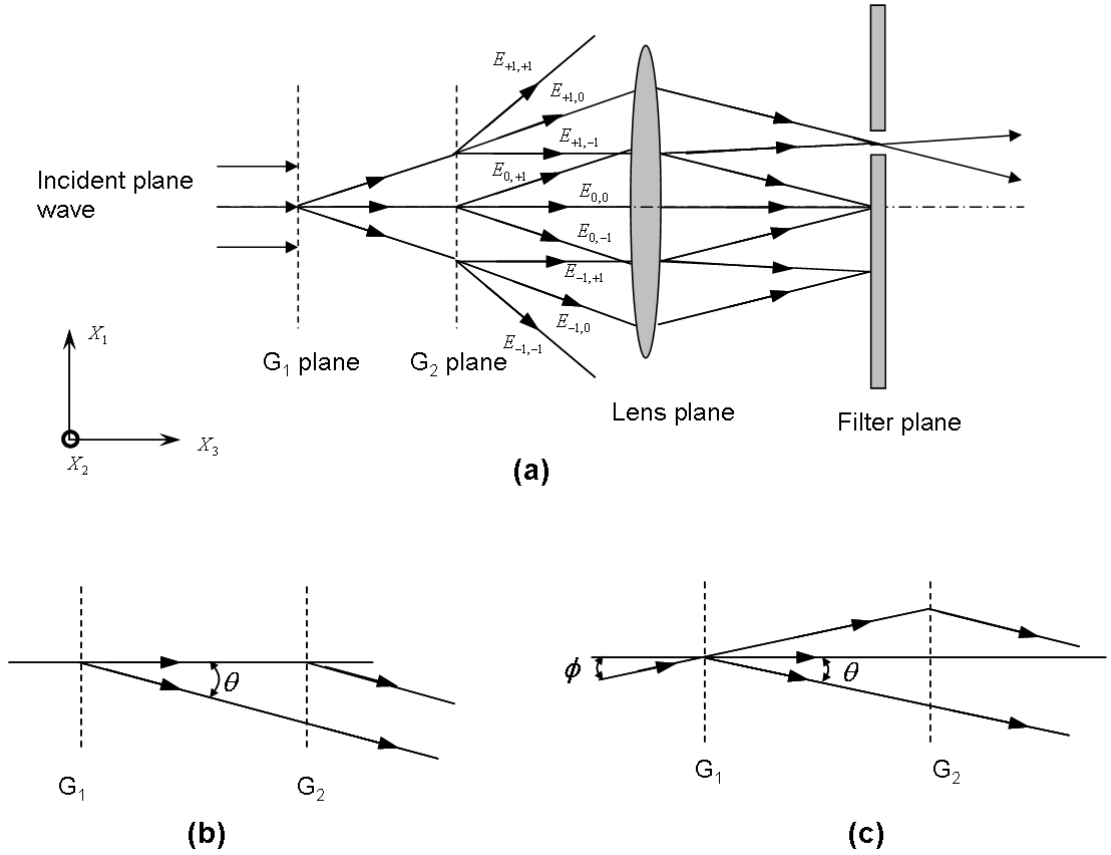


Figure 2.2: Working principle of CGS, (a) Diffraction of a collimated beam through two parallel Ronchi gratings, (b) undeformed object wave front and (c) deformed object wave front.

several diffraction orders $0, \pm 1, \pm 2 \dots$ by the first grating G_1 . The corresponding complex amplitude distribution of the diffracted waves are denoted by $E_0, E_1, E_{-1} \dots$. Consider only three diffracted wave fronts E_0 and $E_{\pm 1}$ for the simplicity analysis. That is the gratings are assumed to have a sinusoidal transmission function. The magnitude of the angle between the propagation direction of E_0 and $E_{\pm 1}$ is given by grating equation $\theta = \sin^{-1}(\lambda/p)$, where λ is the wave length of light used and p is the grating pitch. Upon incidence on the second grating G_2 , the wave fronts are further diffracted into $E_{0,0}, E_{0,+1}, E_{0,-1}, E_{+1,0}, E_{+1,-1}$

etc. The second subscript in each of these represents the diffraction order after leaving the grating G_2 . These wave fronts propagating in distinctly different directions are brought into focus at spatially separated spots on the back focal plane of the filtering lens L . The spacing between these diffraction spots is directly proportional to diffraction angle θ or inversely proportional to grating pitch p . Note from the Fig. 2.2 that the diffracted waves $E_{0,\pm 1}$ and $E_{\pm 1,0}$ are propagating in the same direction (parallel lines) but are displaced (or sheared) laterally in the X_1 -direction. These two overlapping but laterally displaced light beams produce ± 1 diffraction spots. Using a filtering aperture placed at the focal plane of the filtering lens, the diffraction order either $+1$ or -1 is allowed to pass through while blocking all others.

Consider the complex amplitudes of two plane wave fronts $E_0 = A_0 e^{ikl_1}$ and $E_{-1} = A_{-1} e^{ikl_2}$ for analysis. Here A_0 and A_{-1} are amplitudes, l_1 and l_2 are optical path lengths of E_0 and E_{-1} , respectively, and $k = 2\pi/\lambda$ is the wave number. The light intensity I for the undeformed object (see Fig. 2.2(b)) is proportional to,

$$I = (E_0 + E_{-1})(E_0 + E_{-1})^* = A + B \cos \{k(l_1 - l_2)\}. \quad (2.1)$$

The light intensity reaches its maximum value when the following condition for constructive interference is satisfied:

$$k(l_1 - l_2) = 2N\pi \quad (N = \pm 1, \pm 2, \dots). \quad (2.2)$$

It can be seen from Fig. 2.2(b) that

$$(l_1 - l_2) = \Delta[1 - (\cos \theta)^{-1}], \quad (2.3)$$

where θ is the diffraction angle of the grating. For small angles, ($\sin \theta \sim \theta = \lambda/p$). Now expanding the right hand side of Eq. 2.3 using the binomial expansion, we get

$$(l_1 - l_2) = \Delta[1 - (\cos \theta)^{-1}] = \Delta \left[1 - \left(1 - \frac{\theta^2}{2} + \frac{\theta^4}{8} - \dots \right) \right] \approx \Delta \left(\frac{\theta^2}{2} \right). \quad (2.4)$$

Combining Eqs. 2.2 and 2.4, and noting that $k = 2\pi/\lambda$, we get

$$\Delta \frac{\theta^2}{2} = N\lambda. \quad (2.5)$$

Equation 2.5 suggests that N is a constant since θ , p and Δ are all constants for an undeformed object. Therefore, initially the interferometer produces a uniform fringe in the entire field of observation.

When the specimen deforms, the collimation of the object wave is perturbed or light rays are deflected relative to the optical axis. For simplicity, consider light ray deflections only in the $X_1 - X_3$ plane and ϕ be the angular deflection of a generic ray. Let l'_1 and l'_2 be the optical paths of E_o and E_{+1} after deformation (see Fig. 2.2(c)). Now the intensity of light is given by,

$$I' = A' + B' \cos [k(l'_1 - l'_2)], \quad (2.6)$$

where,

$$\begin{aligned}
(l'_1 - l'_2) &= \Delta [(\cos \phi)^{-1} - (\cos(\theta - \phi))^{-1}] \\
&= \Delta \left[\left\{ 1 - \frac{\phi^2}{2} + \dots \right\} - \left\{ 1 - \frac{(\theta - \phi)^2}{2} + \dots \right\} \right] \\
&\approx \Delta \left[-\theta\phi + \frac{\theta^2}{2} \right].
\end{aligned} \tag{2.7}$$

Again, the intensity of light I attains a maximum value when condition for constructive interference namely,

$$k(l'_1 - l'_2) = 2M\pi \quad (M = \pm 1, \pm 2, \dots), \tag{2.8}$$

is met. By combining Eqs. 2.2, 2.7 and 2.8, we can get

$$-\theta\phi\Delta = (M - N)\lambda \tag{2.9}$$

or,

$$\phi = (N - M) \frac{\lambda}{\Delta\theta} = m \frac{\lambda}{\Delta\lambda/p} = m \frac{p}{\Delta}, \quad m = 0, \pm 1, \pm 2, \dots \tag{2.10}$$

where $m = (N - M)$. For reflection mode CGS, $\phi = \partial(\delta s)/\partial X_1$, where $\delta s = 2w$ is the optical path change due to the applied stress with w being the out-of-plane displacement component. For plane stress conditions, we have

$$w \approx \frac{-\nu B}{2E}(\sigma_x + \sigma_y). \tag{2.11}$$

Therefore, the governing equation for reflection-mode CGS with plane stress assumption becomes

$$\frac{\partial w}{\partial X_1} \approx \frac{\partial}{\partial X_1} \left[\frac{-\nu B}{2E} (\sigma_x + \sigma_y) \right] = m \frac{p}{2\Delta}. \quad (2.12)$$

2.3 Experimental procedure

The specimen was initially rested on two soft blocks of putty to preclude any interaction from the supports (anvils) while the specimen undergoes stress wave loading. The top edge of the specimen was taped with a thin adhesively backed copper strip. During the experiment, a pneumatically operated cylindrical steel hammer with a hemispherical tip was launched towards the specimen (velocity 5 *m/sec*). During its descent, a velocity flag (of width ~ 6.4 *mm*), attached to the impactor, first triggered a photo-detector to open a capping shutter located in front of the high-speed camera allowing light to reach its internal cavity. When the impactor-head contacted the adhesive backed copper tape affixed to the top edge of the specimen, it closed an electrical circuit initiating a series of laser pulses for a duration corresponding to a single sweep of the laser beam on a stationary photographic film (Kodak TMAX-400) track. The light entering the camera was reflected-off of a spinning three-facet mirror mounted on a turbine shaft driven using compressed air. The reflected light beam was swept on the film held in the film track as discrete images. At the end of that period, the capping shutter was closed to prevent over-writing on the film. In the current experiments, the laser pulse was repeated every 5 μ s (200,000 frames per second) with a pulse width (exposure time) of 40 ns and a total recording duration of approximately 320 μ s. With these settings, roughly 70 images were recorded on the photographic film.

The light beam reflected off the specimen surface carries information about local surface deformations. The resulting fringes represent surface slopes in the initial crack direction.

2.4 Extraction of stress intensity factors from interferograms

In Eq. 2.12, σ_x and σ_y are the Cartesian stress components. By using chain rule of differentiation, one can transform quantities from $X_1 - X_2$ coordinates to $r - \theta$ coordinate system. The quantity $\sigma_x + \sigma_y$ is an invariant under coordinate transformation. Hence,

$$\frac{\partial w}{\partial X_1} = \frac{\partial w}{\partial r} \frac{\partial r}{\partial X_1} + \frac{\partial w}{\partial \theta} \frac{\partial \theta}{\partial X_1}, \quad (2.13)$$

where $r^2 = X_1^2 + X_2^2$, $\theta = \tan^{-1}(X_2/X_1)$, $X_1 = r \cos \theta$, $X_2 = r \sin \theta$. Further, $\partial r / \partial X_1 = X_1 / r = \cos \theta$, $\partial \theta / \partial X_1 = -X_2 / r^2 = -\sin \theta / r$. By expressing $(\sigma_x + \sigma_y)$ in Eq. 2.12 using asymptotic expansion for crack tip stresses, in-plane gradients of the out-of-plane displacement become [30, 72]

$$\frac{\partial w(t)}{\partial X_1} = \frac{-\nu B}{2E} \left[\sum_{N=1}^{\infty} C_N(t) \left(\frac{N}{2} - 1 \right) r^{(\frac{N}{2}-2)} \cos \left[\left(\frac{N}{2} - 2 \right) \theta \right] \right] = \frac{Mp}{2\Delta}, \quad (2.14)$$

$$\frac{\partial w(t)}{\partial X_2} = \frac{-\nu B}{2E} \left[\sum_{N=1}^{\infty} C_N(t) \left(\frac{N}{2} - 1 \right) r^{(\frac{N}{2}-2)} \sin \left[\left(\frac{N}{2} - 2 \right) \theta \right] \right] = \frac{Mp}{2\Delta}, \quad (2.15)$$

for the crack opening mode (mode-I) and

$$\frac{\partial w(t)}{\partial X_1} = \frac{-\nu B}{2E} \left[\sum_{N=1}^{\infty} D_N(t) \left(\frac{N}{2} - 1 \right) r^{(\frac{N}{2}-2)} \sin \left[\left(\frac{N}{2} - 2 \right) \theta \right] \right] = \frac{Mp}{2\Delta}, \quad (2.16)$$

$$\frac{\partial w(t)}{\partial X_2} = \frac{-\nu B}{2E} \left[\sum_{N=1}^{\infty} D_N(t) \left(\frac{N}{2} - 1 \right) r^{(\frac{N}{2}-2)} \cos \left[\left(\frac{N}{2} - 2 \right) \theta \right] \right] = \frac{Mp}{2\Delta}, \quad (2.17)$$

for the in-plane shear mode (mode-II). In the above (r, θ) are the polar coordinates centered at the crack tip. In Eqs. (2.14)-(2.17), C_N and D_N are coefficients for mode-I and mode-II, respectively. The above equations can be used for a dynamically loaded stationary crack by making an implicit assumption that inertial effects enter the coefficients while retaining the functional form of the quasi-static counterpart. Accordingly, the coefficients C_N and D_N are represented as functions of time t .

2.4.1 Pre-crack initiation period

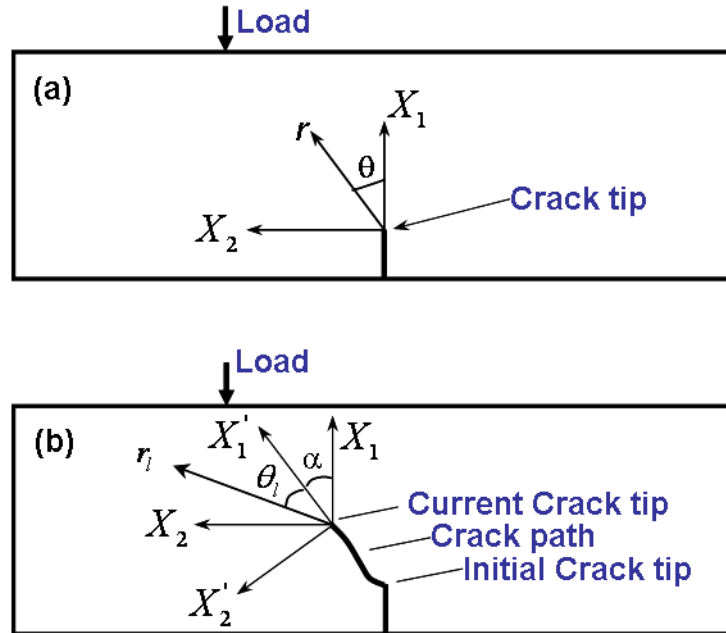


Figure 2.3: Global and local crack tip coordinate systems for (a) stationary crack and (b) propagating crack

Figures. 2.3(a) and (b) show the crack tip coordinate systems followed in this work for digitizing CGS fringes and to extract mode-I and mode-II stress intensity factors. Consider the situation prior to crack initiation as shown in Fig. 2.3(a). Here $X_1 - X_2$ is the global

coordinate system which is aligned with the local (crack tip) coordinate system. Since the crack is aligned with the principal direction of the gratings, CGS governing equation for mixed-mode stress intensity factors is obtained by superposing mode-I and mode-II fields from Eqs. 2.14 and 2.16:

$$\frac{\partial w(t)}{\partial X_1} = \frac{\nu B}{2E} \left[\left\{ \sum_{N=1}^{\infty} C_N(t) \left(\frac{N}{2} - 1 \right) r^{\left(\frac{N}{2} - 1 \right)} \cos \left[\left(\frac{N}{2} - 2 \right) \theta \right] \right\} + \left\{ \sum_{N=1}^{\infty} D_N(t) \left(\frac{N}{2} - 1 \right) r^{\left(\frac{N}{2} - 1 \right)} \sin \left[\left(\frac{N}{2} - 2 \right) \theta \right] \right\} \right] = \frac{Mp}{2\Delta}. \quad (2.18)$$

The coefficients of the terms (with $N = 1$) in the asymptotic series are related to mode-I and mode-II stress intensity factors $K_{ID}(t)$ and $K_{IID}(t)$, respectively, as

$$C_1(t) = K_{ID}(t) \sqrt{\frac{2}{\pi}}, \quad D_1(t) = K_{IID}(t) \sqrt{\frac{2}{\pi}}. \quad (2.19)$$

2.4.2 Post-crack initiation period

Since the crack path during growth can be along an arbitrary direction, it is convenient to define a local (variable) coordinate system (X'_1, X'_2) which is instantaneously aligned with the current crack path as shown in Fig. 2.3(b). While digitizing fringes in the post-crack initiation period, coordinates of the digitized points are transformed from the global system (X_1, X_2) to the local rotated system (X'_1, X'_2) . The CGS fringes represent surface slopes as indicated by Eq. 2.12. Since the crack is at an arbitrary angle, surface slope has to be resolved along the local coordinates as,

$$\frac{\partial w}{\partial X_1} = \frac{\partial w}{\partial X'_1} \cos \alpha + \frac{\partial w}{\partial X'_2} \sin \alpha, \quad (2.20)$$

where α is the crack kink angle as shown in Fig. 2.3(b). By using modified versions of Eqs. 2.14-2.17 and 2.20, for a steadily propagating crack, deformations can be related to optical measurements as, [74, 12]

$$\begin{aligned} & \frac{-\nu B}{2E} \left[-\frac{1}{2} r_l^{-3/2} \left\{ f(V; C_L, C_S) C_1(t) \cos\left(\frac{3\theta_l}{2} + \alpha\right) + \right. \right. \\ & \qquad \qquad \qquad \left. \left. g(V; C_L, C_S) D_1(t) \sin\left(\frac{3\theta_l}{2} + \alpha\right) \right\} + \right. \\ & \sum_{N=2}^{\infty} C_N(t) \left(\frac{N}{2} - 1\right) r_l^{\left(\frac{N}{2} - 2\right)} \cos\left\{\alpha + \left(2 - \frac{N}{2}\right)\theta_l\right\} + \\ & \left. \sum_{N=2}^{\infty} D_N(t) \left(\frac{N}{2} - 1\right) r_l^{\left(\frac{N}{2} - 2\right)} \sin\left\{\alpha + \left(2 - \frac{N}{2}\right)\theta_l\right\} \right] = \frac{Mp}{2\Delta}. \end{aligned} \quad (2.21)$$

Here f and g are functions associated with the instantaneous crack velocity and (r_l, θ_l) denote the crack tip polar coordinates associated with a growing crack,

$$r_l = \left\{ (X'_1)^2 + \alpha_L^2 (X'_2)^2 \right\}^{1/2}, \quad \theta_l = \tan^{-1} \frac{\alpha_L X'_2}{X'_1}. \quad (2.22)$$

For plane stress, the functions f and g are given by [12],

$$f(V; C_L, C_S) = \left(\frac{1+\nu}{1-\nu} \right) \frac{(1+\alpha_S^2)(1-\alpha_L^2)}{4\alpha_L\alpha_S - (1+\alpha_S^2)^2}, \quad (2.23)$$

$$g(V; C_L, C_S) = \left(\frac{1+\nu}{1-\nu} \right) \frac{2\alpha_S(1-\alpha_L^2)}{4\alpha_L\alpha_S - (1+\alpha_S^2)^2}, \quad (2.24)$$

where,

$$\alpha_L = \left[1 - \frac{\rho(1-\nu)}{2\mu} V^2 \right]^{1/2}, \quad \alpha_S = \left[1 - \frac{\rho}{\mu} V^2 \right]^{1/2}. \quad (2.25)$$

Here V is the crack speed, μ and ρ are the *local* shear modulus and mass density, respectively.

Analyzing fringes in FGM using Eqs. 2.18 and 2.21 implicitly assumes a locally homogeneous material behavior in the crack tip vicinity. This needs justification since crack tip stress fields for steadily and transiently growing cracks for nonhomogeneous material have been made available by Shukla and coworkers [11, 12] in recent years. For a relatively shallow elastic gradients such as the ones used in the current study, it is shown in an earlier work [15] that results would not be greatly affected (differences being less than 5 %) by such an assumption. Further, there are also difficulties associated with utilizing existing FGM crack tip fields [11] to analyze optical interferograms in the current work. Specifically, theoretical derivations [11, 12] use spatial variation of elastic modulus and mass density to have a single nonhomogeneity parameter for an exponential type description or assume a constant mass density while varying the modulus. However, particulate composites in general and glass-filled epoxy FGM prepared for this work in particular have significantly different elastic modulus and mass density variations (2.5 fold (4.0 GPa to 10 GPa) over a width of 43mm where as mass density variation was 1.5 fold (1175 kg/m³ to 1700 kg/m³) over the same length) which limit the usage of those reported equations.

The role of crack tip transients namely the rate of change of stress intensity factors and crack accelerations/decelerations are described in Ref. [12]. Based on the experimental results (to be described later), these effects were found to be negligible for the current work. For example, it is noted in Ref. [12] that the rate of change of SIF on out-of-plane displacements becomes relatively insignificant if $dK_{ID}(t)/dt$ is within 1.0×10^5 MPa m^{1/2}/sec and in the current work $dK_{ID}(t)/dt$ values were an order of magnitude less than this value. Also out-of-plane displacements are said to be minimally affected if accelerations are less than 1.0×10^7 m/sec². Again, maximum acceleration recorded during this work was an

order of magnitude lower. Thus extracting SIF from fringes using steady-state assumptions is quite reasonable.

While digitizing interferograms, the current crack tip location was identified and the crack kink angle was evaluated. Simultaneously, around the crack tip, the fringe location r, θ and the fringe order M were also recorded. The collected data was used to perform an over-deterministic least-squares analysis [73, 30] on Eq. 2.18 or 2.21 depending on whether the interferogram belonged to pre-initiation or post-initiation period to extract K_I and K_{II} . To maintain the accuracy of the digitized data points as well as to exclude the region where 3D-effects [30] dominate, data points in the range ($0.3 < r/B < 1.3$) behind the crack tip were chosen for analysis.

2.5 Computation of crack speed

The crack speed history was also determined by differentiating crack length history with respect to time. That is, for every 5 μs after crack initiation, horizontal and vertical components of crack increment were identified and the resultant crack increment was calculated. These were sequentially added to get the instantaneous absolute crack length. The crack speed history was estimated as

$$v_i = \left(\frac{da}{dt} \right) = \frac{a_{i+1} - a_{i-1}}{t_{i+1} - t_{i-1}}, \quad (2.26)$$

where $a_i = a_{i-1} + \Delta a$ and $\Delta a = \sqrt{(\Delta a_h)^2 + (\Delta a_v)^2}$. Here Δa_h and Δa_v are horizontal and vertical components of the crack increment, respectively.

2.6 Crack tip fields in FGM with linear material property variation

2.6.1 Crack along the direction of property gradation

In this section, an asymptotic expression for $\sigma_x + \sigma_y$ (up to six terms) for a stationary crack tip in a functionally graded material having linear variation of elastic modulus is presented. By making use of these expressions, the methodology to extract mixed-mode stress intensity factors from CGS fringes is explained. The elastic crack tip fields are available for non-homogeneous materials having exponential variation of material properties. The use of exponential variation simplifies the process of deriving the crack tip fields. However, a material having an exponential variation of elastic modulus is difficult to prepare. Recently, attempts were made to derive crack tip stress fields for a FGM with a linear property variation [13, 75].

Consider an edge cracked beam having a linear material property variation as described by the following equation:

$$E(X_1) = E_o(1 + \delta_f X_1), \quad -0.0085 \text{ m} \leq X_1 \leq 0.0345 \text{ m}. \quad (2.27)$$

The variable E_o is the elastic modulus (in GPa) at the crack tip as shown in Fig. 2.4(a) and δ_f is the non-homogeneity parameter. The assumed variations of elastic modulus for FGM samples prepared (to be discussed in Chapter 3) are shown in Fig. 2.4(b).

In the following, the expressions provided for $\sigma_x + \sigma_y$ are deduced from Eqs. (11) and (12) of Ref. [13].

$$\sigma_x + \sigma_y = 2 \left[A_0 r^{-1/2} \cos \frac{\theta}{2} + B_0 + A_1 r^{1/2} \cos \frac{\theta}{2} + B_1 r \cos \theta + A_2 r^{3/2} \cos \frac{3\theta}{2} + B_2 r^2 \cos 2\theta \right] +$$

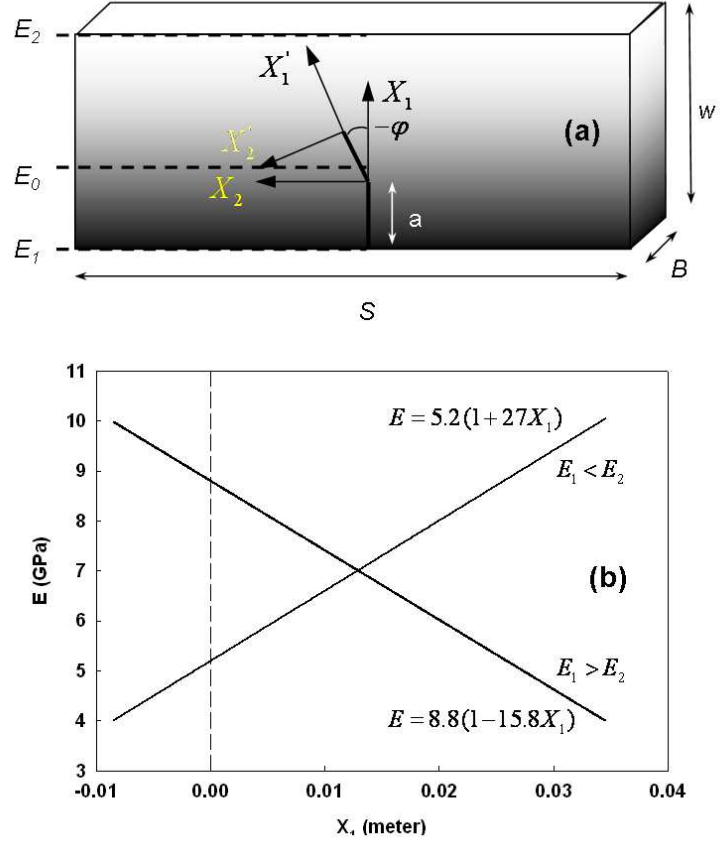


Figure 2.4: (a) Schematic of FGM sample with linear material property variation, (b) elastic modulus variation in graded samples (broken line denotes the crack tip location)

$$\begin{aligned}
& \delta_f \left[A_0 r^{1/2} \left\{ -2 \sin \theta \sin \frac{\theta}{2} - 2 \cos \frac{\theta}{2} \right\} - B_0 r \cos \theta + A_1 r^{3/2} \left\{ 2 \sin \theta \sin \frac{\theta}{2} - \frac{2}{3} \cos \frac{3\theta}{2} \right\} + \right. \\
& \qquad \qquad \qquad \left. B_1 r^2 \left\{ -2 \cos^2 \theta + 2 - \frac{1}{2} \cos 2\theta \right\} \right] + \\
& \delta_f^2 \left[A_0 r^{3/2} \left\{ (\nu - 7 + 2 \cos \theta) \sin \theta \sin \frac{\theta}{2} + (-2 \sin^2 \theta + \frac{\nu}{2} \sin^2 \theta + 2 \cos \theta) \cos \frac{\theta}{2} + \frac{2}{3} \cos \frac{3\theta}{2} \right\} + \right. \\
& \qquad \qquad \qquad \left. B_0 r^2 \left\{ \left(-\frac{1}{2} - \frac{\nu}{4} \right) \cos 2\theta + (3 - 2\nu) \cos^2 \theta - 2 + 2\nu \right\} \right] \quad (2.28)
\end{aligned}$$

for mode-I and

$$\begin{aligned}
\sigma_x + \sigma_y = & 2 \left[-C_0 r^{-1/2} \sin \frac{\theta}{2} + C_1 r^{1/2} \sin \frac{\theta}{2} + D_1 r \sin \theta + C_2 r^{3/2} \sin \frac{3\theta}{2} + D_2 r^2 \sin 2\theta \right] + \\
& \delta_f \left[C_0 r^{1/2} \left\{ -2 \sin \theta \cos \frac{\theta}{2} - 2 \sin \frac{\theta}{2} \right\} + D_0 r \sin \theta + C_1 r^{3/2} \left\{ -2 \sin \theta \cos \frac{\theta}{2} - \frac{2}{3} \sin \frac{3\theta}{2} \right\} + \right. \\
& \left. D_1 r^2 \left\{ 2 \sin \theta \cos \theta - \frac{1}{2} \sin 2\theta \right\} \right] + \\
\delta_f^2 \left[& C_0 r^{3/2} \left\{ ((5 - \nu) \sin \theta + \sin 2\theta) \cos \frac{\theta}{2} + \left(-\frac{\nu}{2} \sin^2 \theta - \frac{3}{2} \cos^2 \theta + 2 \sin \theta + 2 \cos \theta + \frac{3}{2} \right) \sin \frac{\theta}{2} - \right. \right. \\
& \left. \left. \frac{2}{3} \cos \frac{3\theta}{2} \right\} + D_0 r^2 \left\{ \left(-\frac{1}{2} - \frac{\nu}{4} \right) \cos 2\theta + \left(\frac{11}{2} - \frac{\nu}{2} \right) \sin \theta \cos \theta + (\nu + 2) \sin^2 \theta \right\} \right] \quad (2.29)
\end{aligned}$$

for mode-II loading conditions. The expression for $\sigma_x + \sigma_y$ for mixed-mode problem is readily obtained by superposing Eqs. 2.28 and 2.29. The mixed-mode stress intensity factors, K_I and K_{II} , are related to the constant coefficients of singular terms of the asymptotic series in Eqs. 2.28 and 2.29 by $K_I = A_0 \sqrt{2\pi}$ and $K_{II} = C_0 \sqrt{2\pi}$.

2.6.2 Crack inclined to the direction of property gradation

Once the crack initiates, it can propagate at an angle to the direction of material property gradation. Therefore the equations presented in the previous section are no longer valid for post-crack initiation period and a new set of equations need to be used. Consider a case where the crack has initiated and propagated at an angle ϕ with respect to the material gradation as shown in Fig. 2.4(a). Now the elastic modulus variation given by Eq. 2.27 can be re-written as

$$E(x, y) = E_o(1 + \alpha_f X_1' + \beta_f X_2'), \quad (2.30)$$

where

$$\alpha_f = \delta_f \cos \phi, \quad \beta_f = \delta_f \sin \phi. \quad (2.31)$$

In the above equation, E_o is the elastic modulus at the current crack tip ($X'_1 = X'_2 = 0$) and δ_f is the non-homogeneity parameter having dimension (Length)⁻¹. In the following, a four-term expansion for $\sigma_x + \sigma_y$ is deduced from Eqs. (31) and (32) of Ref. [13].

$$\begin{aligned} \sigma_x + \sigma_y = 2 & \left[A_0 r^{-1/2} \cos \frac{\theta}{2} - C_0 r^{-1/2} \sin \frac{\theta}{2} + B_0 + A_1 r^{1/2} \cos \frac{\theta}{2} + C_1 r^{1/2} \sin \frac{\theta}{2} \right. \\ & \left. + B_1 r \cos \theta + D_1 r \sin \theta \right] \\ & + \alpha_f \left[A_0 r^{1/2} \left\{ -2 \sin \theta \sin \frac{\theta}{2} - 2 \cos \frac{\theta}{2} \right\} + C_0 r^{1/2} \left\{ -2 \sin \theta \cos \frac{\theta}{2} - 2 \sin \frac{\theta}{2} \right\} \right. \\ & \left. - B_0 r \cos \theta - 2 D_0 r \sin \theta \right] \\ & + \beta_f \left[A_0 r^{1/2} \left\{ 2 \sin \theta \cos \frac{\theta}{2} + 2 \sin \frac{\theta}{2} \right\} + C_0 r^{1/2} \left\{ -2 \sin \theta \cos \frac{\theta}{2} - 2 \cos \frac{\theta}{2} \right\} \right. \\ & \left. + 3 B_0 r \sin \theta - D_0 r \cos \theta \right] \quad (2.32) \end{aligned}$$

2.7 Extraction of SIFs with difference formulation

As already mentioned, the CGS fringes represent surface slopes in the principal direction of the grating. Therefore the expression for out-of-plane displacement w (Eq. 2.11) was differentiated in Section 2.4 before arriving at the final equations (Eq. 2.18 or 2.21). One could also adopt a difference formulation instead of a derivative formulation as shown below,

$$\frac{\partial w}{\partial X_1} \approx \frac{\delta w}{\delta X_1} = \frac{w_{i+1} - w_i}{\delta X_1} = \frac{Np}{2\Delta}, \quad (2.33)$$

where δ represents the difference operator. By substituting for w from Eq. 2.11, we get

$$\frac{-\nu B}{2\delta X_1} \left[\left(\frac{\sigma_x + \sigma_y}{E_o(1 + \alpha_f X'_1 + \beta_f X'_2)} \right)_{i+1} - \left(\frac{\sigma_x + \sigma_y}{E_o(1 + \alpha_f X'_1 + \beta_f X'_2)} \right)_i \right] = \frac{Np}{2\Delta}, \quad (2.34)$$

where δX_1 is the shearing distance (which is 1.05 mm for the current experimental set-up having $p = 25$ mm and $\Delta = 48$ mm). In the above equation, the expression for $\sigma_x + \sigma_y$ will be taken from Eq. 2.32 with r and θ being evaluated at subscripts $i + 1$ and i as

$$\begin{aligned} r_i &= \sqrt{X_1^2 + X_2^2}, & \theta_i &= \tan^{-1} \frac{X_2}{X_1} \\ r_{i+1} &= \sqrt{(X_1 - \delta X_1)^2 + X_2^2}, & \theta_{i+1} &= \tan^{-1} \frac{X_2}{X_1 - \delta X_1}. \end{aligned} \quad (2.35)$$

The over-deterministic least squares analysis [73, 30] was carried out and mixed-mode stress intensity factors were extracted upto crack initiation.

CHAPTER 3

MIXED-MODE DYNAMIC FRACTURE OF FGM USING CGS

In this chapter, investigation on mixed-mode dynamic fracture of glass filled epoxy beam samples (in two different configurations) using CGS is described. Preparation and characterization of FGM samples is also elaborated. The experimental results namely, the crack length and the crack speed histories and the stress intensity factor histories are presented. Using the maximum tangential stress (MTS) fracture criterion, the initial crack kink angles are predicted and compared with the observed kink angles.

3.1 Material Preparation

FGM samples were prepared by continuously varying the volume fraction of filler particles in the matrix. Solid soda-lime spherical glass particles (Spheriglass 3000, 35 μm diameter, uncoated, from Potters Industries, Inc., USA) were used as the filler material. A low-viscosity, room temperature curing epoxy prepared by mixing bisphenol-A resin and amine based hardener in the ratio 100:36 was used as the matrix material. Bulk elastic properties of the filler material and the matrix are listed in Table 3.1. The material

	E (GPa)	ν	ρ kg/m ³
Epoxy	3.2	0.34	1175
Soda-lime glass ¹	70.0	0.23	2500

Table 3.1: Nominal bulk properties of the constituent materials

preparation consisted of mixing glass particles (40 % volume fraction) into the epoxy resin. Sufficient care was exercised in order to avoid entrapment of air bubbles. The time period

between mixing of particles and pouring into the mold was optimized to get a compositional gradient over the desired height of the sample. The gravity assisted casting method used here produced a monotonic variation of volume fraction of glass particles in the vertical direction. The details are avoided here for brevity and can be found in Butcher *et al.*[24]. Once the specimens were cured, they were removed from the mold and rested for a week before machining to the dimensions shown in Fig. 3.1. A grayscale is used to schematically

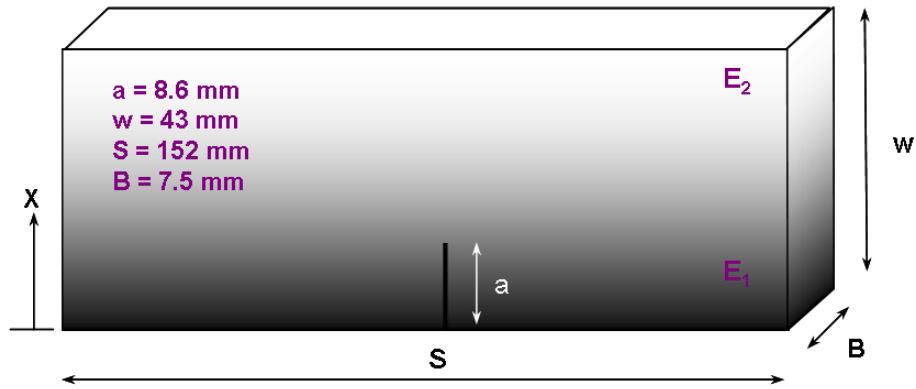


Figure 3.1: Schematic of FGM sample used in experiments

represent the compositional gradation (i.e., the mass density is maximum at the bottom of the sample and decreases in the X -direction).

3.2 Material characterization

Ultrasonic pulse-echo technique was used to measure material properties. A longitudinal wave transducer (Panametrics # V129RM 10MHz, dia=5 mm) and a shear wave transducer (Panametrics # V156RM; 5MHz, dia=7 mm) were used to measure wave speeds C_L and C_S , respectively, at discrete locations in the sample. The variations of C_L and C_S along the width of the sample are shown in Fig. 3.2. A look-up chart of mass density ρ

as a function of longitudinal wave speed C_L is available for glass-filled epoxy in Ref. [24]. By using measured values of C_L and C_S and the value of ρ from the look-up charts, elastic moduli and Poisson's ratios were estimated along the width of the sample using,

$$C_L = \sqrt{\frac{E(1-\nu)}{\rho(1+\nu)(1-2\nu)}}, \quad C_S = \sqrt{\frac{E}{2\rho(1+\nu)}}. \quad (3.1)$$

Elastic modulus and mass density variations along the width of the sample are shown in

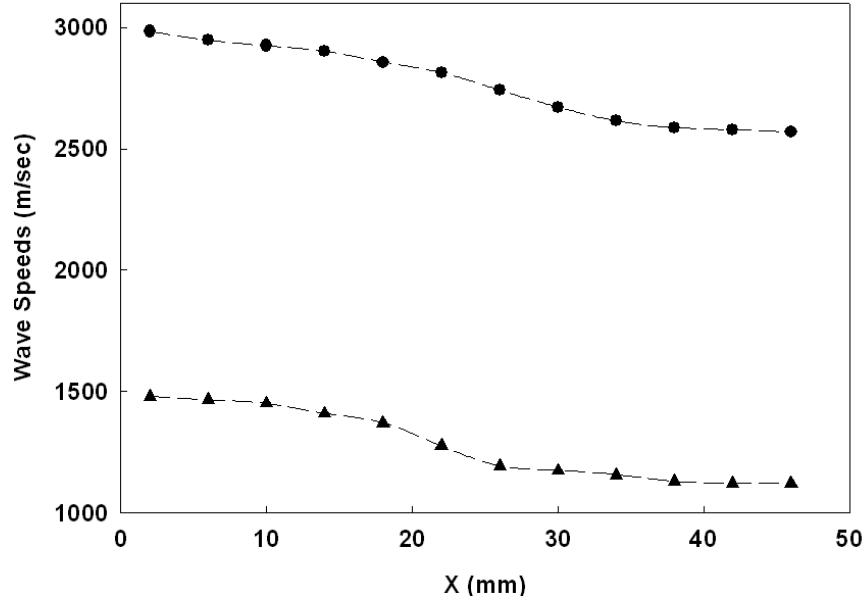


Figure 3.2: Variation of longitudinal and shear wave speeds along the width of the sample

Fig. 3.3. It can be seen from this figure that the elastic modulus varies in a sigmoidal fashion from ~ 10 GPa to ~ 4 GPa over a width of 43 mm. The mass density varies from ~ 1750 kg/m³ to ~ 1200 kg/m³ over the same width. The corresponding Poisson's ratio variation was between 0.33 and 0.37. This variation in ν was not expected to play a significant role

in the fracture behavior of FGM [6]. Therefore a constant value of $\nu=0.34$ was chosen throughout this work.

Mode-I crack initiation toughness tests were also conducted on homogeneous samples of various volume fractions (0%, 7%, 14%, 21%, 28% and 35%) of the filler. Beam samples of dimensions 152 mm \times 43 mm and 7.5 mm thick were machined for fracture tests. An edge crack of length 10 mm ($a/W = 0.23$) was cut along the mid-span in each of these samples. The so-called Dally-Sanford single strain gage method [76] was used to obtain dynamic stress intensity factor histories. A strain gage of gage length 0.8 mm (CEA-13-032WT-120 from Vishay-Micromeritics Group, Inc.) was located at a radial distance of 5.5 mm from the crack tip and at an angle of 60° to the crack orientation. These specimens were impact loaded (impact velocity ~ 4.5 m/sec) in 3-point bend configurations using an Instron 9250-HV drop-tower. The strain history recorded was used to obtain crack initiation toughness values as detailed in Ref. [77]. Figure 3.4 shows the variation of mode-I crack initiation toughness (K_{ICR}) along the width of the sample. An approximately monotonic increase in the crack initiation toughness values can be seen at lower volume fractions (and lower values of E). Increase in crack initiation toughness by a factor of 1.5 is evident when glass filler volume fraction increases from 0 to 40% with a corresponding change in elastic modulus by a factor of 2.4.

3.3 Specimen surface preparation

Next, the specimens were prepared for optical tests. The cured sheets were removed from the mold and machined into test samples of dimensions 152 mm \times 42 mm \times 7.5 mm. The specimen surface was roughened using a #200 grit sandpaper. An optically flat

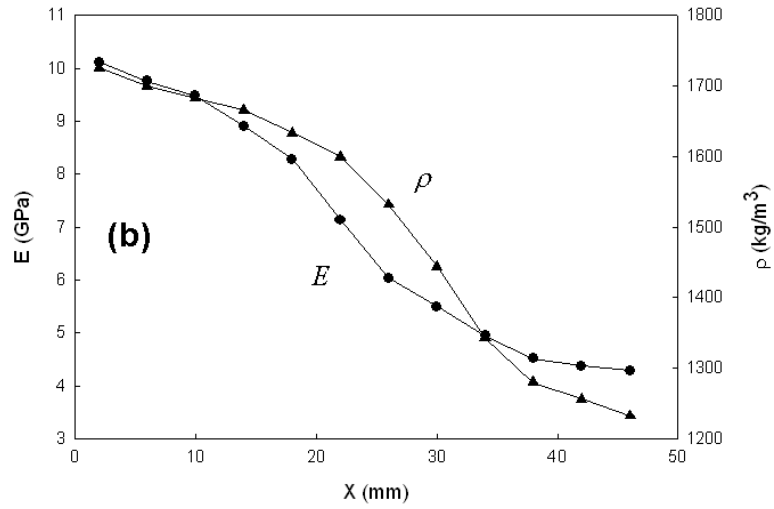


Figure 3.3: Variation of elastic modulus and mass density along the width of the sample

Borosilicate glass disk of 50 mm diameter was first coated with an aluminum film using vapor deposition technique. The region around the crack tip was made optically flat and specular by transferring the thin layer of aluminum film (~ 100 nm thick) coated on the glass disc using a layer of epoxy (5-10 μm thick). An edge crack (root radius ~ 150 μm) of length 8.6 mm ($a/W = 0.2$) was cut into the sample using a high-speed diamond impregnated circular saw.

3.4 Results

In this section, the role of material grading on fracture behavior of FGM is discussed by comparing crack tip position, crack speed and mixed-mode stress intensity factor histories between the two FGM configurations. The crack path history obtained from testing a homogeneous sample of same dimension under similar conditions was also compared with the FGM configurations.

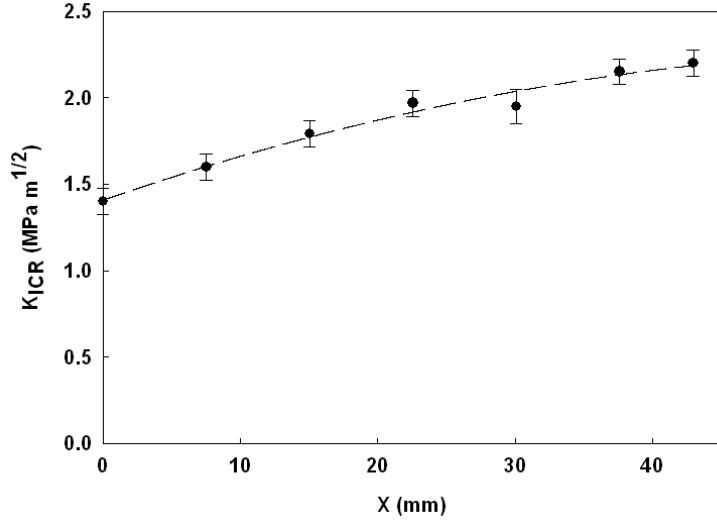


Figure 3.4: Variation of dynamic initiation toughness (impact velocity = 5.4 m/sec) with Elastic modulus. (Broken line is a trend line)

3.4.1 Experimental details

Mixed-mode fracture experiments conducted on FGM samples were of two types: (a) A crack on the compliant side of the sample with impact occurring on the stiffer side and (b) A crack on the stiffer side of the sample with impact occurring on the compliant side. A homogeneous sample having the same geometry and made out of Plexiglas was also tested under similar experimental conditions for comparative purposes. The two configurations of FGM and the homogeneous sample used in experiments are shown schematically in Figs. 3.5(a)–(c) as insets. Here, the elastic modulus at the edge of the cracked sheet behind the crack tip is denoted as E_1 and the one ahead of the crack tip as E_2 . With this notation, type-(a) experiments correspond to $E_1 < E_2$ and type-(b) experiments correspond to $E_1 > E_2$. Except for this change all other conditions are same for type-(a) and (b) experiments. Specimens were subjected to mixed-mode loading by impacting at an offset distance (S

= 25.4 mm) relative to the initial crack plane. Since specimen dimensions and all other experimental conditions are same, any difference in stress intensity factor histories, crack speed histories, and crack path are directly attributable to the compositional gradients.

A few representative fringes are shown in Fig. 3.5 for experiments conducted on two types of FGM samples as well as a homogeneous sample. In all the Figs. 3.5(a)-(c), the first two interferograms correspond to pre-initiation period, third image at a time instant when the crack was about to initiate and the fourth one is in the post-initiation period. The legends correspond to the time instant at which the image was recorded after impact. The impact point was located outside the window of observation and hence cannot be seen in these images. Once the impact occurs, the compressive stress waves originate at the impact point and travel through the specimen. They reflect from the bottom edge and sides of the sample as tensile waves and load the crack tip. At about 60 μs after impact, the crack tip experiences stresses large enough to exhibit fringes after which a monotonic increase in the number of fringes around the crack tip was seen. Two important observations can be made from these images. Firstly, fringes are seen for the case $E_1 < E_2$ when compared to $E_1 > E_2$ indicating more deformation around the crack tip when the crack is located on the compliant side. On the other hand, fewer fringes around the crack tip are seen when it is situated on the stiffer side. Secondly, the crack tip loading is essentially of the mixed-mode type. That is, one can see clearly tilting of fringe lobes towards the left of the initial crack indicating the presence of a negative shear component in the beginning. However, just before crack initiation, fringes tend to become symmetric with respect to the crack suggesting initiation under a predominantly mode-I condition accompanied by a vanishing K_{II} .

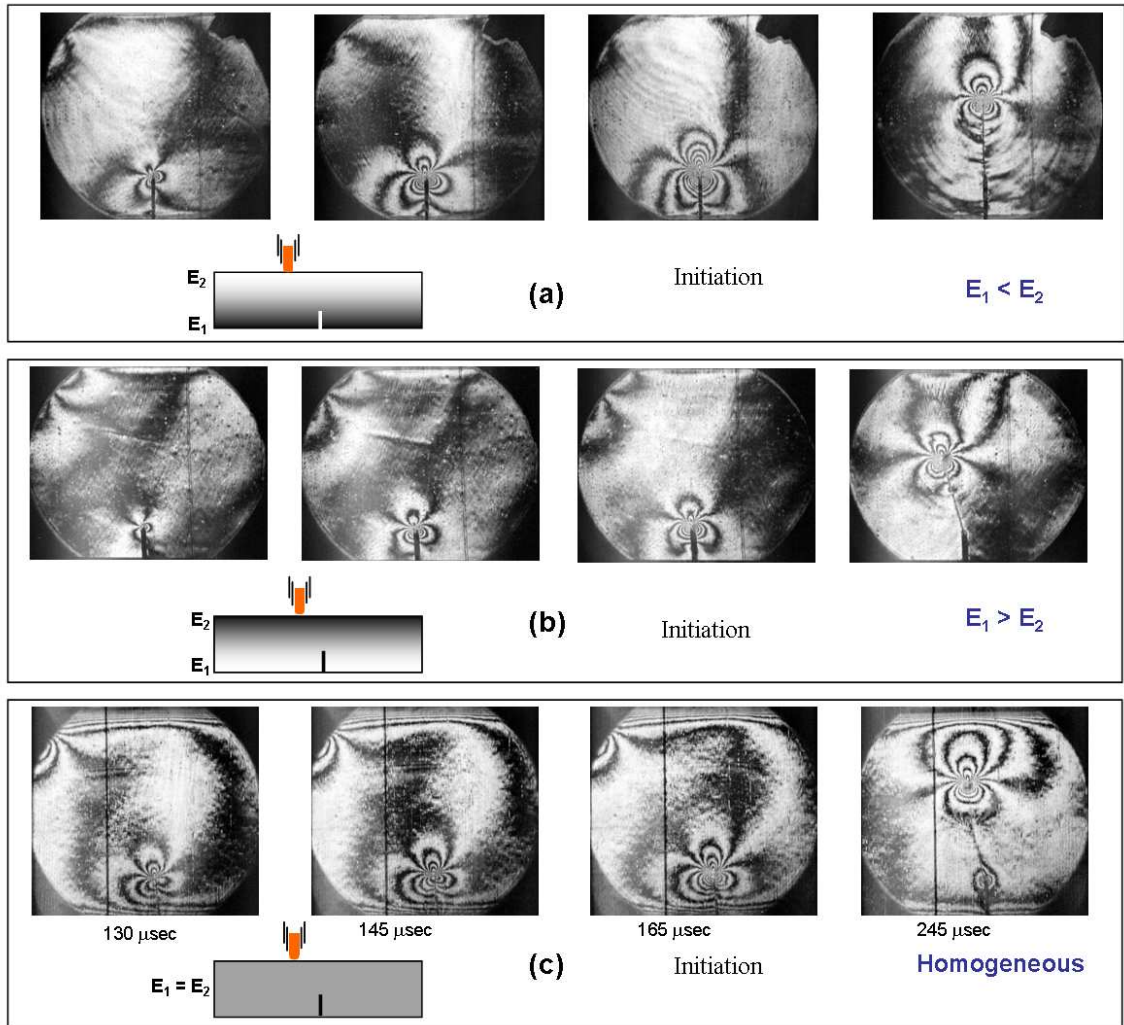


Figure 3.5: Selected CGS interferograms representing contours of $\delta w/\delta x$ in FGM and homogeneous samples. (The vertical line is at 10 mm from the crack). (a) crack on the compliant side and (b) crack on the stiffer side (c) homogeneous (Plexiglas) sample.

3.4.2 Crack growth and crack speed histories

A number of experiments (typically 3-4) were conducted for both configurations $E_1 < E_2$ and $E_1 > E_2$ to ensure repeatability. In the following, results are presented for a representative experiment of each configuration. Figure 3.6(a) shows crack growth histories for both experiments. The crack initiates at about $145 \mu\text{s}$ when it is situated on the stiffer side and at about $160 \mu\text{s}$ when on the compliant side. This is consistent with the fact that more crack tip deformation occurs for the case $E_1 < E_2$ than $E_1 > E_2$ as evidenced by a relatively large number of fringes in Fig. 3.6(a) than in Fig. 3.6(b). Also, the slope of the crack growth history curve is steeper for $E_1 < E_2$ indicating an overall higher crack speed in this case.

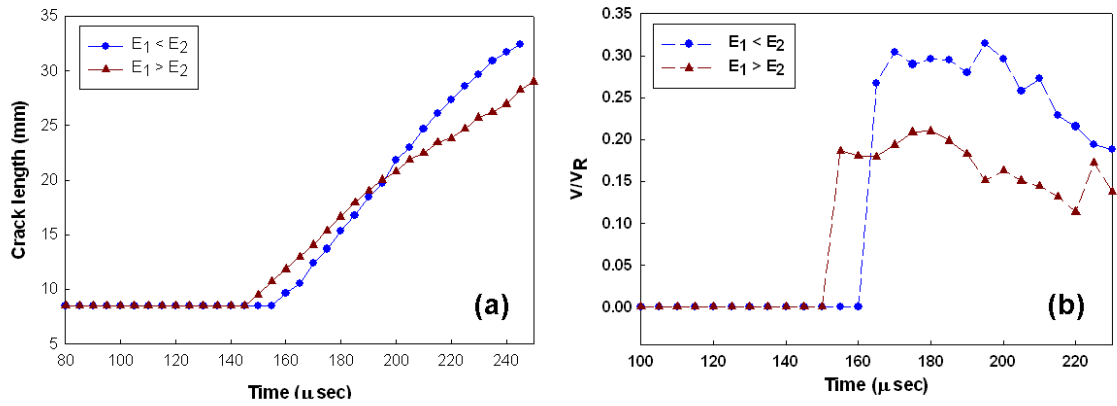


Figure 3.6: Crack growth behavior in FGM samples under mixed-mode dynamic loading. (a) Crack growth history, (b) normalized crack speed history. (V_R : local Rayleigh wave speed)

The crack speed histories were computed from crack growth histories and are shown in Fig. 3.6(b). Here, the crack speeds are normalized using the local Rayleigh wave speed (V_R). The crack speed histories indicate that the crack accelerates following initiation to

a maximum value with a subsequent oscillatory behavior it is driven forward by discrete wave reflections from the boundaries of the specimen. Sudden acceleration after initiation is attributed to the finite root radius ($150 \mu\text{m}$) of the initial crack. The data suggests that the average crack speeds are approximately 310 m/sec ($0.3 V_R$) for $E_1 < E_2$ and 250 m/sec ($0.2 V_R$) for $E_1 > E_2$. This shows that crack speeds are generally higher when the crack is on the compliant side of the sample. Once the crack initiates, the normalized crack speed remains nearly constant until it propagates through the lower half of the specimen. Subsequently, the crack speed history shows a decreasing trend for both the configurations as the crack tip approaches the impact point.

3.4.3 Mixed-mode stress intensity factor histories

The stress intensity factors for both cases were extracted as explained previously and are shown in Fig. 3.7. In this plot, the crack initiation time is identified as ($t = 0 \rightarrow t_i$) so that the positive values correspond to the post-initiation period and the negative ones to the pre-initiation period. The stress intensity factors were initially computed by considering the K -dominant term ($N = 1$ in Eq. 2.18 or 2.21) and up to four higher order terms ($N = 6$) sequentially. After analyzing a few experiments, it was found that the K -dominant solution ($N = 1$) was inadequate to capture the mixed-mode stress intensity factor histories throughout the experiment. A two-term ($N = 3$ in Eq. 2.18) or a three-term ($N = 4$) solution was found to be stable and capture the overall fracture behavior. In Fig. 3.7(a) the mode-I stress intensity factor monotonically increases up to crack initiation. The rate of increase of in the stress intensity factor in the early stages of crack tip loading is about $3 \times 10^4 \text{ MPa } m^{1/2}/\text{s}$. Following crack initiation, a small dip in K_I is seen suggesting a

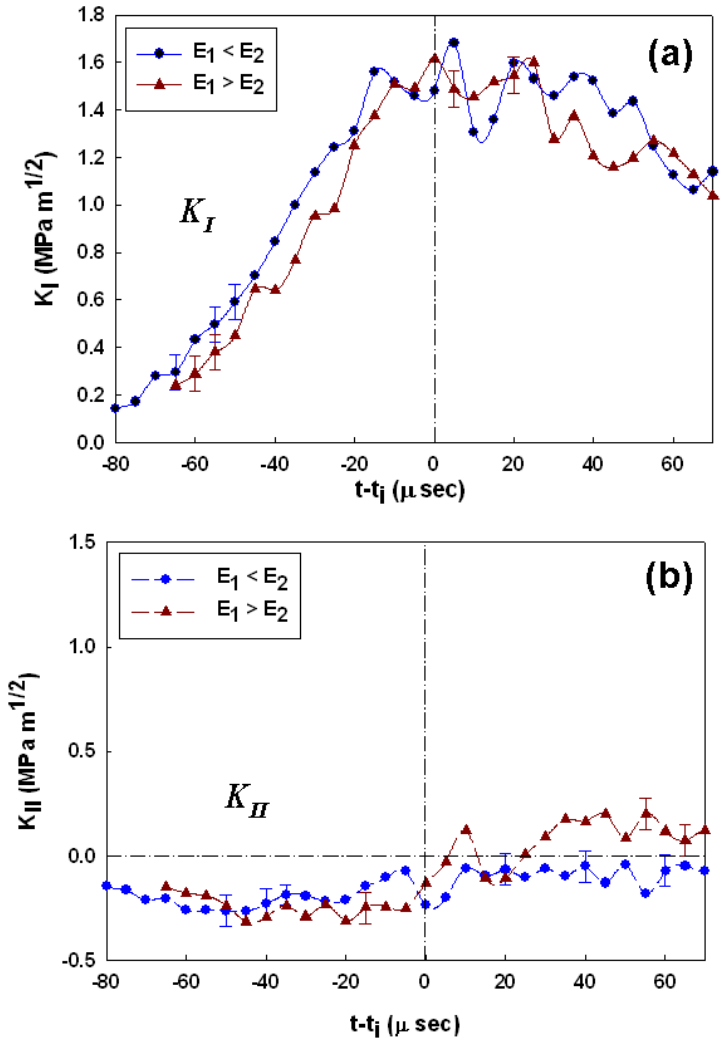


Figure 3.7: Mixed-mode dynamic stress intensity factor histories (impact velocity=5.2 m/sec). (Circles: $E_1 < E_2$, triangles: $E_1 > E_2$). (Time base is altered such that $t - t_i = 0$ corresponds to crack initiation)

sudden release of stored energy from the initial notch tip. After this drop, K_I values show a modest increase in case of $E_1 < E_2$ since the crack propagates into a gradually reinforced region with increasing volume fractions of the filler. However, for the case of $E_1 > E_2$, after initiation K_I gradually decreases in the observation window. The mode-II SIFs (Fig. 3.7(b)) for both FGM are initially negative and once initiation occurs, K_{II} continues to be at a small but negative value for $E_1 < E_2$ whereas it attains a small positive value for $E_1 > E_2$ within the observation window.

As mentioned earlier, a number of experiments (typically 3-4) were conducted for both configurations $E_1 < E_2$ and $E_1 > E_2$ to ensure repeatability. Four fractured samples from each configuration are shown in Fig. 3.8. A distinctly different crack path can be seen for these two configurations from Figs. 3.8(a) and (b). Also the repeatability of crack paths in each configuration for all four specimens can be readily noted. Figure 3.9 shows photographs of the fractured specimens for one representative experiment in each configuration. The impact point is located on the top edge of each image and the initial crack tip is at the bottom edge as indicated. The reflective area on each specimen surface is the region of interest where surface deformations are monitored during experimentation. A vertical line (on the right side of the crack for FGM samples and on the left side of the crack for homogeneous sample) seen in these figures is located 10 mm away from the crack tip to help establish the scale. In Fig. 3.9(a), the crack is on the compliant side ($E_1 < E_2$). Figure 3.9(b) corresponds to the opposite configuration ($E_1 > E_2$) and in Fig. 3.9(c), fractured Plexiglas specimen is shown. The striking feature in these images is the differences in crack paths in the lower half of the specimen. For the case $E_1 < E_2$, the crack initiation occurs almost like a mode-I crack with an *initial* kink angle of $\alpha \sim 4^\circ$ with respect to the X_1 -axis

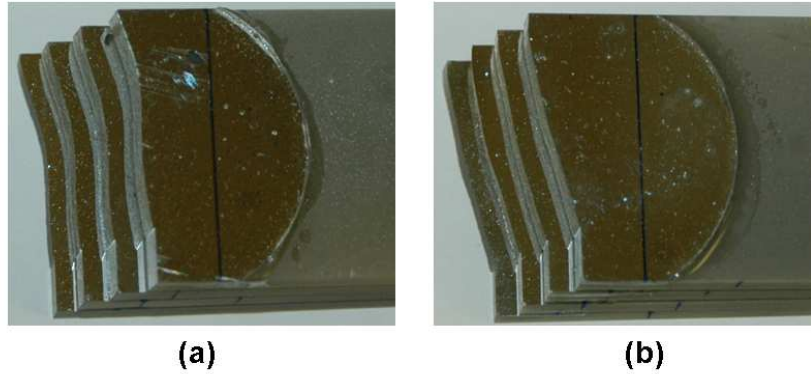


Figure 3.8: Photographs showing multiple fractured specimens (right half) demonstrating experimental repeatability **(a)** FGM with a crack on the compliant side ($E_1 < E_2$), **(b)** FGM with a crack on the stiffer side ($E_1 > E_2$).

whereas for the case $E_1 > E_2$, the crack growth occurs at an initial kink angle of $\alpha \sim 16^\circ$, (see Fig. 3.9(b)). Subsequent crack growth (say, ~ 4 mm beyond the initial growth) in $E_1 < E_2$ case shows a tendency for the crack to grow nearly along the X_1 -direction. On the other hand, in case of $E_1 > E_2$ the crack growth is essentially self-similar following initiation with a continued growth at an angle of $\sim 16^\circ$ with respect to the X_1 -axis. In the upper half of the sample, the crack growth is affected by a combination of free-edge and impact point effects. All the parameters (specimen dimensions, impact velocity, etc.) are same for these two experiments except for the reversal of compositional grading. Hence, the differences in the two crack paths are attributable directly to the respective compositional gradations (elastic as well as fracture toughness gradients). Having seen distinctly different crack paths for the above two configurations, homogeneous specimens made of Plexiglas were also tested under similar conditions and the resulting crack path is shown in Fig. 3.9(c). The crack shows an initial kink angle $\alpha \sim 10^\circ$ which is bounded by the ones observed in case of the two FGM configurations.

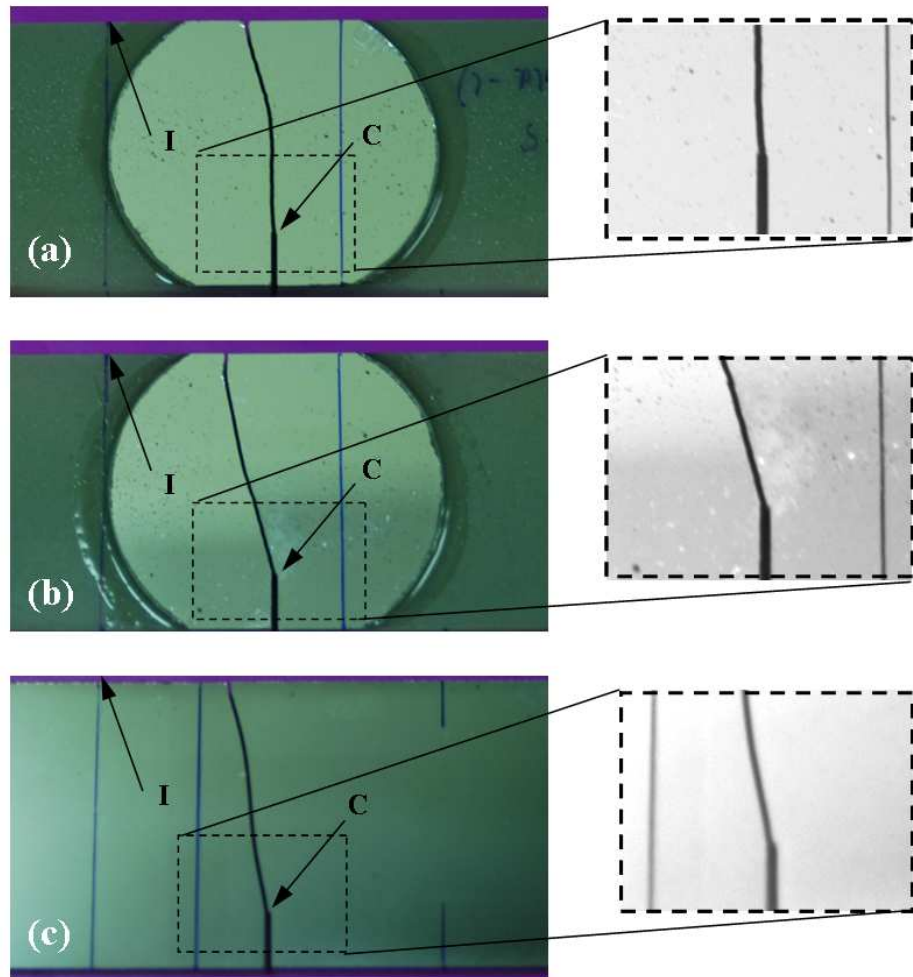


Figure 3.9: Photographs showing fractured specimens for (a) FGM with a crack on the compliant side ($E_1 < E_2$), (b) FGM with a crack on the stiffer side ($E_1 > E_2$) and (c) a homogeneous specimen. Impact point is indicated by letter 'I' and initial crack tip by letter 'C'

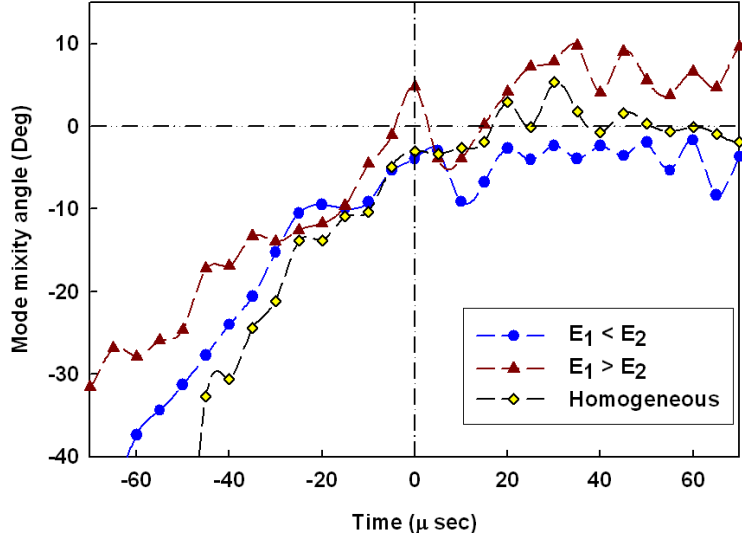


Figure 3.10: Crack growth behavior in FGM samples under mixed-mode dynamic loading. (a) Crack growth history, (b) normalized crack speed history. (VR: local Rayleigh wave speed)

The ratio of in-plane shear stress to normal stress near a crack tip can be quantified by the mode mixity $\psi = \tan^{-1}(K_{II}/K_I)$. The mode mixity histories for all the three cases are plotted in Fig. 3.10. A large negative value of ψ can be seen at the initial stages after impact indicating the presence of significant negative in-plane shear component at the crack tip. But just before crack initiation, ψ approaches zero. This suggests that crack initiated under dominant mode-I conditions in all the three cases. Once the crack initiates, ψ remains slightly negative for the case $E_1 < E_2$ and is slightly positive for $E_1 > E_2$ as shown in Fig. 3.10. Interestingly, for the case of a homogeneous sample, mode mixity is essentially zero (oscillations about zero) during propagation suggesting the possibility of crack growth in FGM occurring under conditions of nonzero K_{II} .

3.4.4 Initial crack path prediction

The maximum tangential stress (MTS) criteria introduced by Erdogan and Sih [78] is found to predict crack kink angles in FGM reasonably well under static loading conditions for glass-filled epoxy [25] and hence its validity in the current dynamic experiments is considered next. The MTS criteria states that the crack kinks in the direction of maximum tangential stress. Thus the crack kink angle α can be computed uniquely by solving the equation

$$K_I \sin \alpha + K_{II}(3 \cos \alpha - 1) = 0. \quad (3.2)$$

Here K_I and K_{II} are mode-I and mode-II stress intensity factors and the kink angle α is positive in the counter-clockwise direction in the usual crack tip coordinate system (see Fig. 2.3(b)). In this work, the crack kink angle at initiation was predicted based on SIF histories 10 μs (2 frames) prior to initiation. Thus predicted kink angle was verified by the observed angle near the initial crack tip. The crack kink angle in experiments was determined from interferograms using MATLABTM as follows. The images corresponding to post-crack initiation regime were loaded into the software environment. First, a point corresponding to the current crack tip was located. Then, a second point was located on the crack establishing a tangent to the current crack path. By using these two points, horizontal and vertical components of crack extension were identified and α was calculated. A third point was marked on the initial crack tip to continuously track the current crack tip with respect to the initial crack tip. The crack kink angle thus calculated was also verified by post-mortem examination of the fractured specimens.

Table 3.2 lists crack kink angles predicted by the MTS criteria using estimated SIFs from the two interferograms just before crack initiation. The crack initiation time is $\sim 160\mu s$

$E_1 < E_2$		$E_1 > E_2$	
Time (μs)	α	Time (μs)	α
150	7.9°	135	17.6°
155	5.8°	140	18.3°
Average	6.8°		17.9°

Table 3.2: Predicted crack kink angle based on estimated SIF data from CGS interferograms before crack initiation

$E_1 < E_2$		$E_1 > E_2$	
Time (μs)	α	Time (μs)	α
165	4.3°	150	16.8°
170	5.0°	155	16.4°
Average	4.6°		16.6°

Table 3.3: Observed crack kink angle from three CGS interferograms just after crack initiation

for $E_1 < E_2$ and $\sim 145\mu s$ for $E_1 > E_2$. It can be seen from Table 3.2 that the average kink angle is greater for $E_1 > E_2$ compared to $E_1 < E_2$. This indicates that the crack would kink more when it is situated on the stiffer side compared to the compliant side of the FGM. This can be readily verified from Fig. 3.9. The crack propagation in fractured specimens showing an initial crack growth (~ 10 mm) are shown as insets in Figs. 3.9(a) and (b) for $E_1 < E_2$ and $E_1 > E_2$, respectively. The observed kink angles are listed in Table 3.4.4 for 5 and 10 μs after crack initiation. It can be seen that the average crack kink angles predicted by the MTS criteria agrees reasonably well with the observed ones at the early stages of crack growth.

3.5 Mixed-mode SIF history from FGM crack tip fields

The SIF histories presented in Fig. 3.7 were computed using crack tip stress fields derived for homogeneous materials. However, in this section, SIFs computed by considering a 4-term expansion (terms associated with $r^{-1/2}, r^0, r^{1/2}, r^1$) of the asymptotic series for stresses which incorporates the variation of elastic modulus in the sample. The stress intensity factors, extracted as explained in Section 2.7 for both configurations, are shown in Fig. 3.11. In this plot, the crack initiation time (t_i) is identified as $t = 0$ so that positive values correspond to the post-initiation period and negative ones to the pre-initiation period. It should be noted here that SIF trends are somewhat different compared to the ones in Fig. 3.7 since they are affected by the non-homogeneity terms α_f and β_f (see Eq. 2.32). In Fig. 3.11(a), K_I increases monotonically up to crack initiation for both configurations. The value of K_I at crack initiation is roughly $1.5 \text{ MPa m}^{1/2}$ for both configurations. After crack initiation, K_I values show an increase in the case of $E_1 < E_2$ since the crack grows into a region with an increasingly higher volume fraction of the filler. However, for the case of $E_1 > E_2$ FGM after initiation, K_I gradually decreases in the observation window. This difference in K_I history in the post-initiation region is also confirmed by the finite element simulations (to be discussed in Chapter 7) where higher energy is absorbed when the crack is situated on the compliant side than on the stiffer side. The K_{II} (see Fig. 3.11(b)) values for both FGM configurations are initially negative and once initiation occurs, K_{II} continue to be a small but negative value for $E_1 < E_2$ whereas it attains a small but positive value for $E_1 > E_2$ similar to the results reported in Fig. 3.7.

The faithfulness of Eq. 2.34 to represent surface slopes observed in experiments is also tested. Thus, the synthetic contours generated from Eq. 2.34 are superimposed on

CGS interferograms obtained from experiments and are shown in Fig. 3.12. One image from the pre-initiation and one from the post-initiation time period is considered for both FGM configurations. It should be noted here that only the lobes behind the crack tip were digitized while performing over-deterministic analyses. Accordingly, the synthetic contours (order $N = -1, -1.5$ and -2) are superimposed on the back lobes of the respective interferograms. The least-square fit considering a 4-term FGM solution for the crack tip field shows a reasonably good fit with the optical data.

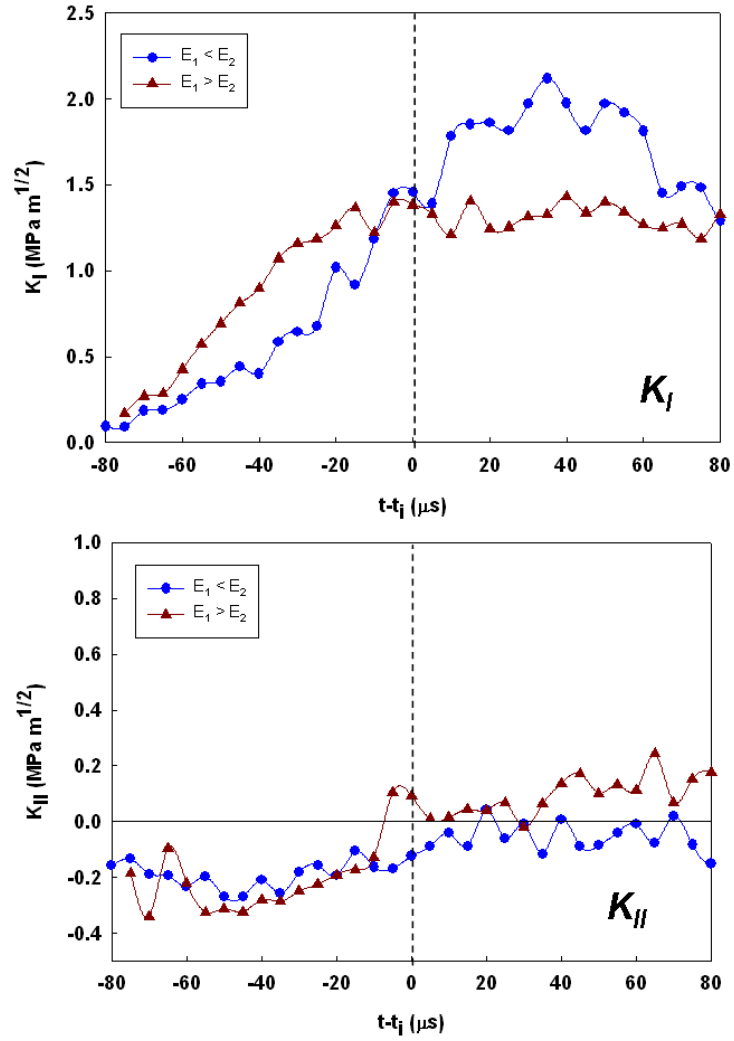


Figure 3.11: Stress intensity factors extracted from CGS interferograms by performing over-deterministic least-squares analysis on difference formulation of CGS governing equation formulated by using crack tip stress fields obtained for FGM with linear elastic modulus variation.

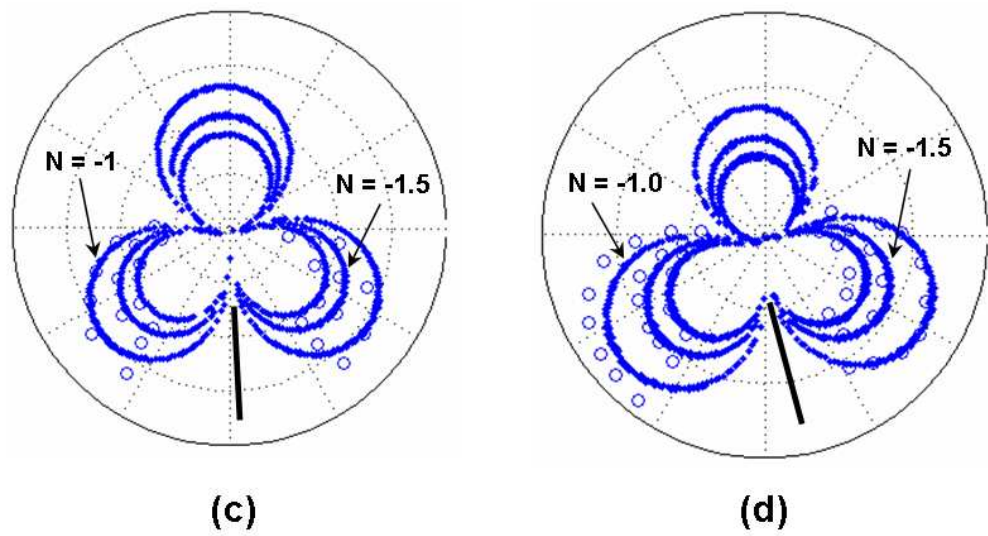


Figure 3.12: The quality of least-squares fit (plots of synthetic contours generated from Eq. 2.34 superimposed on collected data points) for **(a)** $E_1 < E_2$ ($t - t_i = 20 \mu s$) and **(b)** $E_1 > E_2$ ($t - t_i = -20 \mu s$).

CHAPTER 4

THE METHOD OF DIGITAL IMAGE CORRELATION

In this chapter, measurement of surface deformations and strains using the method of digital image correlation (DIC) is explained. A three-step approach is developed during this research for evaluating crack-tip displacements and strains from random speckle images. In the first step, a 2D cross-correlation coefficient is computed to obtain initial estimates of full-field in-plane displacements. In the second step, an iterative technique based on nonlinear least-squares minimization is implemented to refine the estimated displacements from the first step. In the third step, displacements are smoothed and strains are computed.

Next, the experimental set-up and test procedures for measuring transient surface deformations near a rapidly growing crack using a rotating mirror type ultra high-speed digital camera is detailed. Since the current work is the first of its kind using a newly introduced multi-channel high-speed digital camera system, calibration tests are conducted to estimate and correct misalignments between different optical channels. A series of benchmark experiments including intensity variability test, translation test and rotation tests are also conducted and the accuracy of measured displacements and strains are reported.

4.1 The approach

In the digital image correlation technique, random speckle patterns on specimen surface are monitored during a fracture event. These patterns, one before and one after the deformation, are acquired, digitized, and stored. Then a sub-image in the undeformed image is chosen and its location in the deformed image is sought. Once the location of a sub-image

in the deformed image is found, the local displacements can be readily quantified. In the current work, a three-step approach is developed in a MATLABTM [79] environment to estimate planar displacements and hence strains.

4.1.1 Initial estimation of displacements (Step-1)

In the first step, 2D cross-correlation is performed between two selected sub-images. The peak of the correlation function was detected to a sub-pixel accuracy ($1/16^{th}$ of a pixel) by bicubic interpolation. This process is repeated for the entire image to get full-field in-plane displacements. The method is briefly explained in the following. Consider two sub-images, $f(x, y)$ from undeformed image and $g(x, y)$ from the deformed image (Fig. 4.1(a)). Note that $g(x, y)$ can be approximated as a shifted copy of $f(x, y)$ with some random noise $\eta(x, y)$. That is, $g(x, y) = f(x - u, y - v) + \eta(x, y)$, where u and v denote displacements. The cross-correlation can now be performed in the frequency domain as [48],

$$P(\omega_x, \omega_y) = \frac{F(\omega_x, \omega_y)G^*(\omega_x, \omega_y)}{|F(\omega_x, \omega_y)G(\omega_x, \omega_y)|^{1-\alpha_p}} \approx |F(\omega_x, \omega_y)|^{2\alpha_p} e^{j2\pi(u\omega_x + v\omega_y)} \quad (4.1)$$

where F and G are Fourier transforms of $f(x, y)$ and $g(x, y)$, respectively, (ω_x, ω_y) denote the frequency domain variables and α_p is a constant which can be varied from 0 to 1. By performing Fourier transform of the function $P(\omega_x, \omega_y)$, a distinct peak in the second Fourier domain can be obtained as

$$\begin{aligned} G(k_x, k_y) &= \iint P(\omega_x, \omega_y) e^{-j2\pi(\omega_x k_x + \omega_y k_y)} d\omega_x d\omega_y \\ &= \iint |F(\omega_x, \omega_y)|^{2\alpha_p} e^{-j2\pi\{\omega_x(k_x - u) + \omega_y(k_y - v)\}} d\omega_x d\omega_y \\ &= G_{\alpha_p}(k_x - u, k_y - v), \end{aligned} \quad (4.2)$$

where (k_x, k_y) are frequency domain coordinates of the second Fourier domain. Determining u and v displacements of a sub-image then reduces to detecting the spatial location of the peak of the impulse function G_{α_p} accurately (Fig. 4.1(b)). The quality of the signal peak (impulse function) depends on the chosen value of the exponent α_p . If $\alpha_p = 0$ is chosen, it represents an ideal case (existence of zero noise in the images), and the spectrum relation of Eq. (4.1) becomes a pure phase field and the response will degenerate into a Dirac-delta function located at (u, v) . But in reality, due to the presence of noise, the signal peak is often suppressed. Therefore, it is necessary to make $P(\omega_x, \omega_y)$ a halo-weighted complex spectrum rather than a pure phase field by choosing α_p to be greater than zero. A systematic study about the selection of α_p and its effects on measured displacements can be found in [48]. In the current work, $\alpha_p = 0.25$ is adopted. This choice ensures good signal-to-noise-ratio and the probability of a distinct peak appearing at (u, v) is maximized.

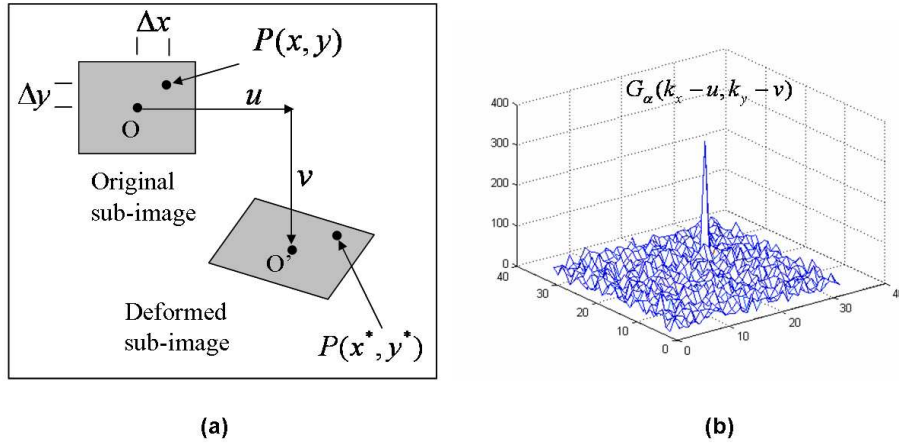


Figure 4.1: **(a)** Undeformed and deformed sub-images chosen from images before and after deformation, respectively and **(b)** typical plot of impulse response $G_{\alpha_p}(k_x - u, k_y - v)$ generated from cross-correlation between two sub-images.

4.1.2 Refining displacements (Step-2)

In this step, an iterative approach is used to minimize the 2D correlation coefficient by using a nonlinear optimization technique. The u and v displacements obtained in step-1 are used as initial guess values for the iterative scheme. The correlation coefficient is defined as [47],

$$s\left(u, v, \frac{\partial u}{\partial x}, \frac{\partial u}{\partial y}, \frac{\partial v}{\partial x}, \frac{\partial v}{\partial y}\right) = 1 - \frac{\sum_{i,j} [F(x_i, y_i) - \bar{F}] [G(x_i^*, y_i^*) - \bar{G}]}{\sum_{i,j} [(F(x_i, y_i) - \bar{F})^2] \sum_{i,j} [(G(x_i^*, y_i^*) - \bar{G})^2]}. \quad (4.3)$$

Here $F(x_i, y_i)$ is the pixel intensity or the gray scale value at a point (x_i, y_i) in the undeformed image and $G(x_i^*, y_i^*)$ is the gray scale value at a point (x_i^*, y_i^*) in the deformed image. The symbols \bar{F} and \bar{G} are the mean values of intensity matrices F and G , respectively (Fig. 4.1). The coordinates or grid points (x_i, y_i) and (x_i^*, y_i^*) are related by deformation between the two images. If the motion occurs in a plane perpendicular to the optical axis of the camera, then the relation between (x_i, y_i) and (x_i^*, y_i^*) can be approximated by a 2D affine transformation,

$$\begin{aligned} x^* &= x + u + \frac{\partial u}{\partial x} \Delta x + \frac{\partial u}{\partial y} \Delta y, \\ y^* &= y + v + \frac{\partial v}{\partial x} \Delta x + \frac{\partial v}{\partial y} \Delta y. \end{aligned} \quad (4.4)$$

Here u and v are translations of the center of the sub-image in X - and Y - directions, respectively. The distances from the center of the sub-image to a generic point (x, y) are denoted by Δx and Δy . Thus, the correlation coefficient s is a function of displacement components (u, v) and displacement gradients $(\partial u/\partial x, \partial u/\partial y, \partial v/\partial x, \partial v/\partial y)$. Therefore,

a search has to be performed for optimum values of displacements and their gradients such that s is minimized. In the current work, the Newton-Raphson method which uses line search and BFGS (Broyden, Fletcher, Goldfarb and Shanno) algorithm to update an inverse Hessian matrix is employed [80]. This method is applied in two phases. In the first phase, minimization is done in only a two variable (u, v) space by using the initial estimates from Step-1. In the second phase, minimization is carried out in a six variable space (displacements and displacement gradients) by using values for (u, v) from Step-1 and zeros for all the gradients. It should be noted here that estimation of displacements is accurate if the minimization is done in a six variable space rather than in a two variable space. However, the gradients obtained are quite noisy (especially when gradients are small as in the present work).

4.1.3 Smoothing of displacements and estimation of strains (Step-3)

The displacement gradients obtained during the correlation process represent average values for each subset and they tend to be noisy. Therefore it is necessary to apply smoothing algorithms to (u, v) fields in order to extract strains. There are a number of methods available in the literature to smooth the data [81, 82]. The one employed here uses an unbiased optimum smoothing parameter based on the noise level present in the displacement field. It should be noted here that displacements are discontinuous across the crack. A generic smoothing method tends to smooth displacements across the crack faces and hence strain concentration effects near the crack tip will be interpreted inaccurately. Therefore a smoothing method which allows discontinuity of displacements across the crack faces was introduced. A regularized restoration filter [83] with a second order fit was employed for

this purpose. This method minimizes the functional,

$$\phi(f) = \|g - Hf\|^2 + \alpha_s \|Lf\|^2, \quad (4.5)$$

where f is the displacement field to be restored and g is the noisy displacement field obtained from DIC method, both arranged in a single column format. In Eq. (4.5), H is a Point Spread Function (PSF) of a degradation model. The objective in the current work was to remove the random noise in order to restore/smooth displacement fields. Therefore, H was assumed as an identity matrix. The Laplacian operator ($\partial^2/\partial x^2 + \partial^2/\partial y^2$) is denoted by L in Eq. (4.5). Here α_s is a smoothing parameter selected on the basis of the noise present in the displacement field. The operation $\|\cdot\|$ denotes l^2 -norm of a vector. Now, Eq. (4.5) can be written as,

$$\phi(f) = (g - Hf)^T (g - Hf) + \alpha_s f^T L^T L f. \quad (4.6)$$

The above functional is minimized by differentiating $\phi(f)$ with respect to f and equating the result to zero. Upon simplification we get,

$$f = (H^T H + \alpha_s L^T S L)^{-1} H g, \quad (4.7)$$

where S is a diagonal matrix needed if a different amount of smoothing is desired in different parts of the image. In the current work, however, an identity matrix was used for S with appropriate diagonal elements set to zero to turn off smoothing across the crack. The Laplacian ($\partial^2/\partial x^2 + \partial^2/\partial y^2$) = $\nabla^2 f$ was found by defining a 3 x 3 discrete Laplacian kernel

as,

$$L(m, n) = \begin{bmatrix} 0 & 1 & 0 \\ 1 & -4 & 1 \\ 0 & 1 & 0 \end{bmatrix}. \quad (4.8)$$

The data points corresponding to the crack faces were excluded from this operation so that displacement discontinuity was preserved along the crack faces. The smoothing parameter α_s was so chosen that data infidelity satisfies the condition [81, 82],

$$\frac{1}{n} \sum_{j=1}^n [f(j) - g(j)]^2 = \sigma^2, \quad (4.9)$$

with n being the total number of data points. The quantity σ^2 is the variance of the noise present in the displacement data to be estimated by a calibration process. Once the displacements are smoothed, strains are obtained by numerical differentiation.

4.2 Static experiments

Before applying DIC technique to study dynamic fracture, a static experiment was conducted so that 2D in-plane displacements and strains evaluated from DIC can be compared with the ones obtained from finite element simulations. Figure 4.2(a) shows the experimental set-up used. The specimen coated with a random speckle pattern was illuminated by two light sources. A Nikon D100 digital camera with an objective lens (Nikkor 28-300 mm) was used to image the specimen surface. A bellows extension with sliding arrangement was used in between the camera and the lens in order to control the optical zoom. The specimen was loaded in three point-bend configuration (Fig. 4.2(b)) in a INSTRON 4465 loading frame. The actual photograph of the set-up is shown in Fig. 4.3. A central region of 45×30 mm of

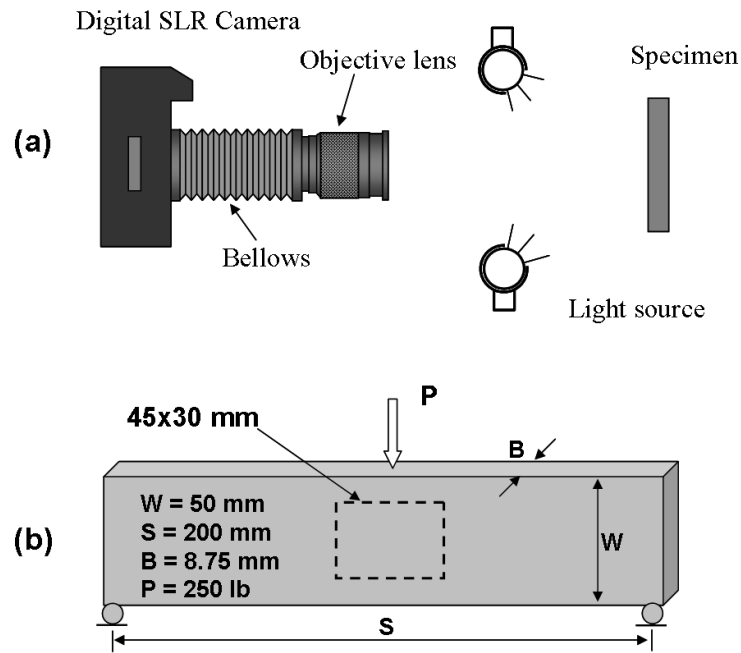


Figure 4.2: (a) Schematic of the experimental set-up for static experiment, (b) specimen and loading details

the specimen surface was imaged. The images recorded at load levels of 50 lbs and 300 lbs were correlated. The selection of the image at 50 lbs as reference image helped to preclude some of the initial rigid body displacements close to zero loads entering the analysis. The resolution of the image was 3000×2000 pixels. The sub-image size chosen for correlation was 32×32 pixels. The magnification used was such that one pixel represented $15 \mu\text{m}$ on the specimen surface.

The in-plane displacement results obtained from step-1, 2 and 3 are shown in Fig. 4.4. The sub-image size chosen was 50×50 pixels. The displacements obtained from step-1 look quite noisy in the figure, nevertheless, they serve as good guess values for step-2. Figure 4.5 shows few representative results from the static test. The full-field u -displacement and

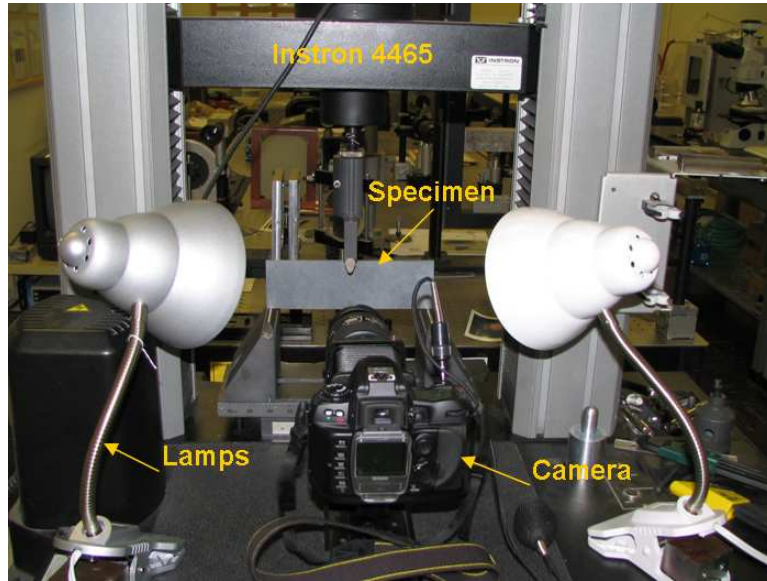


Figure 4.3: Photograph of the static experimental set-up

ϵ_{xx} -strain from DIC are shown in Figs. 4.5(a) and (b), whereas same results from FEA are shown in Figs. 4.5(c) and (d). The qualitative similarity between experimental and finite element results can be noted from these figures. The u -displacement and ϵ_{xx} -strain values along the section AA and BB were collected and plotted in Figs. 4.5(e) and (f). A close agreement (within $\sim 7.2\%$) between DIC and finite element results can be seen for u -displacement in Fig. 4.5(e). The ϵ_{xx} values obtained from experiments also agree with the ones from FEA but with a greater uncertainty (within 15%). This is expected since generally strains computed from DIC are less accurate when compared to displacements as a result of numerical differentiation. In these static experiments, displacements were resolved to an accuracy of 3 % of a pixel ($0.45 \mu\text{m}$) and the strain accuracy was about $108 \mu\epsilon$.

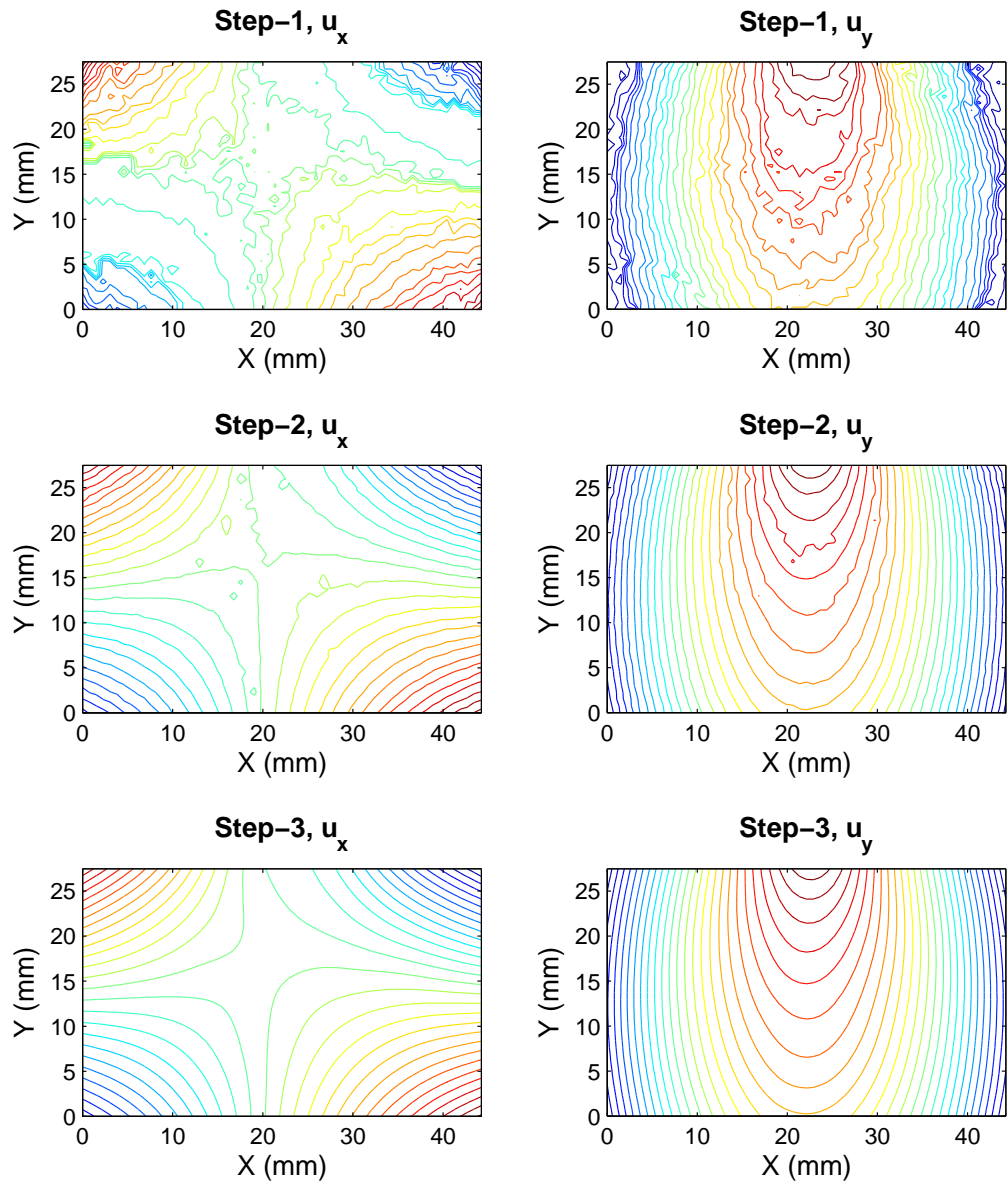


Figure 4.4: In-plane displacements obtained from Step-1, 2 and 3 of the image correlation process. The interval between contours is $7 \mu\text{m}$.

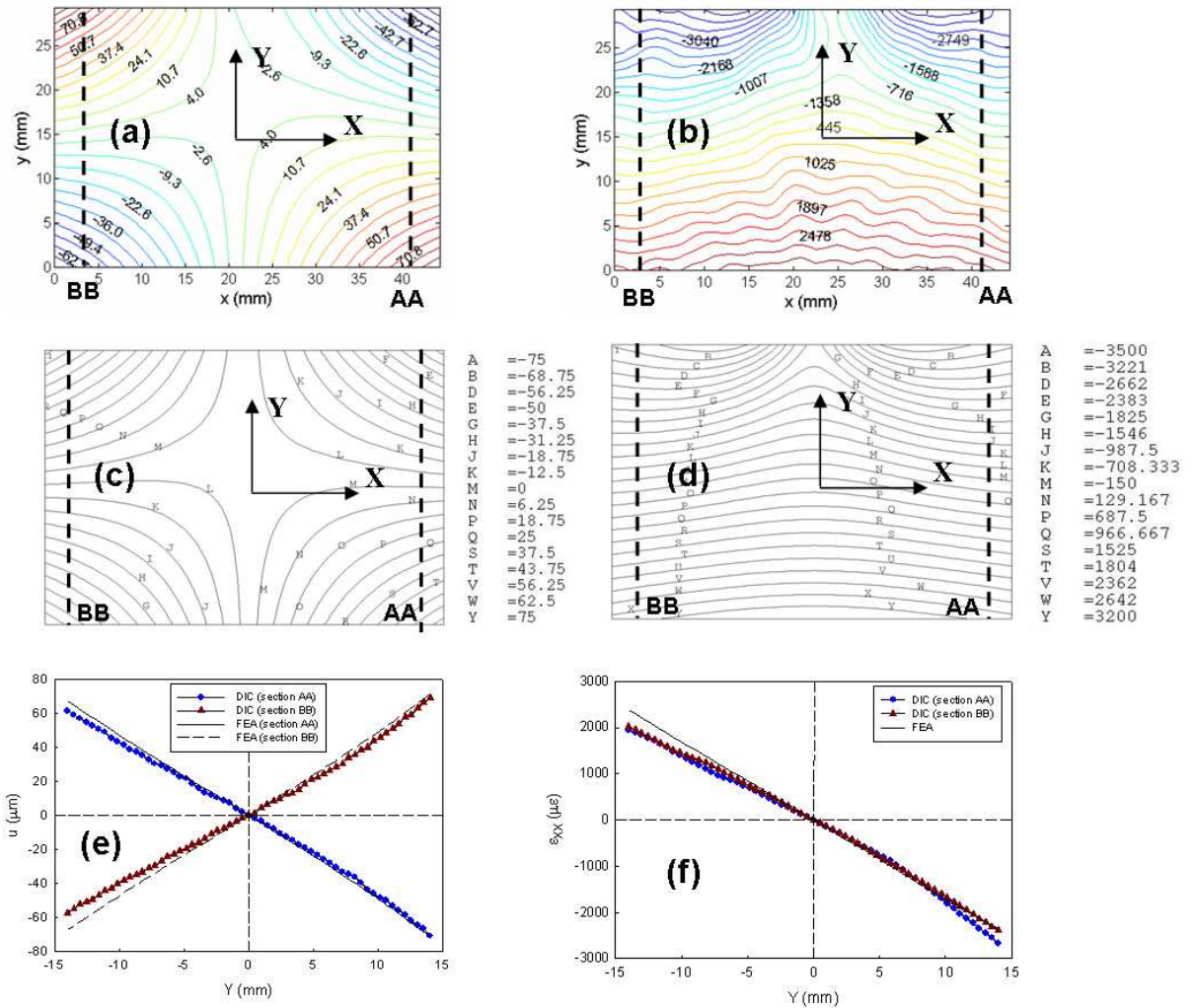


Figure 4.5: Static experimental results. (a) and (c) u -displacement (mm) from DIC and FEA, (b) and (d) ϵ_{xx} (μ -strain) from DIC and FEA, (e) and (f) u -displacement and ϵ_{xx} -strain at section AA and BB. Rigid body displacements have been subtracted out both in (a) and (c)

4.3 Dynamic experimental set-up

A schematic of the experimental set-up used in this study is shown in Fig. 4.6. It

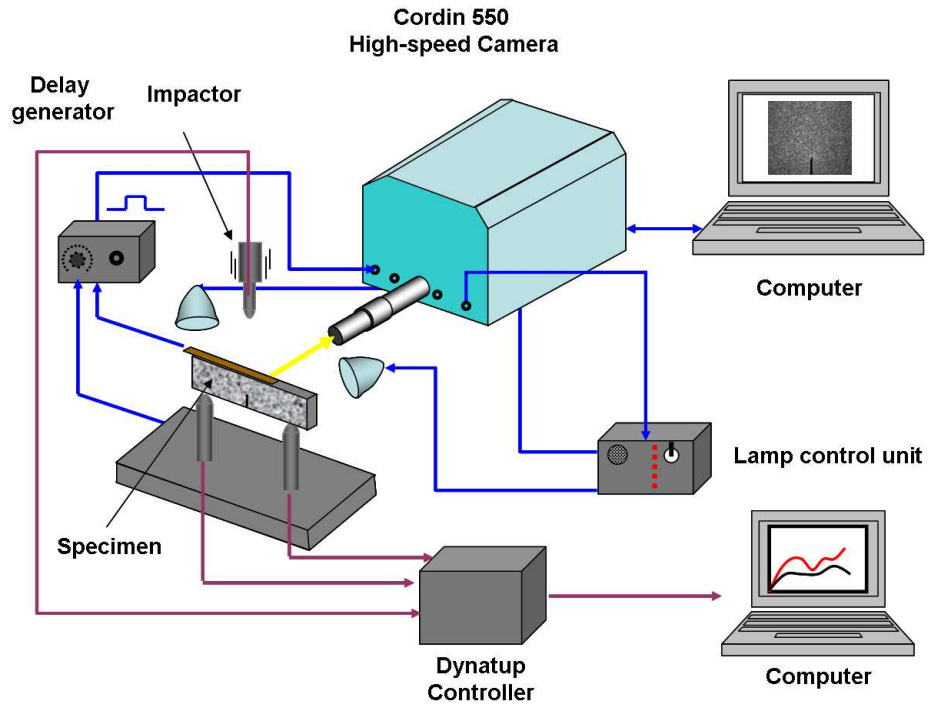


Figure 4.6: Schematic of the dynamic experimental set-up

consisted of a Instron-Dynatup 9250-HV drop-tower for impact loading the specimen and a Cordin 550 ultra-high-speed digital camera (with a 28-300 mm macro lens) for capturing the images in real-time. The drop-tower had an instrumented tup for recording the impact force history and a pair of anvils for recording support reaction histories. The set-up also consisted of a delay/pulse generator to generate a trigger pulse when the tup contacts the specimen. Since all the images were recorded during the event lasting over a hundred micro seconds, the set-up used two high-energy flash lamps, triggered by the camera, to illuminate the specimen. The set-up also utilized two computers, one to record the tup force and anvil

reaction histories (5 MHz acquisition rate) and the other to record the images. The actual photograph of the dynamic set-up is shown in Fig. 4.7.

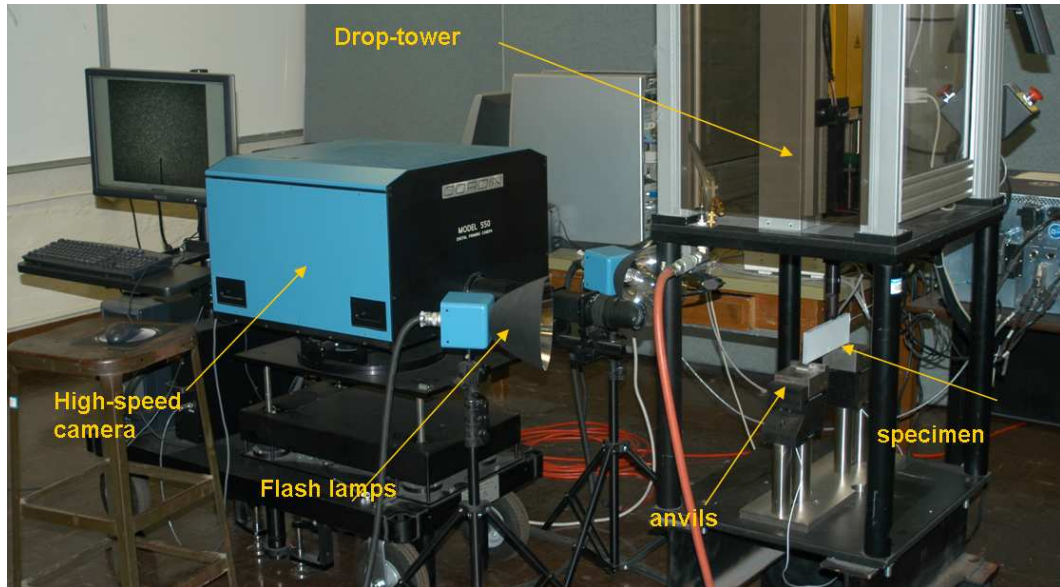


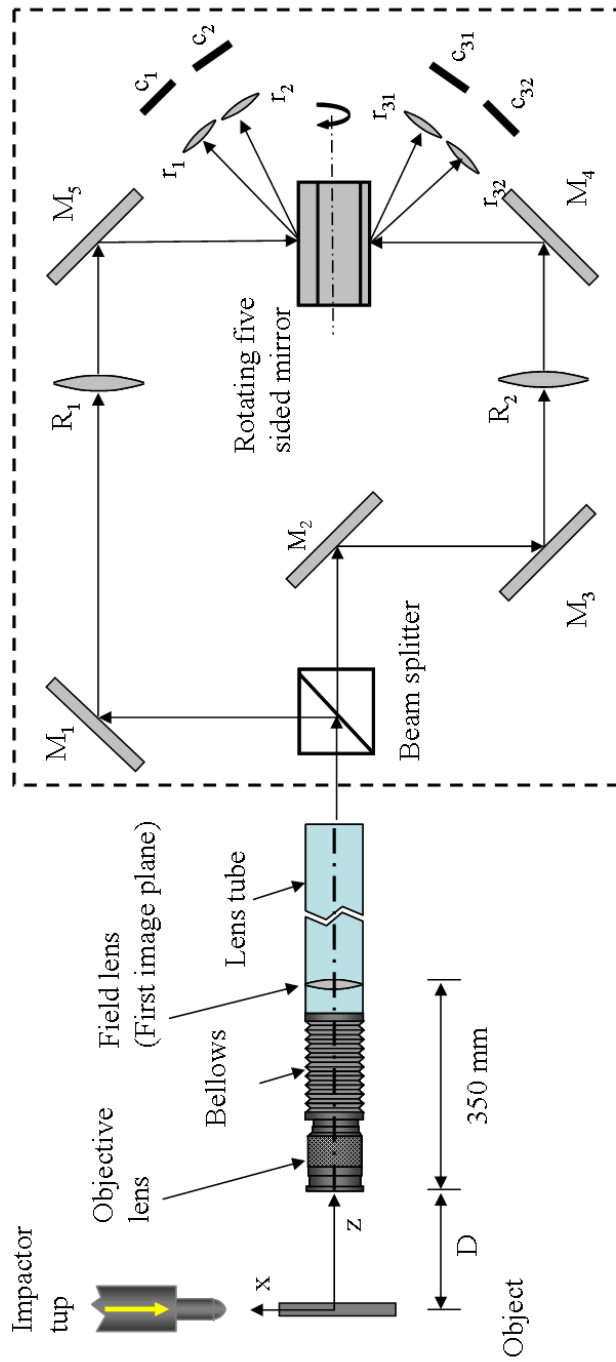
Figure 4.7: Photograph of the dynamic experimental set-up

The high-speed camera uses a combination of CCD based imaging technology and high-speed rotating mirror optical system. It can capture images up to 2 million frames per second at a resolution of 1K x 1K pixels per image. It has 32 independent CCD image sensors positioned radially around a rotating mirror which sweeps light over these sensors (Fig. 4.8). Each sensor is illuminated by a separate optical relay. Thus small misalignments between images are to be expected. (The effect of these parameters on displacement results are discussed in Sections 4.4 and 4.5). These misalignments preclude the possibility of image correlation between two images recorded by different CCD sensors. However, the above artifacts are absent between two images if they are captured by the same CCD sensor at two different time instants close to one another.

Therefore, the following approach was adopted. Prior to impacting the specimen, a set of 32 images of the specimen were recorded at a desired framing rate (200,000 frames per second in this work). While keeping all the camera settings (CCD gain, flash lamp duration, framing rate, trigger delay, etc.) same, next set of images, this time triggered by the impact event, were captured. For every image in the deformed set, there is a corresponding image in the undeformed set. That is, if an image in the deformed set was recorded by say sensor #10, then the image recorded by the same sensor #10 in the undeformed set was chosen for image correlation. *By doing this, the optical path could be maintained same for the two images under consideration and the only source of error now becomes the CCD noise which is in the range of 4 to 6 gray levels in an 8-bit intensity image (Section 4.5.1).* In order to get meaningful results, it is essential that no extraneous camera movements occur while recording a set of images and during the time-interval between the two sets of images. This was achieved by triggering the camera electronically.

4.4 High-speed camera calibration

As noted earlier, in the high-speed digital camera, different geometrical distortions are present in the images. This is because light travels through different optical paths (relays) before reaching individual CCD sensors, as shown in Fig. 4.8. In this work, the specimen was located at approximately 270 mm away from the objective lens. The field lens was about 620 mm away from the specimen. The image at the field lens was then relayed through various optical elements before being recorded by a sensor. For the camera system, four main types of misalignments in the images can be identified.



Cordin 550

Figure 4.8: Optical schematic of cordin-550 camera: M_1, M_2, M_3, M_4, M_5 are mirrors; R_1 and R_2 are relay lenses; r_1, r_2, \dots, r_{32} are relay lenses for CCDs; c_1, c_2, \dots, c_{32} are CCD sensors

- Focusing errors between frames: This aberration can be minimized by careful alignment of each optical path but cannot be entirely eliminated. However, since two images one before deformation and one after deformation, recorded from the same camera were correlated in the current work, this error does not affect measurements.
- Translation between two images: The images could have an in-plane (X - and Y - directions) relative translation of 5-7 pixels (out of 1000×1000 pixel image). Since the evaluation of fracture parameters depends primarily on locating the crack tip, translation of the whole image is not detrimental to the accuracy of results. However, these translations between frames were estimated accurately by calibration. Subsequently, the images were aligned to get good registration of one frame relative to the next.
- In-plane rotation between two images: The individual camera images could also have relative rotation (a maximum of 0.18° between the frames). This rotation was estimated accurately in the calibration experiment and then the frames were aligned with respect to each other.
- Perspective effect: In order to minimize errors due to perspective effects, camera needs to be located sufficiently far away from the specimen and the images must be recorded using higher $F^\#$ numbers. In the current experiment, the field lens was situated 620 mm away from the specimen and with an $F^\#$ of 5.6.

A calibration experiment was performed to quantify the above imperfections. The objective here was to estimate the correction parameters to be used later on for aligning each optical channel relative to a reference. A template with 5 x 5 array of targets (dark circles) was printed on a white glossy background and affixed to a flat surface. The camera was focused

on the template and flash lamps were adjusted to illuminate the targets uniformly. A set of 32 pictures of the template were recorded at 200,000 frames per second. Figure 4.9 shows a corresponding image recorded by one of the sensors. It should be noted here that calibration of the camera is needed only once before the actual fracture experiments. The various recording parameters (distance between the lens and the specimen, framing rate, magnification, etc) subsequently need to be maintained same between the calibration and real experiments.

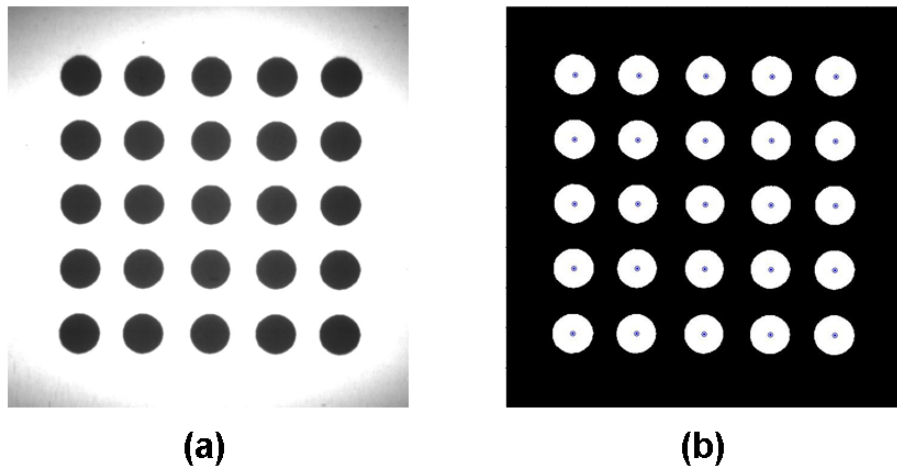


Figure 4.9: (a) Image of the 5×5 dot pattern template used for calibration experiment and (b) Inverted binary image of the template in order to find the control points

In the calibration experiment, distortions were corrected using a two-step process. In the first step, various correction factors were estimated between the images. To do this, one image was chosen as the base image and the distortions of all other 31 images (called input images) with respect to the base image were estimated. The base image and one of the input images were considered and histogram equalization was carried out on them. Then these images were converted into binary images by performing a thresholding operation

followed by an intensity inversion operation to get white circles with a black background (see Fig. 4.9(b)). The location of the center of each circle was estimated for both the base and input images. These center locations (also called control points) were further fine-tuned for the input image by performing normalized cross-correlation operation locally [84]. This operation matches the template in the neighborhood of a control point in the base image with that of an input image and fine-tunes the location of the control point of the input image. This process is repeated for all other 31 images and the control points for every base image-input image pair were stored.

In the second step, correction was applied to the real images recorded in an experiment based on the transform inferred from the control points. *Here it should be emphasized that no histogram equalization and thresholding operations were performed on real images.* The input image was transformed with respect to the base image by a linear conformal mapping transformation. In this transformation, shape of the input image was unchanged, but the image was deformed by some combination of translation, rotation, and scaling. That is, by doing this, straight lines remained straight and parallel lines remained parallel. The transformation used is given by,

$$\begin{pmatrix} x_i \\ y_i \end{pmatrix} = \begin{pmatrix} a_1 & b_1 \\ -b_1 & a_1 \end{pmatrix} \begin{pmatrix} x_b \\ y_b \end{pmatrix} + \begin{pmatrix} a_o \\ b_o \end{pmatrix}, \quad (4.10)$$

where (x_i, y_i) and (x_b, y_b) are coordinates of the input image and the base image, respectively. Also, (a_o, b_o) represent translations in the X - and Y - directions, respectively. The stretch and rotation are denoted by a_1 and b_1 . Since there are four unknowns in Eq. (4.10), two pairs of control points are sufficient to find these unknowns. Since there are 25 pairs

of control points (5×5 array of circles), the unknowns were determined in this work in an over-deterministic least-squares sense. The transformation structure generated from each pair of control points is listed in Table 4.1. Here the image from camera # 09 was chosen as the base image and misalignments of all other images with respect to this image are listed. It can be noted from this table that there is horizontal and vertical misalignment between the successive images. The horizontal movement is in the range of 0 to 9 pixels where as the vertical movement is in the range of 0 to 4 pixels. Rotation between the frames is within 0.003 radians. As noted earlier, for every experiment, two sets of images were recorded, one set before impact loading and another set after. The above transformation was applied for both the sets. That is, if a control points pair came from analyzing images of sensors 1 and 10 (1 being the base image and 10 being the input image) of the reference image set, then the transformation was also applied to the images captured by sensors 1 and 10 in the undeformed set as well as the deformed set. The two images from the same camera were then correlated (that is, between the images captured by sensor 10 of the undeformed set and the deformed set). *Again it should be noted here that since the same transformations are applied to both the undeformed and deformed images, they would not influence measured deformations but improve the quality of sequential displaying (or animation) of images helpful in visualizing the failure process.*

4.5 Benchmark experiments for high-speed camera

In view of the presence of distortions/misalignments in the camera system, it becomes important to assess the camera performance to measure transient deformations in a dynamic

	a_1	b_1 (radians)	a_o (pixels)	b_o (pixels)
Camera 00	0.9966	0.0003	1.3468	1.9695
Camera 01	0.9997	0.0004	-0.4052	-1.0066
Camera 02	0.9986	0.0003	0.7136	0.8484
Camera 03	1.0006	0.0002	-1.7187	0.0524
Camera 04	0.9986	-0.0009	0.5622	-0.1669
Camera 05	1.0001	-0.0003	-1.1137	-0.3886
Camera 06	1.0002	0.0007	-2.2279	-0.3266
Camera 07	1.004	0.0029	-6.5381	2.656
Camera 08	1.007	0.0056	-3.7658	-1.05
Camera 09	1.0000	0.0000	0.0000	0.0000
Camera 10	0.9983	-0.0019	0.0058	-0.9471
Camera 11	0.9995	-0.0012	1.6056	-1.9433
Camera 12	0.9946	-0.0003	8.1177	-0.6218
Camera 13	1.0003	0.0002	0.318	-0.2026
Camera 14	0.998	-0.0015	2.2551	-0.7557
Camera 15	0.9961	0.0005	2.6524	3.1431
Camera 16	0.9939	-0.0017	9.4083	1.9072
Camera 17	0.9977	-0.0005	4.6258	-0.7484
Camera 18	0.9984	-0.0003	5.4465	-1.8866
Camera 19	0.9969	-0.0013	4.5083	-1.7703
Camera 20	0.999	-0.0008	3.8725	-1.873
Camera 21	1.0000	-0.0009	3.2238	-3.2697
Camera 22	0.9993	-0.0011	4.8201	-2.9866
Camera 23	1.0018	-0.0008	3.2343	-3.8285
Camera 24	0.9998	0.0006	3.7571	-1.9882
Camera 25	1.0017	-0.0012	1.4998	-4.764
Camera 26	0.999	0.0001	1.7903	-1.4227
Camera 27	0.9976	-0.0012	4.97	-0.3825
Camera 28	0.9999	-0.0007	4.1851	-2.8842
Camera 29	0.9984	-0.0014	4.5328	-2.8868
Camera 30	1.0002	-0.0019	4.1973	-3.5948
Camera 31	0.9995	-0.0016	3.2673	-2.8311

Table 4.1: Alignment differences between individual optical channels of Cordin-550 camera; Stretch, rotation and translations of different images with respect to the image taken by camera # 09

test. Therefore certain benchmark tests - image intensity variability test, translation text and rotation tests were conducted.

4.5.1 Intensity variability test

In the current work, 8-bit (0 to 255 gray levels) images were captured and analyzed. The CCD noise in these images was first estimated. The CCD noise in an acquired image depends on the value of CCD gain that can be pre-set in the camera on a scale of 0 to 1000 before conducting an experiment. For all the experiments reported in this work, this value was set in the range of 500 to 550. A value of 700 becomes an upper limit since it results in saturation of a few pixels in the acquired images and hence was avoided. Thus, two sets of 32 images were acquired at framing rates of 200,000 and 50,000 frames per second in total darkness (with the lens cap on). All the images in these two sets had their pixels representing the gray scale values in the range of 0 to 8. Thus, it can be said that lower 3 bits in an 8-bit image represents CCD noise and the intensity represented by the remaining 5 bits can be faithfully measured. Figure 4.10 shows the mean and standard deviations of intensity values of all pixels (1 million pixels in a 1000x1000 pixel image) in various images captured in darkness. It can be seen from this figure that all the images have their mean intensity values in the range 6 to 8 with a relatively narrow spread (standard deviation in the range 2 to 4).

As already mentioned, in the current work, transient deformations are estimated by performing image correlation between two images acquired from the same CCD sensor, one before the impact and another after the impact. Therefore it is important to know the intensity variations between two images recorded by the same CCD sensor at different

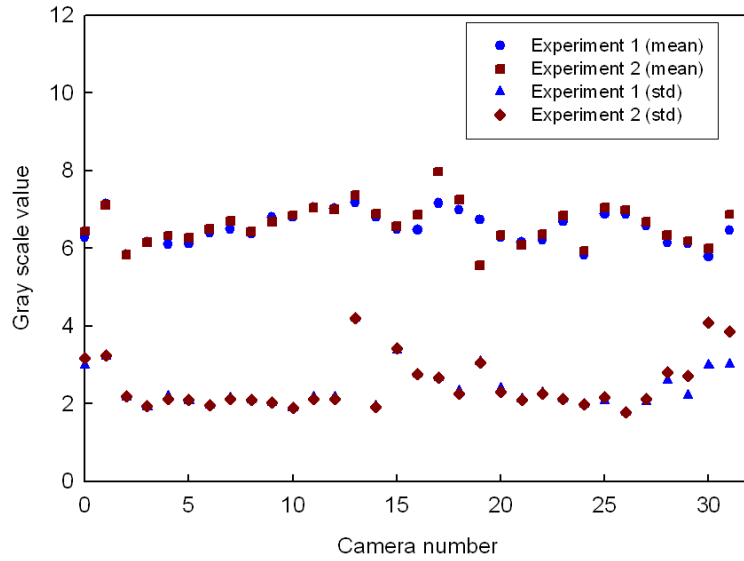


Figure 4.10: Mean and standard deviations of intensity values of images acquired in total darkness (with lens cap on). Images were recorded at 50,000 frames per second in experiment 1 and at 200,000 frames per second in experiment 2.

times. To this end, five sets of 32 images of a stationary sample, decorated with random speckle pattern, were acquired at 200,000 frames per second. The gray scale values at a few randomly chosen pixels were stored (same set of random pixels were chosen from all the images). The intensity values at a particular pixel from all the five images acquired by the same CCD sensor was examined. This variation is shown in Table 4.2 for all the 32 CCD sensors. Significant difference in intensity value at a pixel is observed between images acquired by different CCD sensors. More importantly, a very small variation in gray scale value at a pixel from images acquired by the same CCD sensor can be seen. Thus, the standard deviation values are in the range 2 to 6 gray levels for most of the CCD sensors (apparently this is in the same range as the standard deviation values observed for the images recorded in total darkness, see Fig. 4.10). This demonstrates that between an undeformed and deformed image registered during an actual experiment, there are no

Camera #	Set 1	Set 2	Set 3	Set 4	Set 5	Mean	St. dev
00	121	116	123	120	122	120.4	2.7
01	106	102	104	108	102	104.4	2.61
02	119	120	125	116	120	120	3.24
03	93	95	111	109	102	102	8.06
04	122	125	126	116	120	121.8	4.02
05	97	102	106	105	105	103	3.67
06	106	97	108	112	103	105.2	5.63
07	79	80	74	82	74	77.8	3.63
08	84	81	84	89	84	84.4	2.88
09	123	118	128	129	129	125.4	4.83
10	111	105	110	114	116	111.2	4.21
11	118	112	111	110	117	113.6	3.65
12	82	88	76	82	82	82	4.24
13	117	115	115	114	117	115.6	1.34
14	88	98	93	87	93	91.8	4.44
15	94	96	93	92	91	93.2	1.92
16	77	73	73	77	72	74.4	2.41
17	63	60	59	65	63	62	2.45
18	97	93	92	93	98	94.6	2.7
19	76	66	71	72	72	71.4	3.58
20	69	70	60	71	67	67.4	4.39
21	87	86	93	95	85	89.2	4.49
22	114	109	113	115	110	112.2	2.59
23	82	80	79	82	76	79.8	2.49
24	92	89	93	96	84	90.8	4.55
25	124	119	120	130	122	123	4.36
26	122	120	126	117	123	121.6	3.36
27	78	83	86	79	78	80.8	3.56
28	76	74	73	77	70	74	2.74
29	95	93	92	91	96	93.4	2.07
30	73	71	70	71	69	70.8	1.48
31	95	91	95	96	88	93	3.39

Table 4.2: Gray scale values at a particular pixel in five repeated sets of images of speckle pattern acquired at 200,000 frames second. Note the repeatability of the gray scale values between different sets of images.

abrupt light intensity variations apart from the random CCD noise. This is a rather subtle but important point to note. Also it is unique to this type of high-speed camera system where one can perform image correlation between two images acquired from the same CCD sensor to obtain highly accurate displacements.

4.5.2 Translation test

In this experiment, a specimen (decorated with random b/w speckles) was mounted on a 3D-translation stage, as shown in Fig. 4.11. A series of known displacements were

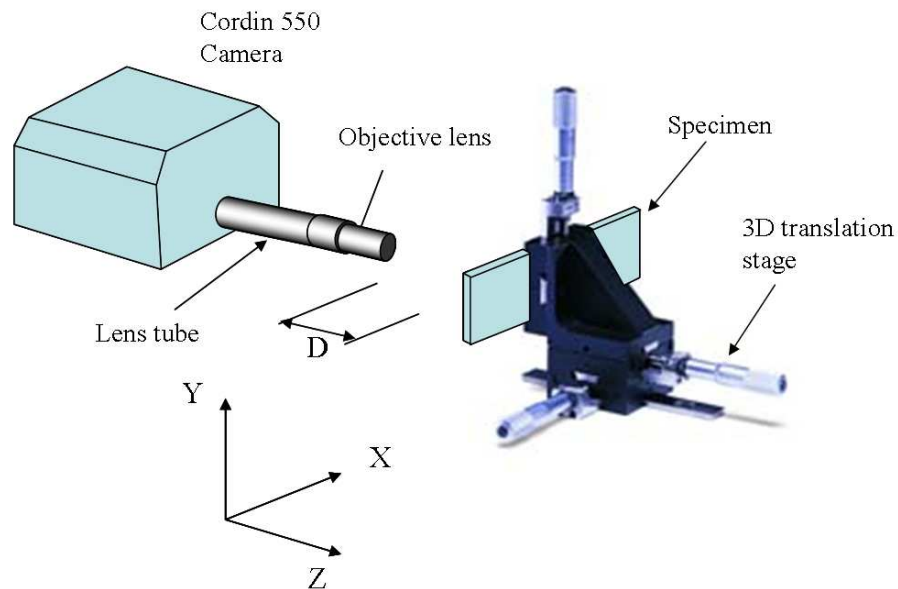


Figure 4.11: Experimental set-up for conducting translation test for high-speed digital camera

imposed in the X - and Y - directions separately and the images were captured. The mean and standard deviations of the displacement fields were computed and compared with the applied displacements. Also, a small out-of-plane (Z -direction) displacement of $30 \pm 2\mu\text{m}$

¹ was applied to the sample and a set of images were captured. The objectives of these translation tests were as follows:

- To estimate noise levels in the measured in-plane displacement fields (or, to determine the smallest in-plane displacement that can be measured reliably from the camera system).
- To compare displacement fields obtained by the 32 individual cameras when they are used to measure the same applied displacement.
- To determine the effect of out-of-plane displacement on the accuracy of measured in-plane displacements (or, to address the issue of whether the accuracy of in-plane displacements is affected if the sample undergoes a small out-of-plane deformation during an experiment).
- To determine the effect of variation in the working distance (D) distance between the sample and the objective lens (see Fig. 4.11), on the quality of the measured in-plane displacements.

The details of translation tests are given in Table 4.3. Totally six sets of 32 images were recorded in each configuration. In Configuration-1, the objective lens of the camera was 400 mm away from the sample. The first set of 32 images of the undeformed sample makes Set-1. In Set-2 and Set-3, images were recorded after applying $60 \pm 2\mu\text{m}$ of translation in the X -direction and $60 \pm 2\mu\text{m}$ translation in the Y -direction, respectively. This is typically

¹This is typically the amount of out-of-plane displacement that occurs in the vicinity of a crack tip in an experiment conducted in this work. For example, in Ref. [17] one can see roughly 7-9 interferometric (CGS) fringes near the crack tip over a distance of ~ 10 mm. Since these fringes represent surface slopes and the resolution of the set-up was $\sim 0.015^\circ/\text{fringe}$, one can estimate the out-of-plane displacement around the crack tip to be $\sim 23 \mu\text{m}$.

the deformation level observed in the current tests. In Set-4 and Set-5, specimen was translated by $300 \pm 2\mu\text{m}$ in the X - and $300 \pm 2\mu\text{m}$ the Y -direction, respectively. These represent the amount of rigid body displacements expected in the dynamic tests. In Set-6, images were recorded after applying $30 \mu\text{m}$ translation in the Z -direction. The same exercise was repeated for Configuration-2 where the camera was kept twice as close as in Configuration-1. It should be noted here that all these translations were applied manually by micrometers in a xyz -translation stage.

<i>Configuration 1</i>		<i>Configuration 2</i>	
<i>Working distance (D) = 400 mm</i>		<i>Working distance (D) = 200 mm</i>	
<i>Magnification = 35.6 $\mu\text{m}/\text{pixel}$</i>		<i>Magnification = 27 $\mu\text{m}/\text{pixel}$</i>	
Set 1	Undeformed	Set 1	Deformed
Set 2	X -translation = $60 \pm 2\mu\text{m}$	Set 2	X -translation = $60 \pm 2\mu\text{m}$
Set 3	Y -translation = $60 \pm 2\mu\text{m}$	Set 3	Y -translation = $60 \pm 2\mu\text{m}$
Set 4	X -translation = $300 \pm 2\mu\text{m}$	Set 4	X -translation = $300 \pm 2\mu\text{m}$
Set 5	Y -translation = $300 \pm 2\mu\text{m}$	Set 5	Y -translation = $300 \pm 2\mu\text{m}$
Set 6	Z -translation = $30 \pm 2\mu\text{m}$	Set 6	Z -translation = $30 \pm 2\mu\text{m}$

Table 4.3: Details of translation tests: Six sets of 32 images were recorded in each configuration. In Configuration-2, the camera was kept twice as close as in Configuration-1.

The full-field displacements were computed for all these tests. The sub-image size chosen was 30×30 pixels which gave $32 \times 32 = 1024$ data points for a $1K \times 1K$ image. The results shown in Figs. 4.12(a) and (b) are: (i) the mean and standard deviations of u -displacement (between images of Set-1 and Set-2 of Configuration-1, ‘solid circle’), (ii) the mean and standard deviations of v -displacement (between images of Set-2 and Set-3 of Configuration-1, ‘solid square’), (iii) mean and standard deviations of u -displacement (between images of Set-1 and Set-2 of Configuration-2, ‘solid triangle’) and (iv) mean and

standard deviations of v -displacement (between images of Set-2 and Set-3 of Configuration-2, ‘solid diamond’). Tests were conducted in Configuration-2 to examine the effect of the

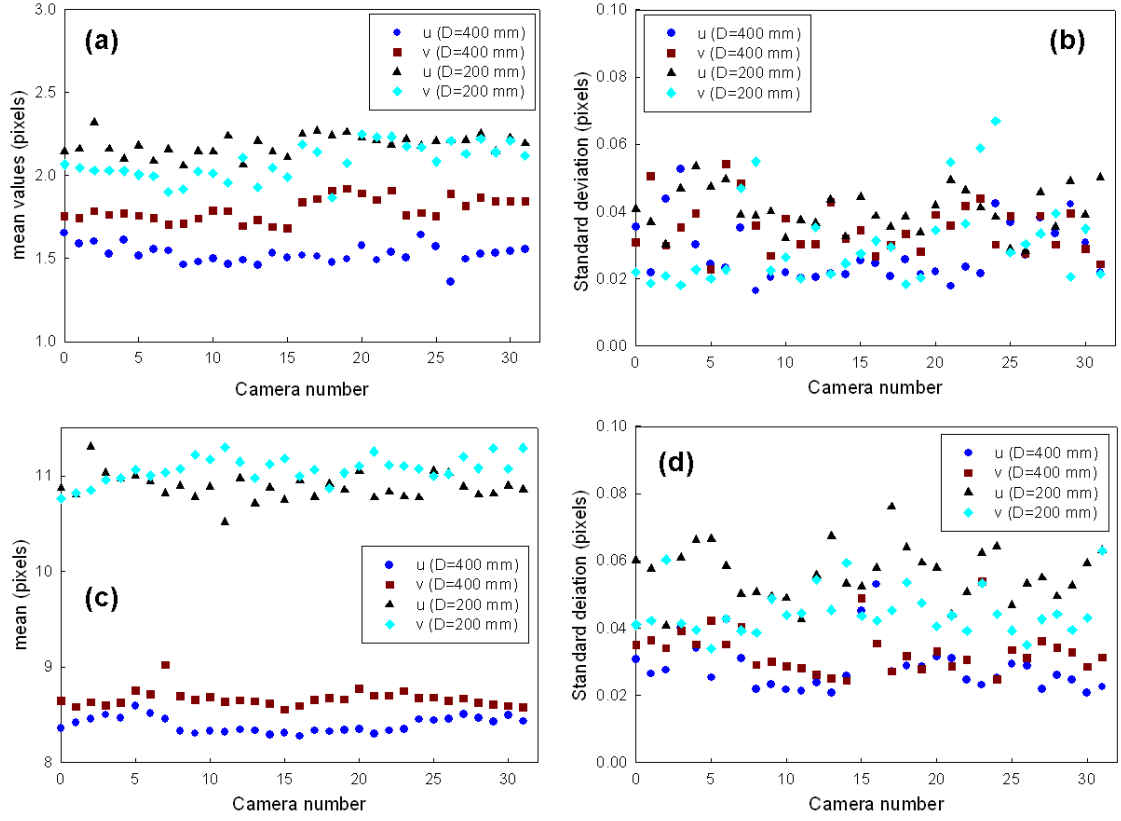


Figure 4.12: Translation test results for $D=400$ mm and 200 mm (see Fig. 4.8). (a) mean and (b) standard deviations of u - and v - displacement fields for X - and Y - translations of $\sim 60 \pm 2 \mu\text{m}$ (c) mean and (d) standard deviations of u - and v -displacement fields for X - and Y - translations of $300 \pm 2 \mu\text{m}$. Magnification = $35.6 \mu\text{m}/\text{pixel}$ for $D=400$ mm and $27 \mu\text{m}/\text{pixel}$ for $D=200$ mm.

working distance ‘ D ’ on the accuracy of the measured displacements. It should be noted that magnification in Configuration-1 was $35.6 \mu\text{m}/\text{pixel}$ and in Configuration-2 it was $27 \mu\text{m}/\text{pixel}$ on the image plane. In view of this, a constant value of $\sim 60 \mu\text{m}$ (1.6 pixels) was expected for ‘solid circles’ and ‘solid squares’ of Figs. 4.12(a). Similarly a value of

~ 2.2 pixels was expected for ‘solid triangles’ and ‘solid diamonds’ of Fig. 4.12(a). It can be seen from Fig. 4.12(a), that a constant displacement is being measured in all 32 cameras within a scatter band of 0.2 pixels. Also the error levels in the displacements measured by each of the cameras fall within the range of 2 to 6% of a pixel (see Fig. 4.12(b)). Similar results for X - and Y - translations of $300 \mu\text{m}$ (between images of Sets-1 and -4 and Sets-4 and -5 of Configurations-1 and 2) are presented in Figs. 4.12(c) and (d). By comparing the results in Figs. 4.12(b) and (d), it is evident that there is no significant difference in standard deviations of the measured displacement fields. This implies that displacements of 8 to 10 pixels can be measured rather easily to an accuracy of less than 6% of a pixel. By comparing the values of ‘solid triangles’ and ‘solid circles’ in Fig. 4.12(b) or (d), it is clear that the quality of measured displacements is not affected significantly if the working distance D is reduced by a factor of 2. Finally, Fig. 4.13 shows the effect of the imposed uniform out-of-plane displacement on the measured in-plane displacements. The mean and standard deviations of u - and v -displacements that occurred between the images of Set-5 and Set-6 (Z -translation of $30 \mu\text{m}$) are shown in Figs. 4.13(a) and (b). Again, both u - and v -displacements are within 0.1 pixels in Fig. 4.13(a). The standard deviation of u - and v -displacements is in the range 1 to 6% of a pixel as evident from Fig. 4.13(b).

It is instructive to study in-plane strain fields estimated from measured displacements in these translation tests. To this end, the displacements were smoothed by the restoration method explained in Section 4.1.3 and strains were obtained by performing numerical differentiation. The mean and standard deviations of ϵ_{xx} and ϵ_{yy} strains are presented for two tests in Table 4.4. These tests correspond to X - and Y -translations of $60 \pm 2 \mu\text{m}$ (between images of Set-1 and Set-3 of configuration 1) and of $300 \pm 2 \mu\text{m}$ (between images of Set-1 and

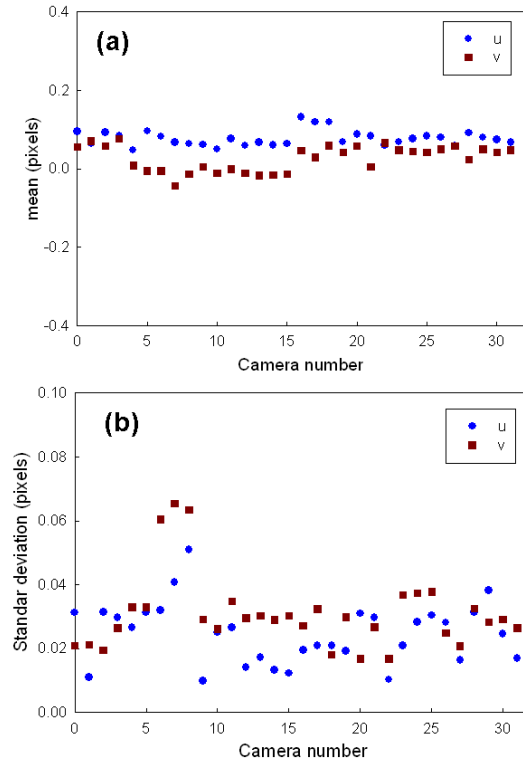


Figure 4.13: Translation test results for $D = 400$ mm (see Fig. 4.8) and out-of-plane displacement (w) = $30 \mu\text{m}$. (a) mean and (b) standard deviation of u - and v -displacement field.

Set-5 of configuration 1). Since the applied displacement was a rigid translation, ideally, zero strains for all the images are expected. However, numerical differentiation amplifies the noise in the displacements which manifests itself in the estimated strains. The mean values of strains were in the range 0 to $150 \mu\epsilon$ in both the experiments. The standard deviations of strains were in the range 0 to $300 \mu\epsilon$ for various individual cameras. Interestingly, the mean and standard deviations were not affected by the amount of translation imposed. The implication of this on an actual experiment is that a relatively large rigid body motion can be accommodated without sacrificing accuracy in the measured displacements and strains.

Camera #	$X_{trans}, Y_{trans} = 60 \pm 2\mu\text{m}$				$X_{trans}, Y_{trans} = 60 \pm 2\mu\text{m}$			
	$\epsilon_{xx} (\mu\epsilon)$		$\epsilon_{yy} (\mu\epsilon)$		$\epsilon_{xx} (\mu\epsilon)$		$\epsilon_{yy} (\mu\epsilon)$	
	Mean	Std	Mean	Std	Mean	std	Mean	Std
00	-20.7	203.1	259.7	217.1	0.9	209	2.2	229.1
01	-65	88.8	190.6	258.6	-35.3	240.6	15.4	244.6
02	-200.4	92.6	124.7	200.3	0.8	248.7	78.8	253.7
03	-210.1	139.9	30.2	209.4	13.8	341	106.4	230.6
04	-119.2	69.9	153.6	184.8	1.6	250	-9.7	241.2
05	-83.8	102.9	53.9	101.8	-52.1	167.8	10.6	335.6
06	-68.3	147	68.5	125.2	-178.7	159.5	51.6	254
07	-129.6	186	27.4	134.3	-65.5	196.4	85	277.9
08	0.4	94.6	100.3	157.4	-19.7	211.4	79.1	195.7
09	-44.1	118.4	71.8	153.8	11.2	219.7	117.1	206.1
10	-27.8	112.3	106.7	159.3	-0.7	215.2	45.4	237.1
11	-2.4	121.5	52.2	204.2	-1.5	219.5	83.5	214.2
12	-14.6	128.3	125.2	203	-42.3	201.2	-5.2	215.4
13	-7.5	140.6	36.8	284.6	-13.8	193.2	79.4	195.7
14	11.4	135.3	73.5	211.2	-50.5	235.9	3.8	202.2
15	11.5	84.6	14.9	315.3	-16.7	216.6	102.1	58.5
16	-6.5	103	168.8	308.1	-75.7	247	50.7	92.3
17	-15	113.3	3.7	319.3	-8	239.4	16.8	168.6
18	55.8	164.8	60.4	258.6	7.2	222.4	88.5	243.9
19	-7.7	126.4	192	215.1	-2.5	242.2	-33.5	242.8
20	32.4	117.1	88.8	242.2	-69.5	214.9	22.3	248.6
21	15.2	104.8	188.7	148.3	-17.3	288.1	55.5	234.6
22	28	150.3	195.5	167.1	-39.9	246.3	-34.1	247.7
23	4.5	161.9	175.8	142.5	-25.1	210.8	62.4	253.9
24	-171.4	107.7	42	217.1	15.3	224	137.2	311.6
25	-153.3	99.8	42.5	167.1	43.4	231.5	-4.9	287.1
26	-93.7	133.1	25.8	218.2	-59.5	230.3	4.1	187.9
27	-161.2	123.7	-24.1	197	-18.7	218.9	22.5	320.9
28	-133.6	92.5	162.1	126.6	10.8	237	93.1	248.6
29	-174.7	84	133.2	210.5	-16.4	203.2	-69.3	167.4
30	-93.2	149.4	-17.3	191.9	-15.5	194.5	72.2	219.8
31	-10.1	123.7	255.4	214	-3.2	200.9	53.7	221.6

Table 4.4: Mean and standard deviations of in-plane strain fields estimated from measured displacements in translation test

4.5.3 Rotation test

The objectives of the rotation test were (a) to estimate the accuracy with which a pure rotation can be measured using the high-speed camera system, (b) to compare the performance of different individual cameras when they are used to measure same applied rotation and (c) to examine whether the applied rotation produces any spurious strain. In the rotation test, a specimen decorated with random b/w speckle pattern was mounted on a rotation stage. Two sets of 32 images were recorded at 200,000 frames per second, one set before, and another set after imposing a rotation of 0.32° (0.0056 radians). The full-field displacements were computed between these two sets of images. The sub-image size chosen was 30×30 pixels so that the displacements were available on a grid of $32 \times 32 = 1024$ points. These displacements were smoothed by the restoration method explained in Section 4.1.3. The cross derivative terms $\partial u/\partial y$ and $\partial v/\partial x$ were computed by numerical differentiation. The rotation ω_{xy} was then evaluated as,

$$\omega_{xy} = \frac{1}{2} \left(\frac{\partial u}{\partial y} - \frac{\partial v}{\partial x} \right). \quad (4.11)$$

Figure 4.14 shows a representative full-field plot of ω_{xy} from one pair of the images. The estimated values are close to the applied value of rotation everywhere in the image except near the boundaries. This is expected because the errors displacement derivatives (strains and rotations) get magnified near the boundaries due to the so-called edge effects. Next, mean and standard deviations of ω_{xy} were computed for each image (while computing these quantities for a 32×32 matrix, three rows and three columns of data points were excluded near the border of the image in view of the presence of larger errors at these

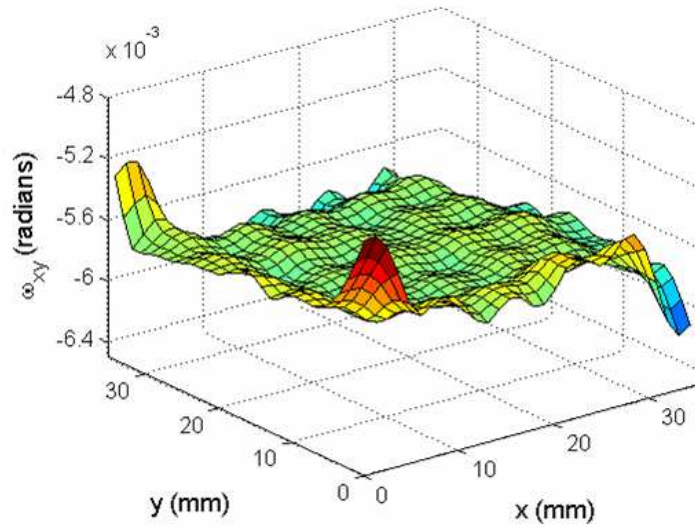


Figure 4.14: Estimated full-field quantity ω_{xy} from one pair of the images taken from camera # 1 in a rotation experiment (Imposed rotation = 0.0056 ± 0.00035 radians).

locations). Figure 4.15 shows the mean and standard deviation of estimated rotations and strains from this test. It can be seen from Fig. 4.15(a) and (c) that an applied rotation of 0.0056 ± 0.00035 radians is measured by all the individual cameras with in an error band of $\sim 5 \times 10^{-4}$ radians (10 % error). A rigid rotation imposed to the sample will not produce any strains. Consequently, zero strains are expected from this test. However, the mean values of strain fields obtained were within $100 \mu\epsilon$ and standard deviations were up to $300 \mu\epsilon$. Thus, it can be said that in an actual experiment involving some rigid rotation of the sample, spurious values of in-plane strains in the range to 100 to $300 \mu\epsilon$ can be expected.

4.6 Flash lamp light characteristics

One of the main assumptions while performing image correlation between two images recorded by a high-speed digital camera system is that illumination of the specimen is

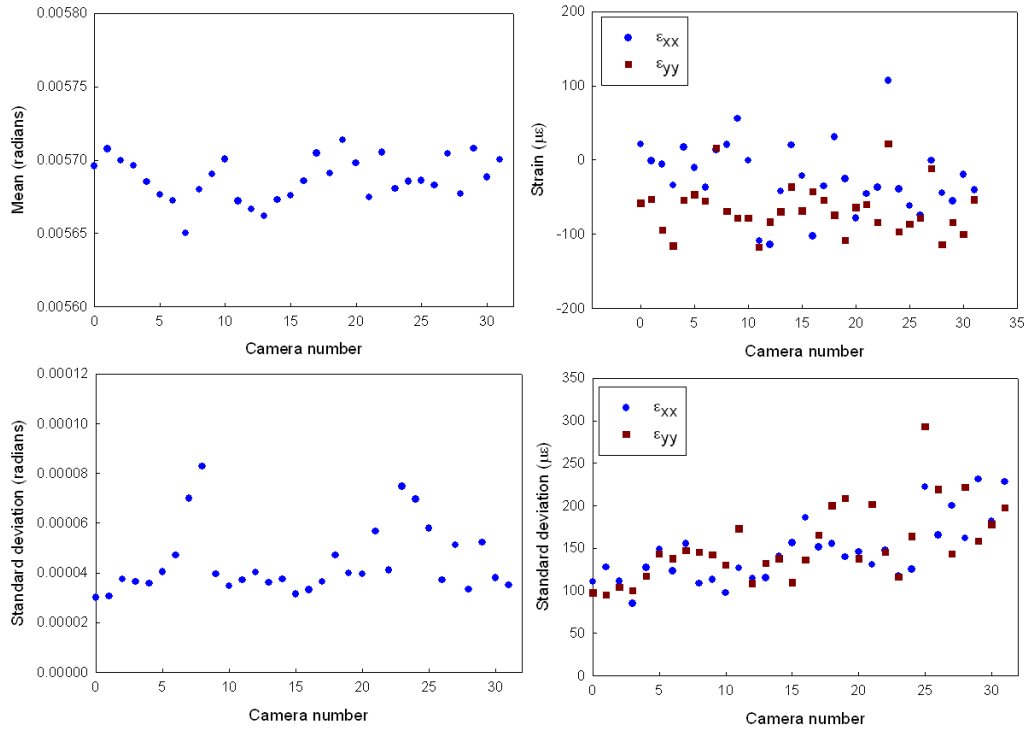


Figure 4.15: Results from rotation test (applied rotation = 0.0056 ± 0.00035 radians). (a) mean and (c) standard deviation of rotation field estimated from image correlation. (b) mean (d) standard deviations of in-plane strains estimated (ideally these strains need to be zeros).

uniform and stable (spatially as well as temporally) and also repeatable. Spatial stability means the light intensity needs to be uniform in the region of interest (in the current work $31 \times 31 \text{ mm}^2$ area). By temporal stability, we expect the light intensity to remain constant during the event of interest ($\sim 150 \mu s$ in this work during which all the 32 images were acquired). The repeatability is also important since the light intensity need to remain same between any two successive experiments. To be more specific, undeformed set of 32 images and the deformed set of 32 images need to be exposed by the same light intensity.

The light intensity from the flash lamps ramps up initially, dwells for a while and then decreases. In the current work, dwell time was set to 9 ms. In order to test flash lamp characteristics, a photo detector having 1 mm^2 sensing area was placed at a location where the sample was placed in the real experiment. The voltage signal proportional to the light intensity was recorded with time using a high-speed data acquisition system at a sampling rate of 1 MHz. This exercise was repeated twice in order to check for the repeatability of the flash lamp characteristics. Subsequently, the photo detector was moved to a new location in the plane perpendicular to the optical axis of the camera by 25 mm inch and the output was again recorded twice. The voltage signal registered by the photo detector is plotted in Fig. 4(b). An excellent repeatability in the light intensity can be seen. A dwell time of 9

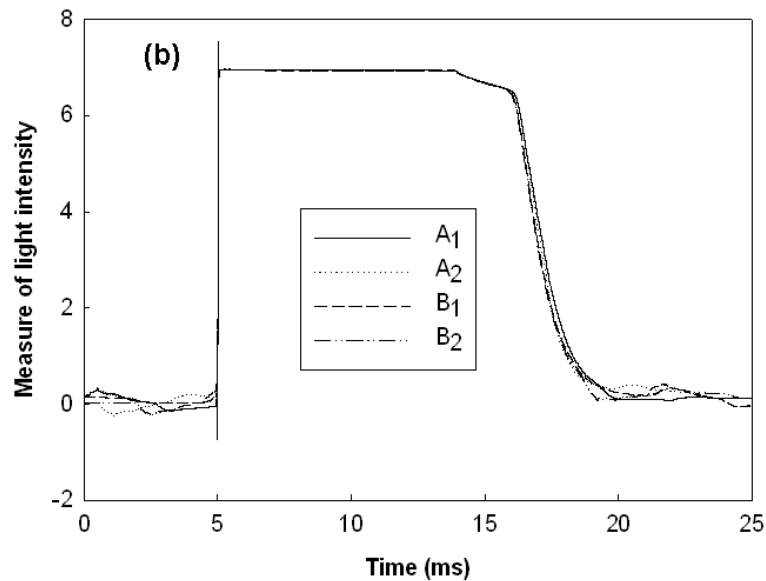


Figure 4.16: Photo detector output proportional to flash lamp light intensity, A_1 , A_2 and B_1 , B_2 are two repeated acquisitions when photodiode was placed one inch away in the plane perpendicular to optical axis of the camera.

ms can be seen from all these plots. While conducting the real experiment, all the images

were captured during this dwell time by appropriately triggering the event. Thus, the flash lamps were found to be stable and no hot spots were found in the captured images.

CHAPTER 5

DYNAMIC FRACTURE STUDIES USING DIC METHOD

In this chapter, the method of DIC to study dynamic fracture in polymeric materials is discussed. Mode-I and mixed-mode dynamic fracture of epoxy and syntactic foam samples are examined using this method. The sample preparation and the experimental procedure are explained in detail. The crack opening and sliding displacements and dominant strain histories are computed from speckle images. The dynamic stress intensity factor histories are extracted by performing over-deterministic least-squares analysis on estimated displacements.

5.1 Sample preparation

Edge cracked epoxy and syntactic foam samples were prepared for conducting mode-I and mixed-mode dynamic fracture experiments, respectively, using DIC method. Epoxy samples were made from bisphenol-A resin and an amine based hardener in the ratio 100:38 for mode-I experiments. For mixed-mode tests, samples were made by mixing 25% (by volume) of hollow microballoons in the epoxy matrix. The microballoons used in this study were commercially available hollow glass spheres of mean diameter of $\sim 60 \mu\text{m}$ and wall thickness $\sim 600 \text{ nm}$. The microballoons were carefully stirred into the epoxy resin while avoiding air bubbles and agglomeration. Stirring was continued until the mixture showed a tendency to gel and then poured into molds. This helped to eliminate any buoyancy induced floatation of microballoons during the cure cycle. The elastic modulus and Poisson's ratio, measured ultrasonically, were 4.1 GPa and 0.34 for epoxy samples and 3.02 GPa and 0.34

for syntactic foam samples, respectively [24]. While casting the mixture, a sharp razor blade was inserted into the mold. After the sample was cured, a sharp ‘edge notch’ was left behind in the specimen. Further details about this method of introducing a sharp crack into specimens can be found in Ref. [77]. Finally, the specimen was machined into beams of height 50 mm with a crack of 10 mm length ($a/W = 0.2$) as shown in Fig. 5.1(a) and (b). A random speckle pattern was created on the specimen surface by spray-painting with black and white paints alternatively.

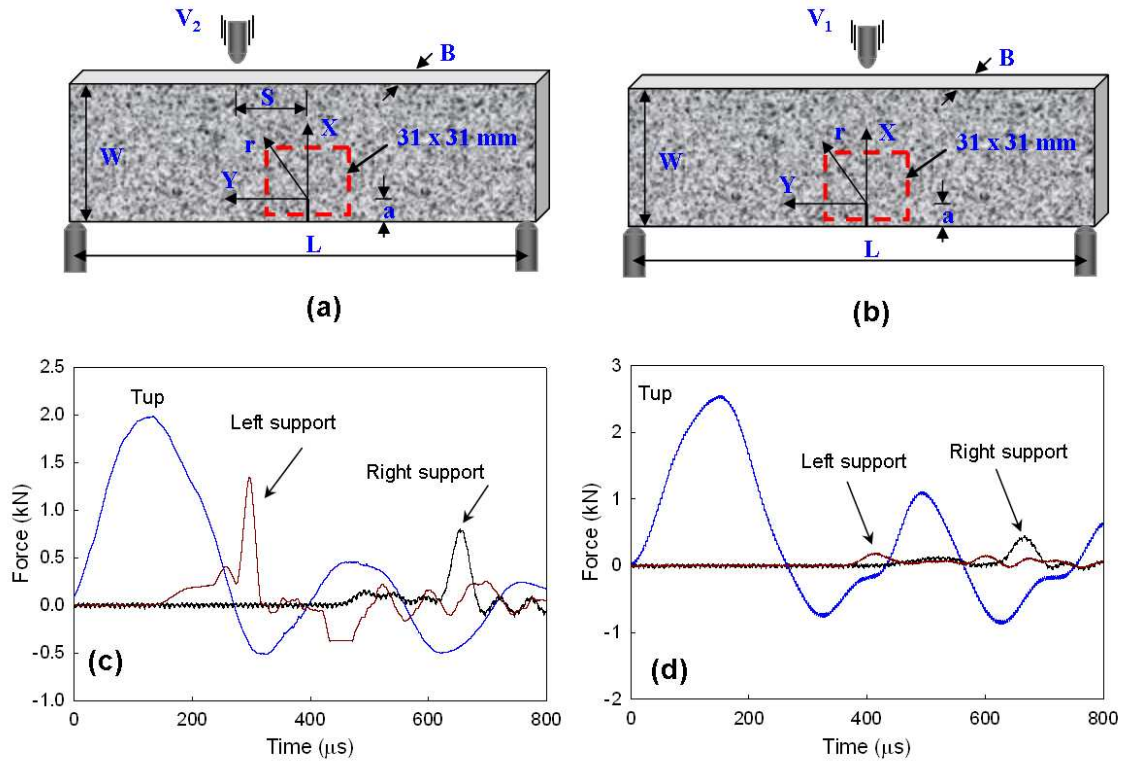


Figure 5.1: Specimen configuration for (a) mixed-mode test of syntactic foam and (b) mode-I test of epoxy. Impactor force history and support reaction histories recorded by Instron Dynatup 9250 HV drop tower for (c) mixed-mode experiment and (d) mode-I experiment. The sample dimensions are $a = 10$ mm, $W = 50$ mm, $S = 25.4$ mm, $L = 200$ mm, $B = 8.75$ mm, Impact velocities, $V_1 = 4.5$ m/sec and $V_2 = 4.0$ m/sec.

5.2 Experimental procedure

Since the event to be captured is highly transient in nature, the total recording time is rather small and hence the high-speed camera was synchronized with the event. The sequence of events in a typical experiment was as follows: The specimen was initially rested on two instrumented supports/anvils of the drop tower. The camera, anchored firmly to the ground, was focused on $31 \times 31 \text{ mm}^2$ region of the sample in the crack tip vicinity (see Fig. 5.1 (a) and (b)). A set of 32 pictures of the stationary sample were recorded at the desired framing rate (225,000 frames per second in mode-I and 200,000 frames per second in mixed-mode experiment). Next, an impactor was launched at a desired velocity ($\sim 4.5 \text{ m/sec}$ for mode-I $\sim 4.0 \text{ m/sec}$ for mixed-mode) towards the sample. As soon as the tup contacted an adhesive backed copper tape affixed to the top of the specimen, a signal was generated by a pulse/delay generator to trigger the camera. The camera also sent a separate trigger signal to the high intensity flash lamps. A trigger delay was pre-set in the camera system to capture images $\sim 75 \mu\text{s}$ after the initial impact. This time delay provides sufficient time for the high intensity flash lamps to ramp up to their full intensity level and provide uniform illumination during recording. Since the measurable deformations around the crack tip for the first $85 \mu\text{s}$ are relatively small, there was no significant loss of information during this period. A total of 32 images were recorded with $4.44 \mu\text{s}$ ($5 \mu\text{s}$ in mixed-mode tests) interval between images for a total duration of $142 \mu\text{s}$ ($160 \mu\text{s}$ in mixed-mode tests). Once the experiment was complete, the captured images were stored in the computer. Just before the impact occurs, the velocity of the tup was recorded by the drop-tower system. Also recorded were the tup force and support reaction histories.

The tup force and support reaction histories are shown in Fig. 5.1(c) and (d) for asymmetric impact of syntactic foam specimen and symmetric impact of epoxy specimen, respectively. In these plots, multiple contacts between the specimen and the tup can be evidenced by the occurrence of more than one peaks. Since complete fracture of the specimen had taken place before $240 \mu\text{s}$ in both the experiments, only the first peak of the impact force history is of relevance here. From Fig. 5.1(d) it can be seen that supports feel the impact force only after $\sim 400 \mu\text{s}$ for the mode-I test. In case of the mixed-mode test, since left support is closer to the impact point, the impact force records start earlier than the one for the right support (see Fig. 5.1(c)). Also, it should be noted that anvils register a noticeable impact force after $220 \mu\text{s}$ by which time the crack had propagated through half the sample width (see Fig. 5.4). Thus, the reactions from the anvils do not play any role in the crack initiation and initial growth. Accordingly, for both the tests, the samples were subsequently modeled as a free-free beam in finite element simulations with impact resisted by the specimen inertia.

5.3 Finite element simulations

5.3.1 Mixed-mode fracture of syntactic foam

Elasto-dynamic finite element simulations were conducted up to crack initiation under plane stress conditions. The finite element mesh used is shown in Fig. 5.2(a) along with the force boundary conditions at the impact point. Experimentally determined material properties (elastic modulus = 3.1 GPa, Poisson's ratio 0.34 and mass density = 870 kg/m^3) were used as inputs for the finite element analysis. The numerical model was loaded using the force history recorded by the instrumented tup (only the first peak of the tup force

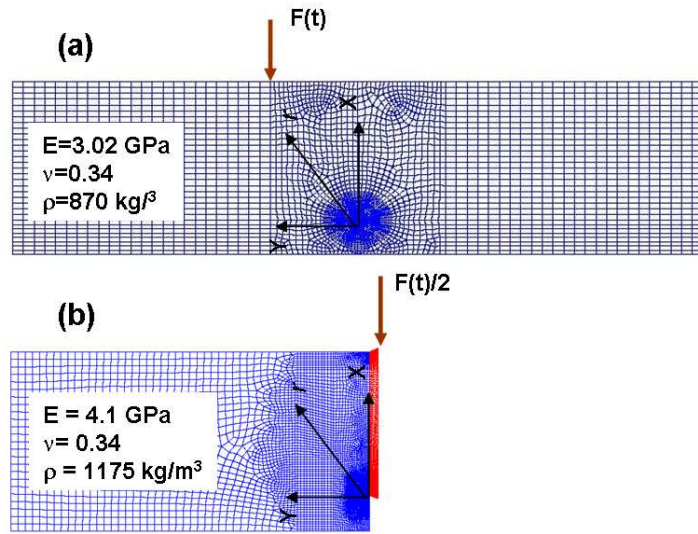


Figure 5.2: Finite element mesh used for elasto-dynamic finite element analysis of **(a)** mixed-mode problem and **(b)** mode-I problem.

from Fig. 5.1(c) was used). (Before applying, the force history data was interpolated and smoothed for the following two reasons: (a) The time step of the force history measurement was larger than the one used in the simulations and (b) The force history recorded by the tup had experimental noise. Therefore smoothed cubic splines were fitted to the force history data before applying to the model.) The implicit time integration scheme of the Newmark β method with parameters $\beta = 0.25$ and $\gamma = 0.5$ and 0.5% damping was adopted in the simulations.

Instantaneous crack opening and sliding displacements along the crack flanks were used for extracting mode-I and mode-II stress intensity factors (SIF). Using Williams' asymptotic expansion for crack opening and sliding displacements, apparent stress intensity factors can

be expressed as

$$\begin{aligned} [K_I(t)]_{app} &= \frac{\sqrt{2\pi} E u_y(t)|_{\theta=\pm\pi}}{8\sqrt{r}} \approx K_I(t) + C_1 r, \\ [K_{II}(t)]_{app} &= \frac{\sqrt{2\pi} E u_x(t)|_{\theta=\pm\pi}}{8\sqrt{r}} \approx K_{II}(t) + C_2 r. \end{aligned} \quad (5.1)$$

Here u_y and u_x are the crack opening and sliding displacements, respectively, K_I and K_{II} are mode-I and mode-II stress intensity factors, E is the elastic modulus of the material, C_1 and C_2 are higher order coefficients. For each time instant, the values of $[K_I(t)]_{app}$ and $[K_{II}(t)]_{app}$ are plotted as a function of r and the extrapolated values $K_I = \lim_{r \rightarrow 0} [K_I]_{app}$ and $K_{II} = \lim_{r \rightarrow 0} [K_{II}]_{app}$ were identified as the mode-I and mode-II instantaneous stress intensity factors.

5.3.2 Mode-I fracture of epoxy

The finite element simulation procedures for the mode-I test are same as the mixed-mode test except the numerical model was loaded using one-half of the force history recorded by the instrumented tup due to symmetry of the model. Finite element mesh of the half-model used is shown in Fig. 5.2(b) along with the boundary conditions. Experimentally determined material properties for this case are (elastic modulus = 4.1 GPa, Poisson's ratio 0.34 and mass density = 1175 kg/m³). As explained in the previous section, the mode-I SIF was calculated by regression of crack opening displacements by the formula

$$[K_I(t)]_{app} = \frac{\sqrt{2\pi} E u_y(t)|_{\theta=\pm\pi}}{4\sqrt{r}} \approx K_I(t) + Cr. \quad (5.2)$$

The T -stress was also determined using a modified stress difference method [77]. Instantaneous normal stress difference $(\sigma_x - \sigma_y)$ ahead of the crack tip along X_1 -axis was used to calculate the non-singular T -stress as

$$(\sigma_x - \sigma_y)|_{r,\theta=0^\circ} \approx T + Dr, \quad (5.3)$$

where D is a higher order coefficient of the asymptotic expansion of crack tip stresses.

5.4 Results - Mixed-mode dynamic fracture of syntactic foam

From each experiment 64 images were available, 32 each from the undeformed and the deformed sets, each having a resolution of 1000×1000 pixels. Figure 5.3 shows four selected speckle pattern images from the deformed set of 32 images. The time instant at which the images were recorded after impact is shown below each image and the current crack tip location is indicated by an arrow. The position of the crack tip is plotted against time in Fig. 5.4. It can be seen from this figure that crack initiates at about $175 \mu\text{s}$. Upon initiation, the crack rapidly accelerates and subsequently attains at a relatively steady velocity of ~ 270 m/s. The magnification used in this experiment was such that the size of a pixel was equal to $31 \mu\text{m}$ on the specimen. A sub-image size of 26×26 pixels was chosen for image correlation. The 2D in-plane displacements were estimated for all the 32 image-pairs. The crack opening displacement, u_y , and sliding displacement, u_x , for the sample images (one before crack initiation and one after) are shown in Fig. 5.5.

Figures 5.5(a) and (c) show u_y - and u_x -displacements at $150 \mu\text{s}$ after impact and Figs.5.5(b) and (d) show the corresponding displacement components at $t = 220 \mu\text{s}$ after impact. These are smoothed values of displacements (aspects of smoothing were discussed

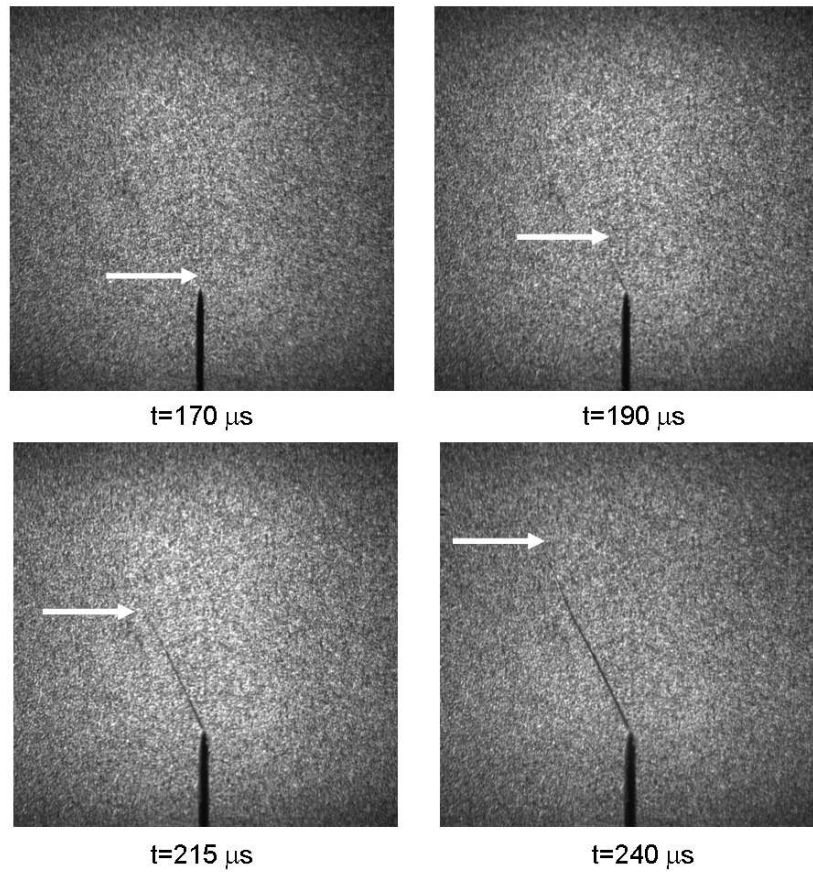


Figure 5.3: Acquired speckle images of $31 \times 31 \text{ mm}^2$ region at various times instants. (Crack tip location is shown by an arrow.)

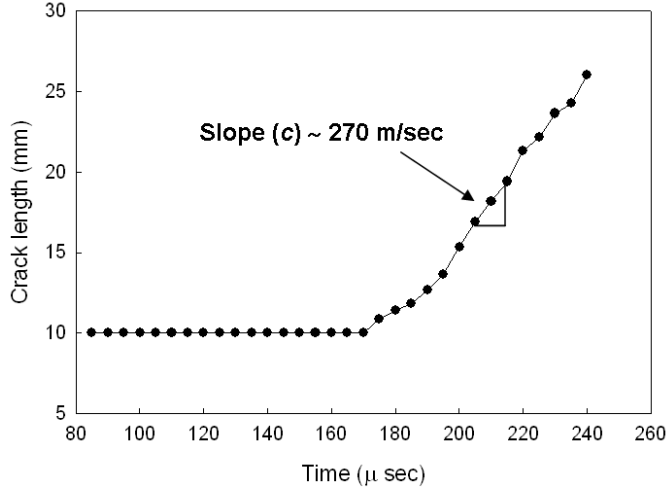


Figure 5.4: Crack growth behavior in syntactic foam sample under mixed-mode dynamic loading.

in Chapter 4). A significant amount of rigid body displacement component can be seen in the u_x -field (Figs. 5.5(c) and (d)). In the current work, the displacements were resolved to an accuracy of 2 to 6% of a pixel or 0.6 to 1.8 μm .

5.4.1 Extraction of stress intensity factors

Both crack opening and sliding displacement fields were used to extract dynamic stress intensity factors in the current work. The asymptotic expressions for crack tip displacement fields for a dynamically loaded stationary crack are given by [72],

$$\begin{aligned}
 u_x = & \sum_{n=1}^N \frac{(K_I)_n}{2\mu} \frac{r^{n/2}}{\sqrt{2\pi}} \left\{ \kappa \cos \frac{n}{2}\theta - \frac{n}{2} \cos \left(\frac{n}{2} - 2 \right)\theta + \left\{ \frac{n}{2} + (-1)^n \right\} \cos \frac{n}{2}\theta \right\} \\
 & + \sum_{n=1}^N \frac{(K_{II})_n}{2\mu} \frac{r^{n/2}}{\sqrt{2\pi}} \left\{ \kappa \sin \frac{n}{2}\theta - \frac{n}{2} \sin \left(\frac{n}{2} - 2 \right)\theta + \left\{ \frac{n}{2} - (-1)^n \right\} \sin \frac{n}{2}\theta \right\}, \quad (5.4)
 \end{aligned}$$

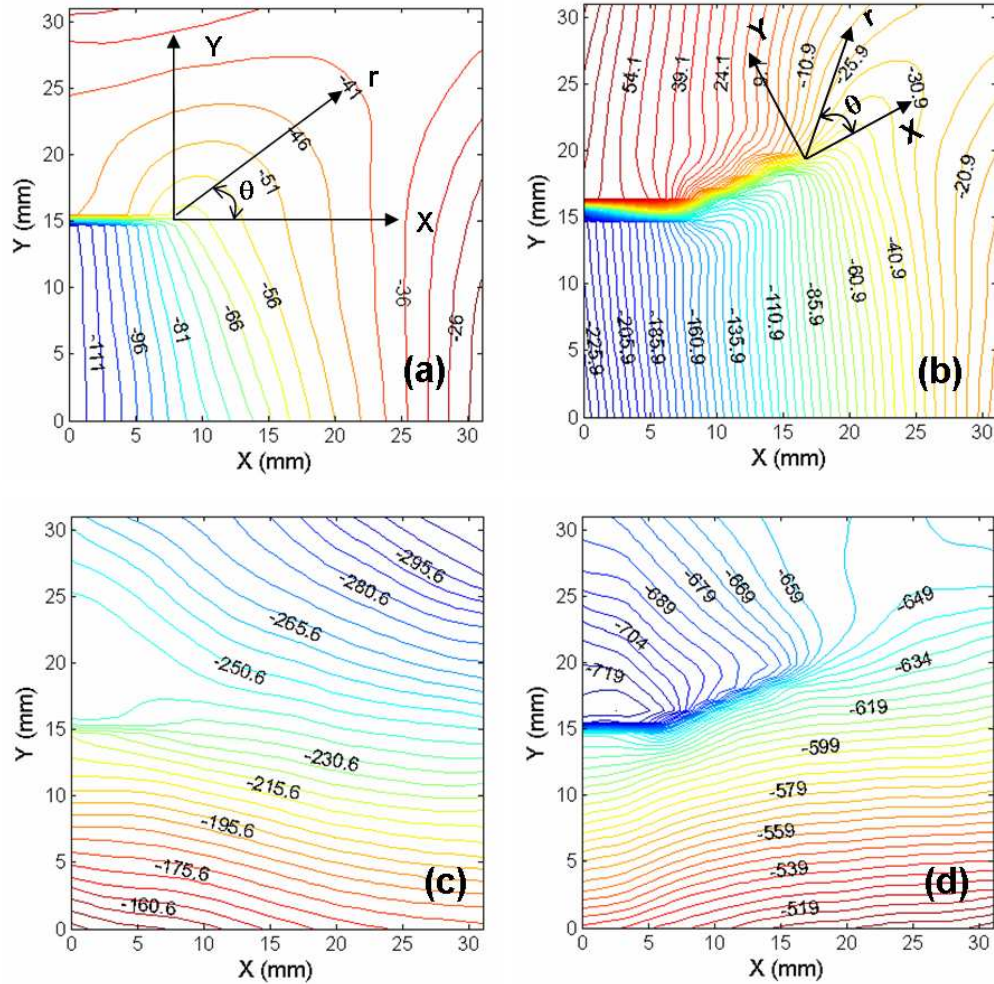


Figure 5.5: Crack opening and sliding displacements (in mm) for pre- and post-crack initiation instants. **(a)** v -displacement and **(c)** u -displacement before crack initiation (at $t=150 \mu\text{s}$); **(b)** v -displacement and **(d)** u -displacement after crack initiation ($t=220 \mu\text{s}$). Crack initiation time $\sim 175 \mu\text{s}$. (A large rigid body displacement can be seen in (c) and (d) due to movement of the sample).

$$\begin{aligned}
u_y = & \sum_{n=1}^N \frac{(K_I)_n r^{n/2}}{2\mu \sqrt{2\pi}} \left\{ \kappa \sin \frac{n}{2} \theta + \frac{n}{2} \sin \left(\frac{n}{2} - 2 \right) \theta - \left\{ \frac{n}{2} + (-1)^n \right\} \sin \frac{n}{2} \theta \right\} \\
& + \sum_{n=1}^N \frac{(K_{II})_n r^{n/2}}{2\mu \sqrt{2\pi}} \left\{ -\kappa \cos \frac{n}{2} \theta - \frac{n}{2} \cos \left(\frac{n}{2} - 2 \right) \theta + \left\{ \frac{n}{2} - (-1)^n \right\} \cos \frac{n}{2} \theta \right\}. \quad (5.5)
\end{aligned}$$

In the above equations, u_x and u_y are crack sliding and opening displacements, (r, θ) are crack tip polar coordinates, κ is $(3 - \nu)/(1 + \nu)$ for plane stress where μ and ν are shear modulus and Poisson's ratio, respectively. The coefficients $(K_I)_n$ and $(K_{II})_n$ of the leading terms ($n = 1$) are the mode-I and mode-II dynamic stress intensity factors (SIF), respectively. Equations (5.4-5.5) implicitly assume that inertial effects enter the coefficients while retaining the functional form of the quasi-static crack tip equation. However, once the crack initiates, asymptotic expressions for crack sliding and opening displacement fields for a steadily propagating crack are used [85]:

$$\begin{aligned}
u_x = & \sum_{n=1}^N \frac{(K_I)_n B_I(C)}{2\mu} \sqrt{\frac{2}{\pi}} (n+1) \left\{ r_1^{n/2} \cos \frac{n}{2} \theta_1 - h(n) r_2^{n/2} \cos \frac{n}{2} \theta_2 \right\} \\
& + \sum_{n=1}^N \frac{(K_{II})_n B_{II}(C)}{2\mu} \sqrt{\frac{2}{\pi}} (n+1) \left\{ r_1^{n/2} \sin \frac{n}{2} \theta_1 + h(\bar{n}) r_2^{n/2} \sin \frac{n}{2} \theta_2 \right\}, \quad (5.6)
\end{aligned}$$

$$\begin{aligned}
u_y = & \sum_{n=1}^N \frac{(K_I)_n B_I(C)}{2\mu} \sqrt{\frac{2}{\pi}} (n+1) \left\{ -\beta_1 r_1^{n/2} \sin \frac{n}{2} \theta_1 + \frac{h(n)}{\beta_2} r_2^{n/2} \sin \frac{n}{2} \theta_2 \right\} \\
& + \sum_{n=1}^N \frac{(K_{II})_n B_{II}(C)}{2\mu} \sqrt{\frac{2}{\pi}} (n+1) \left\{ \beta_1 r_1^{n/2} \cos \frac{n}{2} \theta_1 + \frac{h(\bar{n})}{\beta_2} r_2^{n/2} \cos \frac{n}{2} \theta_2 \right\}, \quad (5.7)
\end{aligned}$$

where

$$r_m = \sqrt{X^2 + \beta_m^2 Y^2}, \quad \theta_m = \tan^{-1} \left(\frac{\beta_m Y}{X} \right) \quad m = 1, 2$$

$$\begin{aligned}
\beta_1 &= \sqrt{1 - \left(\frac{c}{C_L}\right)^2}, & \beta_2 &= \sqrt{1 - \left(\frac{c}{C_S}\right)^2} \\
C_L &= \sqrt{\frac{(\kappa+1)\mu}{(\kappa-1)\rho}}, & C_S &= \sqrt{\frac{\mu}{\rho}}, & \kappa &= \frac{3-\nu}{1+\nu} \quad \text{for plane stress} \\
h(n) &= \begin{cases} \frac{2\beta_1\beta_2}{1+\beta_2^2} & \text{for odd } n \\ \frac{1+\beta_2^2}{2} & \text{for even } n \end{cases} & & h(\bar{n}) = h(n+1) \\
B_I(C) &= \frac{1+\beta_2^2}{D}, & B_{II}(C) &= \frac{2\beta_2}{D}, & D &= 4\beta_1\beta_2 - (1+\beta_2^2)^2.
\end{aligned} \tag{5.8}$$

Here (X, Y) and (r, θ) are crack tip Cartesian and polar coordinates instantaneously aligned with the current crack tip (see, Fig. 5.5(b)) and c is the speed of the propagating crack tip, C_L and C_S are dilatational and shear wave speeds in the material, μ and ν are shear modulus and Poisson's ratio, respectively. Again, coefficients $(K_I)_n$ and $(K_{II})_n$ of the leading terms are the mode-I and mode-II dynamic stress intensity factors, respectively.

For a mode-I problem u_y is the dominant in-plane displacement and hence used for extracting mode-I SIF history. However, in a mixed-mode problem, both u_x and u_y displacements can be equally important. It can be thought that crack opening displacement u_y as having mode-I rich information whereas sliding displacement u_x as having mode-II rich information. Therefore, one can use u_y to extract K_I and u_x to extract K_{II} accurately. On the other hand, one can use either radial (u_r) or tangential (u_θ) displacements (computed by transforming u_x and u_y) to extract both K_I and K_{II} together more accurately compared to using u_x and u_y alone. Following Yoneyama *et al.*[86] who have demonstrated this recently, in the current work the radial displacement component u_r was used to extract both K_I and K_{II} histories.

For extracting SIF from displacement data, the current crack tip location was identified and the Cartesian and polar coordinate systems ($X - Y$ and $r - \theta$) were established at the crack tip. A number of data points (usually 100 to 120) were collected in the region around the crack tip ($0.3 < r/B < 1.6$) and ($-145^\circ < \theta < 145^\circ$) where B is the sample thickness and u_x and u_y displacement values as well the location of these points were stored. Next u_x and u_y were transformed into u_r and u_θ as,

$$\begin{pmatrix} u_r \\ u_\theta \end{pmatrix} = \begin{pmatrix} \cos \theta & \sin \theta \\ -\sin \theta & \cos \theta \end{pmatrix} \begin{pmatrix} u_x \\ u_y \end{pmatrix}. \quad (5.9)$$

The asymptotic expression for u_r also transformed from u_x and u_y as follows:

$$\begin{aligned} u_{rk} = & \left\{ \sum_{n=1}^N (K_I)_n f_{In}(r_k, \theta_k) + \sum_{n=1}^N (K_{II})_n f_{II n}(r_k, \theta_k) \right\} \cos \theta_k \\ & + \left\{ \sum_{n=1}^N (K_I)_n g_{In}(r_k, \theta_k) + \sum_{n=1}^N (K_{II})_n g_{II n}(r_k, \theta_k) \right\} \sin \theta_k \\ & + T_x \cos \theta_k + T_y \sin \theta_k, \end{aligned} \quad (5.10)$$

where f_{In} , $f_{II n}$, g_{In} and $g_{II n}$ are angular functions from Eqs. 5.4 and 5.5 or 5.6 and 5.7. In Eq. 5.10 the subscripts ' n ' and ' k ' are indices used to represent the number of terms in the expansion (usually 4 to 5 were found sufficient in this work) and the number of data points where the displacements were collected. Further, T_x and T_y denote rigid body translations in the X - and Y -directions, respectively. An over-deterministic least-squares analysis [87] of the data was carried out for finding K_I and K_{II} . This was repeated for all the 32 image pairs and the stress intensity factor histories were generated.

Figure 5.6 shows SIF histories extracted from displacements. The crack initiation time

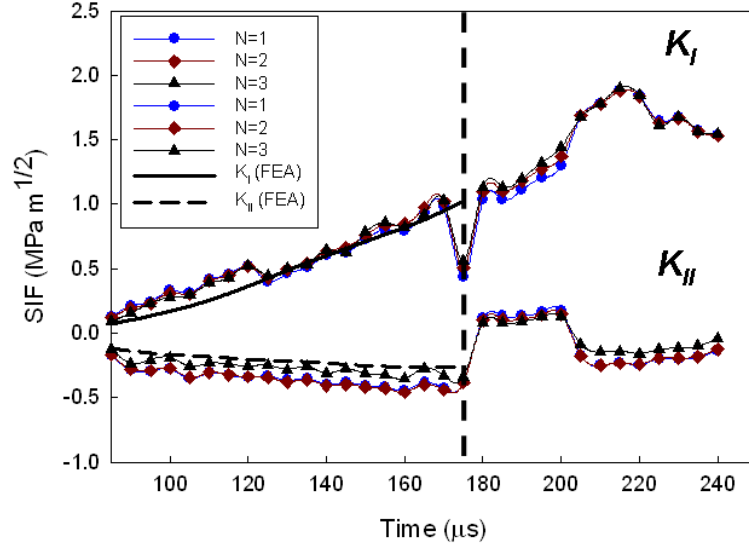


Figure 5.6: Stress intensity factors extracted from displacement fields obtained from image correlation. SIF history obtained from finite element simulation up to crack initiation is also shown.

is indicated by a vertical dotted line. Three different plots are presented for both K_I and K_{II} by varying the number of terms in the asymptotic series. A good convergence can be seen from Fig. 5.6 when the number of terms ($N = 1, 2, 3$) was used in the expansion. Both mode-I and mode-II SIFs increase monotonically up to crack initiation at $175 \mu\text{s}$. At crack initiation there is a noticeable drop in the magnitudes of both K_I and K_{II} due to elastic unloading near the crack tip. Following initiation at $\sim 1.0 \text{ MPa m}^{1/2}$, K_I continues to increase until it reaches a value of $\sim 1.8 \text{ MPa m}^{1/2}$ beyond which it shows a decreasing trend whereas the mode-II SIF, K_{II} , remains close to zero after initiation. The SIF histories evaluated from experiments are in good agreement with the ones from finite element computations up to crack initiation. The relative amount of in-plane shear stress to normal stress near the crack can be quantified by mode mixity $\psi = \tan^{-1}(K_{II}/K_I)$. The mode mixity history is plotted in Fig. 5.7. A large negative value for ψ can be seen at initial

stages after impact indicating the presence of significant negative in-plane shear component at the crack tip. Just before crack initiation, however, ψ approaches zero suggesting that crack initiation occurs under dominant mode-I conditions.

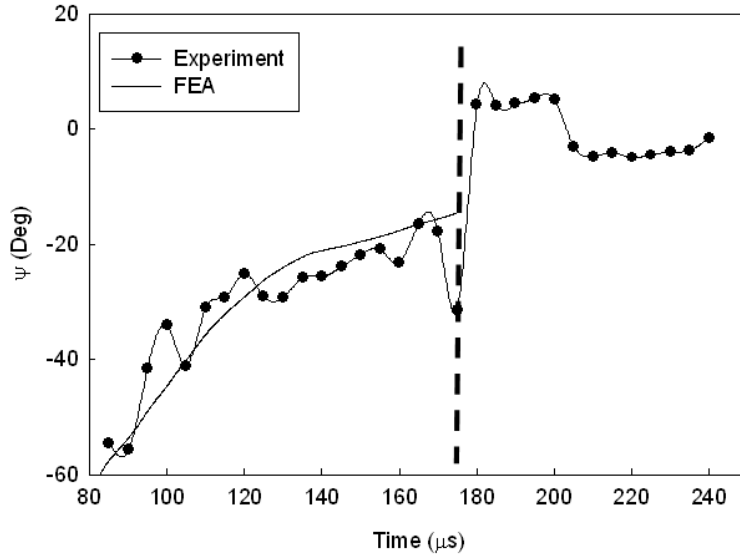


Figure 5.7: The mode-mixity, ψ obtained from experiments and finite element simulation. The broken line corresponds to crack initiation time.

5.4.2 Estimation of strains

Displacements were smoothed by the methodology explained in Section 4.1.3. In order to smooth the displacement fields, the noise level in the displacement data needs to be quantified. The following approach was adopted to estimate the same. A random speckle pattern was imaged twice with the high-speed camera system at the same framing rate as the used in an actual experiment without deforming the specimen. The full-field u - and v -displacements were estimated between these two images. Figure A.1 (in Appendix A) shows u -displacement extracted from such an experiment. Ideally one would expect both u - and

u - displacements to be zero in the entire field. The displacements, however, oscillates about zero with some experimental noise. The displacement shown in Fig. A.1 has a standard deviation of $\sigma = 0.039$ pixels and a variance of 0.0019. This value was accepted as the noise and was used in Eq. 4.9 to estimate the optimum value of the smoothing parameter α_s . Once displacements were smoothed, Lagrangian strains,

$$\epsilon_{xx} = \frac{\partial u}{\partial x} + \frac{1}{2} \left\{ \left(\frac{\partial u}{\partial x} \right)^2 + \left(\frac{\partial v}{\partial x} \right)^2 \right\} \quad (5.11)$$

$$\epsilon_{yy} = \frac{\partial v}{\partial y} + \frac{1}{2} \left\{ \left(\frac{\partial u}{\partial y} \right)^2 + \left(\frac{\partial v}{\partial y} \right)^2 \right\} \quad (5.12)$$

$$\epsilon_{xy} = \frac{1}{2} \left\{ \frac{\partial u}{\partial y} + \frac{\partial v}{\partial x} \right\} + \frac{1}{2} \left\{ \frac{\partial u}{\partial x} \frac{\partial u}{\partial y} + \frac{\partial v}{\partial x} \frac{\partial v}{\partial y} \right\}, \quad (5.13)$$

were obtained by differentiating displacements. (The use of higher order terms did not affect the results significantly in this work.) The crack tip normal strains obtained using this methodology are shown in Fig. 5.8(a) at time $t = 150 \mu\text{s}$ after impact. Normal strain contours from finite element results at $t = 150 \mu\text{s}$ is also shown in Fig. 5.8(b). To facilitate direct comparison, an increment of roughly $132 \mu\epsilon$ was chosen between each contour level in both these plots. Since the accuracy of measured strains range between 150 to $300 \mu\epsilon$, lower strain levels are relatively inaccurate. Typical mixed-mode normal strain contours, concentrated around the crack tip can be seen in these figures. A severe concentration of strain contours around the crack tip is seen in Fig. 5.8(a). Further, a qualitative similarity between the strain contours obtained from the experiments and finite element simulations exist in Figs. 5.8(a) and (b).

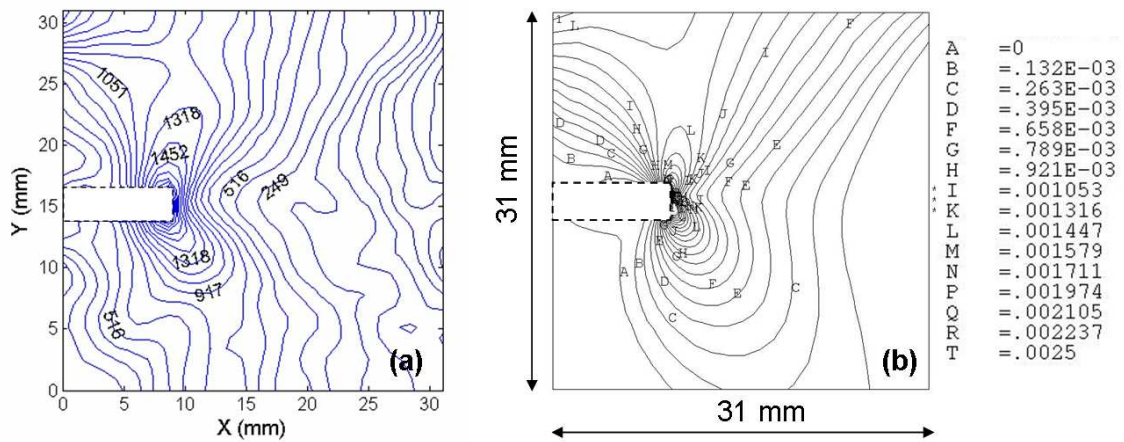


Figure 5.8: Crack tip normal strains (in micro strains) at $t = 150 \mu\text{s}$. (a) from experiment and (b) From FEA. Crack initiation time = $175 \mu\text{s}$.

5.5 Results - Mode-I dynamic fracture of epoxy

Figure 5.9 shows four selected speckle pattern images from the deformed set of 32 images. The time instant at which the images were recorded after impact is indicated below each image and the current crack tip is denoted by an arrow. The position of the crack tip is plotted against time in Fig. 5.10. It can be seen from this figure that the crack initiates at about $133 \mu\text{s}$. Also plotted is the crack speed history obtained by numerically differentiating crack length history using a central difference scheme. It can be noted from this figure that upon initiation, crack rapidly accelerates to $\sim 350 \text{ m/s}$ and subsequently propagates at a relatively steady velocity of 250 m/s . The magnification used in this experiment was such that the size of a pixel was $31 \mu\text{m}$ on the specimen. A sub-image size of 30×30 pixels was chosen for image correlation. The 2D in-plane displacements were estimated for all the 32 image-pairs. The crack opening displacement, v , and sliding displacement, u , for two sample images (one before crack initiation and one after) are shown in Fig. 5.11. Figures

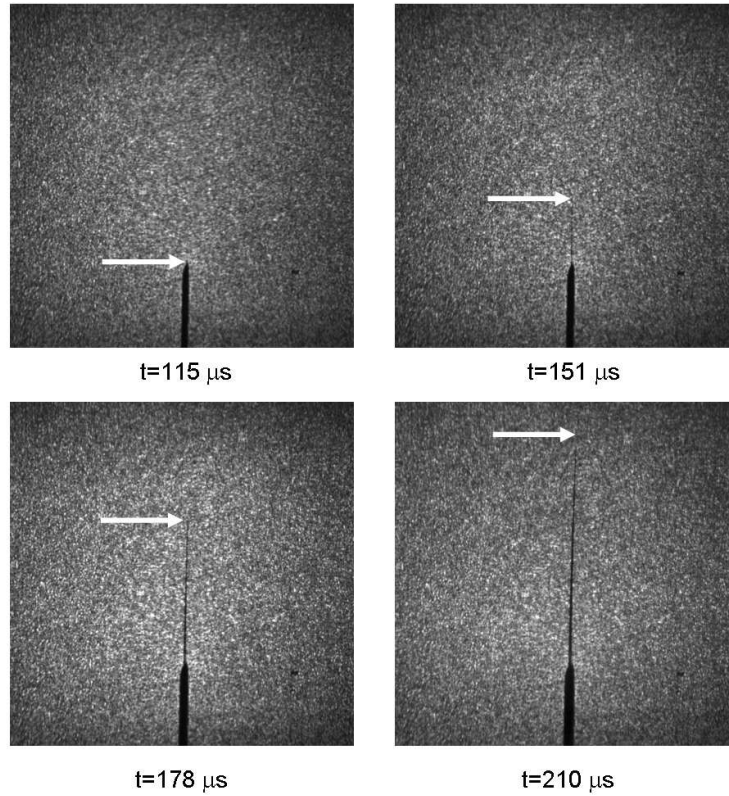


Figure 5.9: Acquired speckle images of $31 \times 31 \text{ mm}^2$ region at various times instances. Current crack tip location is shown by an arrow.

5.11(a) and (c) show v - and u -displacements at $120 \mu\text{s}$ after impact and Figs. 5.11(b) and (d) show the corresponding displacement components at $t = 151 \mu\text{s}$ after impact. These are smoothed values of displacements (aspects of smoothing were discussed in section 4.1.3). A dominant mode-I crack opening displacement field can be noticed from Figs. 5.11(a) and (b). A significant amount of rigid body displacement component can be seen from the u -field (Figs. 5.11(c) and (d)). In the current work, the displacements were resolved to an accuracy of 2 to 6% of a pixel. Therefore the accuracy of the displacement components in

Fig. 5.11 is in the range 0.6 to 1.8 μm . The entire history of crack opening displacement (u_y) is given in Appendix A.

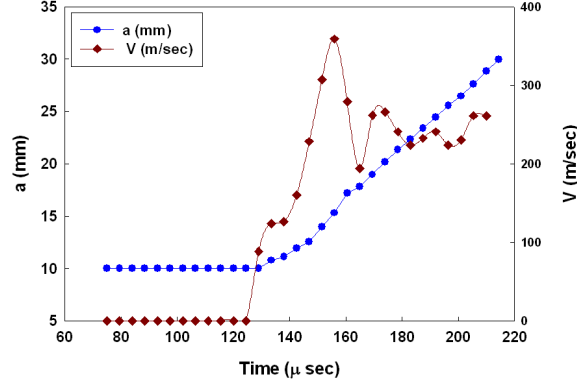


Figure 5.10: Crack growth behavior in epoxy sample under mode-I dynamic loading. Crack length history and crack speed history

5.5.1 Extraction of stress intensity factors

Since crack opening displacement, u_y being the dominant displacement component for a mode-I test, only Eq. 5.5 or 5.7 is sufficient to extract the SIFs. However, for mode-I tests, T -stress was also extracted from displacements. Therefore Eq. 5.5 is written in a different form as

$$\begin{aligned}
 u_y = & A_0(t) \frac{r^{1/2}}{\mu} \sin \frac{\theta}{2} \left(\frac{2}{1+\nu} - \cos^2 \frac{\theta}{2} \right) - \frac{\nu B_0(t)}{\mu(1+\nu)} r \sin \theta \\
 & - C_0(t) \frac{r^{1/2}}{\mu} \cos \frac{\theta}{2} \left(\frac{1-\nu}{1+\nu} - \sin^2 \frac{\theta}{2} \right) - \frac{D_0(t)}{\mu(1+\nu)} r \cos \theta \\
 & + Pr \cos \theta + Qr \sin \theta + Cr^0 + O(r^{3/2}). \tag{5.14}
 \end{aligned}$$

In the above equation, (r, θ) are crack tip polar coordinates and μ, ν are shear modulus and Poisson's ratio of the material. Also, $A_0, B_0, C_0, D_0, P, Q, C$ are constant coefficients

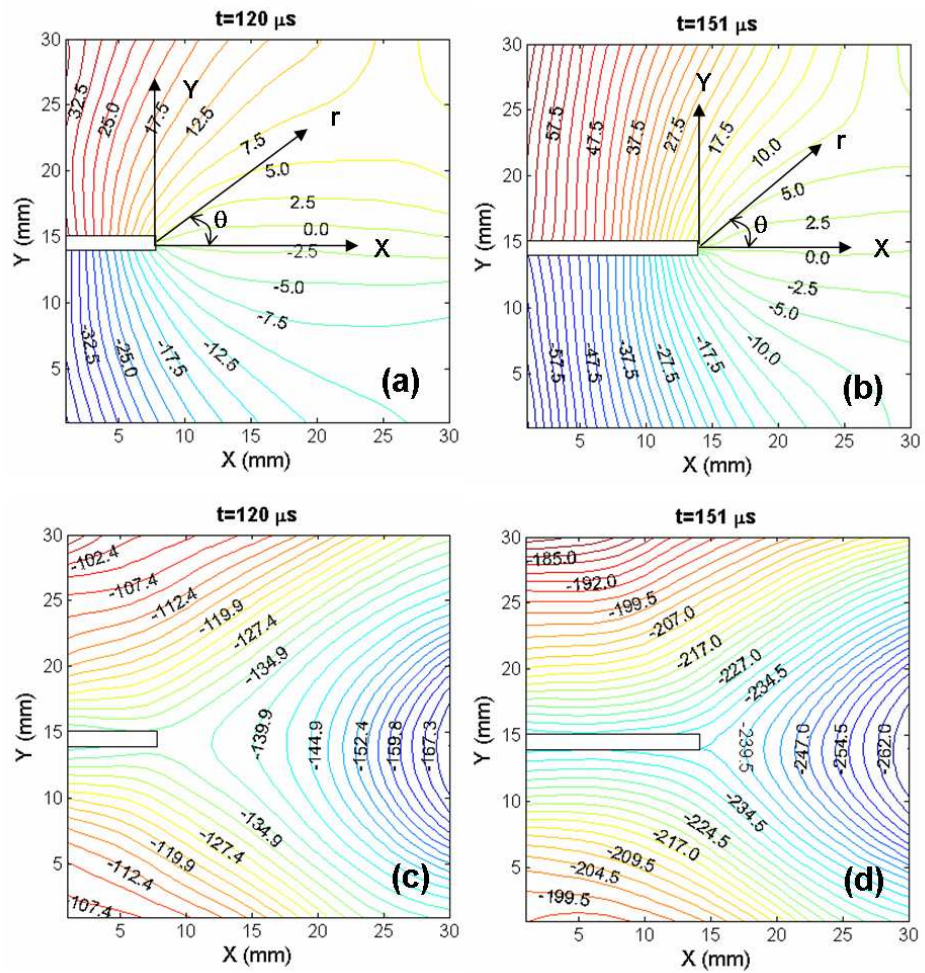


Figure 5.11: Crack opening and sliding displacements (in μm) for pre- and post-crack initiation instants. (a) v -displacement and (c) u -displacement before crack initiation (at $t = 120 \mu\text{s}$); (b) v -displacement and (d) u -displacement after crack initiation ($t = 151 \mu\text{s}$). Crack initiation time $\sim 133 \mu\text{s}$.

of the asymptotic expansion. The mode-I and mode-II dynamic stress intensity factors $K_I(t)$ and $K_{II}(t)$ are related respectively to the constants A_0 and C_0 as $K_I(t) = A_0\sqrt{2\pi}$ and $K_{II}(t) = C_0\sqrt{2\pi}$. The quantity $2B_0$ is the so-called T -stress. In Eq. 5.14, the first two terms represent symmetric deformations (mode-I), third and the fourth terms represent anti-symmetric deformation (mode-II), fifth, sixth and seventh terms are to account for rotation and rigid body translations. Equation 5.14 implicitly assumes that inertial effects enter the coefficients while retaining the functional form of the quasi-static crack tip equation. However, once the crack initiates, Eq. 5.7, which is valid for a steadily propagating crack, is used.

The stress intensity factors were extracted by performing over-deterministic least-squares analysis as explained in the section 5.4.1. The crack opening displacement field obtained from DIC superposed with the ones obtained from least-squares fit of SIF solution is shown for two time instants (one before crack initiation and one after) in Fig. 5.12. The synthetic contours are plots of Eq. (5.14) in Fig. 5.12(a) and Eq. (5.7) in Fig. 5.12(b) with only K -dominant terms. The least-squares fit considering K -dominant solution shows a good agreement with the experimental data. Figure 5.13 shows SIF history extracted from displacements. The crack initiation time is indicated by a vertical dotted line. The mode-I SIF, K_I , increases monotonically up to crack initiation at $133 \mu\text{s}$. Following initiation at $K_I \sim 1.1 \text{ MPa m}^{1/2}$, SIF continues to increase until it reaches a value of $\sim 1.7 \text{ MPa m}^{1/2}$ beyond which it remains constant. The mode-II SIF, K_{II} remains close to zero within an acceptable experimental error, as expected for a mode-I experiment. This oscillation of K_{II} about zero represents errors associated with the evaluation of stress intensity factors using least-squares method as well as loading asymmetries of the sample. The K_I history

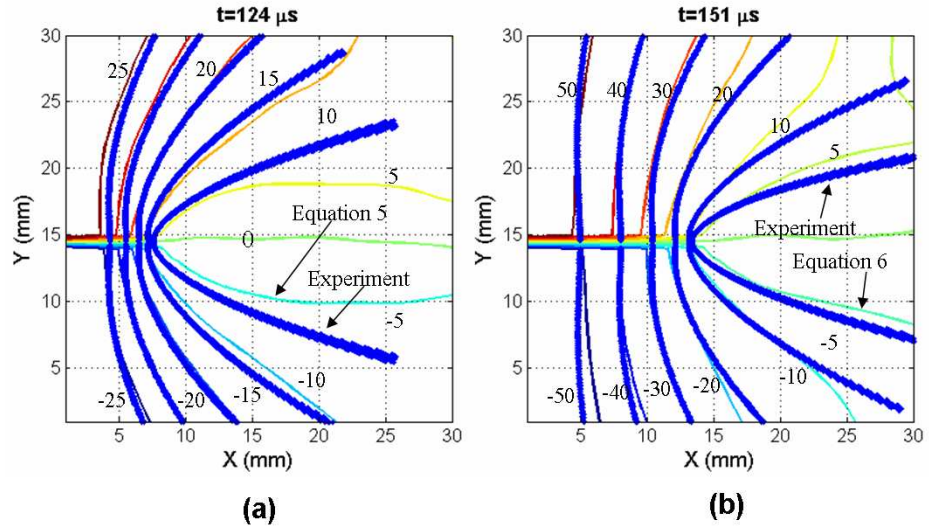


Figure 5.12: Examples showing quality of least-squares fit of displacement data; Crack opening displacement field (μm) obtained from DIC and synthetic contours for **(a)** $t = 124 \mu\text{s}$ (before crack initiation) and **(b)** $t = 151 \mu\text{s}$ (after crack initiation). Crack initiation time = $133 \mu\text{s}$

evaluated from experiments is in good agreement with the ones from finite element computation up to crack initiation. Once K_I and T -stress histories were extracted, the in-plane constraint $\beta = T\sqrt{\pi a}/K_I$ was also computed and is plotted in Fig. 5.14 along with the one from finite element method up to crack initiation. A large negative β can be observed at initial stages which is typical of TPB samples under dynamic loading conditions [77, 88]. Just before crack initiation, β value is about -0.35 which in agreement with authors previous work [77]. A reasonably good agreement of experimental β with that of finite element values can also be seen from this figure.

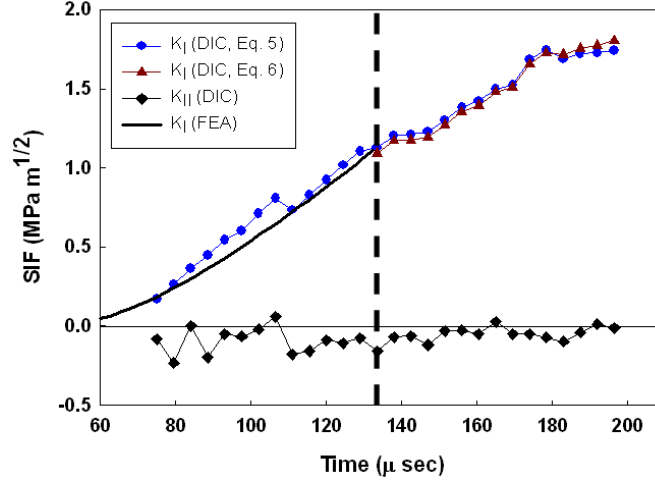


Figure 5.13: Stress intensity factors extracted from displacement field obtained from image correlation. SIF history obtained from finite element simulation up to crack initiation is also shown.

5.5.2 Estimation of strains

The crack tip normal strains obtained using the methodology described earlier are shown in Fig. 5.15 for the two images, one before and one after crack initiation. Figures 5.15(a) and (b) show ϵ_{yy} strain at 120 μs and 151 μs after impact, respectively. Normal strain contours from finite element results at $t = 120 \mu\text{s}$ is also shown in Fig. 5.15(c). To facilitate direct comparison, an increment of $140 \mu\epsilon$ was chosen between each contour level in all these plots. Symmetric mode-I normal strain contours, concentrated around the crack tip can be seen in these figures. A severe concentration of strain contours around the crack tip can be seen in Fig. 5.15(a). However, in Fig. 5.15(b), the density of strain contours moderate around the propagating crack tip. The strain value of a contour at a certain distance from the crack tip is large in Fig. 5.15(b) compared to the one in Fig. 5.15(a). This is in agreement with SIF history where K_I increases from $\sim 0.9 \text{ MPa m}^{1/2}$ at $t = 120 \mu\text{s}$ to $\sim 1.3 \text{ MPa m}^{1/2}$ at $t = 151 \mu\text{s}$ (Fig. 5.13(a)). In Fig. 5.15(a), tilting of the near-tip strain

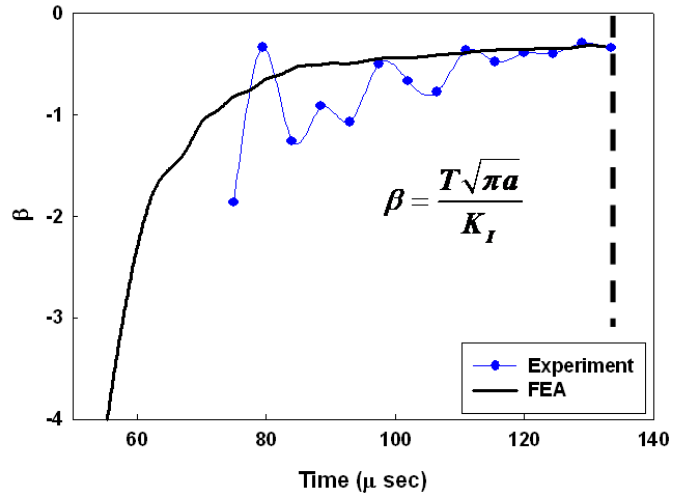


Figure 5.14: Crack tip in-plane constraint, β obtained from experiments and finite element simulation. The broken line corresponds to crack initiation time.

contours away from the crack tip indicates the presence of negative T -stress component. However, once the crack initiates and propagates, the T -stress tends to approach zero and later on become positive in a TPB geometry. Accordingly, strain contours show a smaller tilt in Fig. 5.15(b). Further, the qualitative similarity between the strain contours obtained from the experiments and finite element simulation can be readily noted from Figs. 5.15(a) and (c).

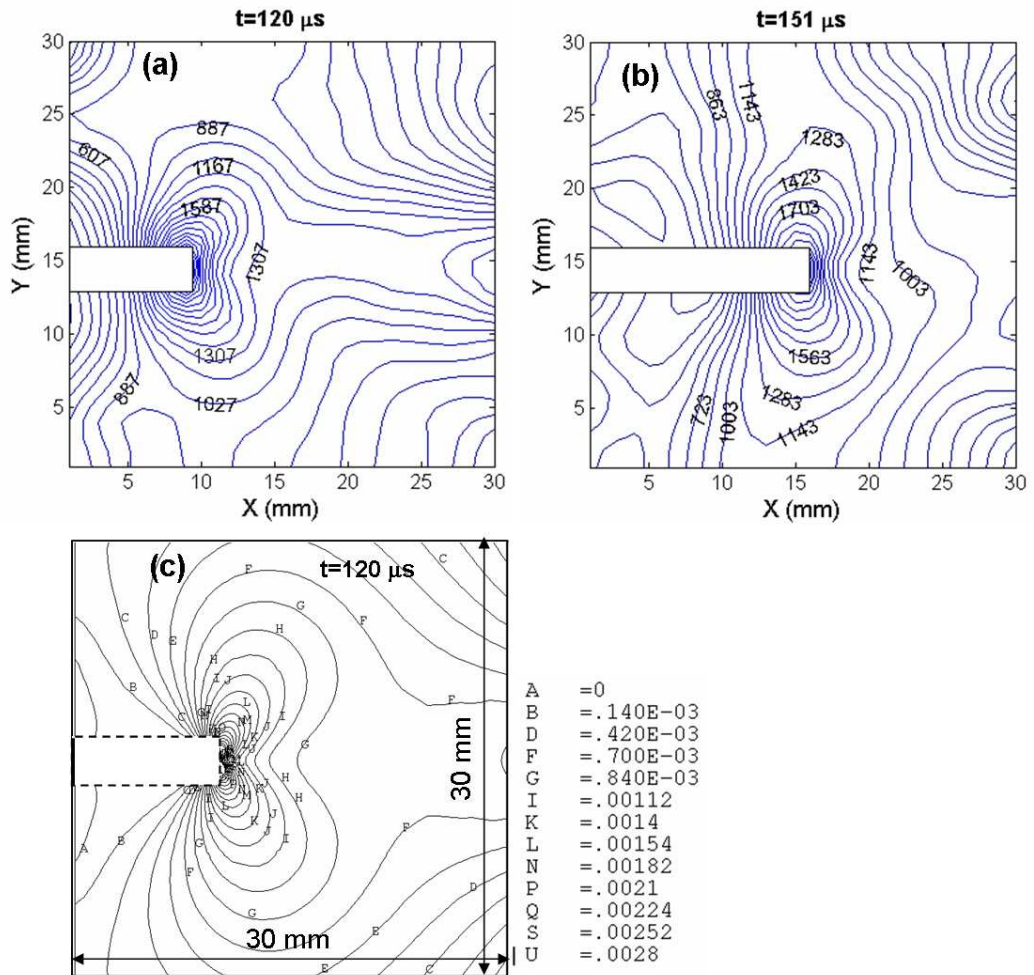


Figure 5.15: Crack tip normal strains (in micro strains) for pre- and post-crack initiation. Normal strain ϵ_{yy} at (a) $t = 120 \mu s$ and (b) at $t = 151 \mu s$ and (c) ϵ_{yy} from finite element analysis at $t = 120 \mu s$. Crack initiation time = $133 \mu s$.

CHAPTER 6

NUMERICAL PROCEDURES FOR MODELING DYNAMIC FRACTURE IN FGM

In this chapter, finite element procedures for modeling mixed-mode dynamic crack propagation in FGM are detailed. Cohesive element formulation and its implementation in ABAQUS/Standard commercial finite element software under the option of user-defined element (UEL) is described. Using this option, exponential and bilinear types of traction separation laws are implemented. The governing equations for elastodynamic simulation and the associated numerical procedure in ABAQUS/Standard using implicit time integration are also briefly discussed. Most of the studies reported in the literature use explicit time integration. But the attractive and easy to implement feature of UEL in ABAQUS/Standard prompted adopting an implicit time integration scheme in the current work. Generally for large problems with material nonlinearities, explicit methods are preferred over implicit methods in view of minimizing the solution cost. However, in the current problem, the only nonlinearity is from the traction-separation law. For such a mildly nonlinear problem, using implicit schemes can be justified considering superior convergence rate of Newtons method in ABAQUS/Standard. Also, developing a user-defined element over using the cohesive elements provided in ABAQUS 6.5, gives flexibility in terms of applying spatially varying cohesive element properties to FGM.

6.1 Elastodynamic governing equations

The governing equations for dynamic response of a structure can be derived by requiring the work of external forces to be absorbed by the work of internal, inertial and viscous forces

for a small kinematically admissible motion (any small displacement field that satisfies compatibility conditions as well as essential (kinematic) boundary conditions). Therefore the governing equation in its weak form (after carrying out variational formulation) can be written as [89]

$$\begin{aligned} \{\delta a\}^T \left[\left\{ \int_{V_e} \rho [N]^T [N] dV \right\} \{\ddot{u}\} + \left\{ \int_{V_e} c_d [N]^T [N] dV \right\} \{\dot{u}\} + \left\{ \int_{V_e} [B]^T \{\sigma\} dV \right\} \right. \\ \left. - \left\{ \int_{V_e} [N]^T \{F\} dV \right\} - \left\{ \int_{S_e} [N]^T \{\Phi\} dS \right\} - \sum_{i=1}^n P_i \right] = 0. \end{aligned} \quad (6.1)$$

In this equation, $\{\delta a\}$ are small arbitrary displacements, $[F]$ are body forces, $[\Phi]$ are prescribed surface tractions, P_i are concentrated loads. Further, dV and dS are elemental volume and elemental surface area, respectively, ρ is mass density and c_d is material damping parameter. The integration is carried out over the element volume V_e and surface area S_e . The displacement (which is a function of space and time), velocity and acceleration fields are given by,

$$\{u\} = [N]\{a\}, \quad \{\dot{u}\} = [N]\{\dot{a}\}, \quad \{\ddot{u}\} = [N]\{\ddot{a}\}, \quad (6.2)$$

where $[N]$ are shape functions and $[u]$ are nodal degrees of freedom. Since $\{\delta a\}$ are arbitrary, by combining Eqs. 6.1 and 6.2, finite element approximation to the equilibrium equation 6.1 can be written as

$$[m]\{\ddot{u}\} + [c]\{\dot{u}\} + [k]\{u\} = \{r^{ext}\}. \quad (6.3)$$

Here $[m]$ and $[c]$ are consistent mass matrix and consistent damping matrix, respectively, and $[k] = \int_{V_e} [B]^T [E] [B] dV$ is stiffness the matrix. Further, $\{r^{ext}\}$ is the external force

vector which is the summation of body forces, surface tractions and concentrated loads. For an assembled structure, global finite element equations are written as

$$[M]\{\ddot{U}\}_n + [C]\{\dot{U}\}_n + [K]\{U\}_n = [R^{ext}]. \quad (6.4)$$

Here the subscript n denotes $n\Delta t$ where Δt is the time step size. The absence of time step subscripts for matrices $[M]$, $[C]$ and $[K]$ implies linearity. But for problems with material nonlinearity, $[K]$ is a function of displacement and therefore of time also. In the current work, the damping matrix C is not used. The algorithmic damping (Section 6.2) available from the implicit scheme provides just enough damping for the program to run smoothly. Direct integration of Eq. 6.4 can be performed by two methods, *explicit* and *implicit*. Explicit methods have the form [89]

$$\{U\}_{n+1} = f(\{U\}_n, \{\dot{U}\}_n, \{\ddot{U}\}_n, \{U\}_{n-1}, \dots) \quad (6.5)$$

and therefore allow $\{D\}_{n+1}$ to be determined completely in terms of historical information of displacements and their time derivatives at time $n\Delta t$ and before. Whereas implicit methods have the form

$$\{U\}_{n+1} = f(\{\dot{U}\}_{n+1}, \{\ddot{U}\}_{n+1}, \{U\}_n, \{\dot{U}\}_n \dots). \quad (6.6)$$

The computation of $\{U\}_{n+1}$ requires the information of time derivatives of $\{U\}_{n+1}$, which are unknowns. Therefore iterations need to be performed for achieving convergence to an acceptable solution for $\{U\}_{n+1}$.

6.2 Implicit integration of dynamic equations in ABAQUS

ABAQUS uses Hilber, Hughes and Taylor (HHT) implicit operator [90] for time integration in dynamic problems. This operator replaces the actual equilibrium Eq. (6.4) with a balance of inertial forces at the end of a time step and a weighted average of the static forces at the beginning and at the end of a time step [91].

$$[M](\ddot{U})_{t+\Delta t} + (1 + \alpha_d)\{(R^{int})_{t+\Delta t} - (R^{ext})_{t+\Delta t}\} - \alpha_d\{(R^{int})_t - (R^{ext})_t\} = 0. \quad (6.7)$$

Here \ddot{U} is the acceleration field and α_d is a parameter that controls algorithmic damping. Further, M , R^{int} and R^{ext} are consistent mass matrix, internal force vector and external force vectors. The HHT operator uses Newmark formulae for displacement and velocity integration:

$$U_{t+\Delta t} = U_t + \Delta t \dot{U}_t + \Delta t^2 \left[\left(\frac{1}{2} - \beta \right) \ddot{U}_t + \beta \ddot{U}_{t+\Delta t} \right] \quad (6.8)$$

and

$$\dot{U}_{t+\Delta t} = \dot{U}_t + \Delta t \left[(1 - \gamma) \ddot{U}_t + \gamma \ddot{U}_{t+\Delta t} \right] \quad (6.9)$$

where

$$\beta = \frac{1}{4}(1 - \alpha_d)^2, \quad \gamma = \frac{1}{2} - \alpha_d \quad \text{and} \quad -\frac{1}{3} \leq \alpha_d \leq 0. \quad (6.10)$$

In this equation, α_d is the parameter that controls algorithmic damping. When $\alpha_d = 0$, β and γ take the values of 1/4 and 1/2 respectively, which is the requirement for an unconditional stability of an implicit time integration scheme. With these values, the operator reduces to a trapezoidal rule without any damping. In the current work, a value of -0.05

is chosen for α_d . This ensures that numerical dissipation is less than 1% of the total energy which helps to remove the participation of high frequency modal components and yet maintain good accuracy in the important lower modes.

6.3 Formulation of an element in ABAQUS

Formulation of a user-defined element (UEL) in ABAQUS/Standard involves providing the contribution of the element to the Jacobian matrix and the residual force vector in a generic nonlinear solution step. Before presenting the details of the UEL implementation, the solution of nonlinear equations in ABAQUS/Standard using Newton's method is briefly discussed. Consider the equilibrium equations from the principle of virtual work. Let, U_i^M be the approximate solution after iteration i , and ΔU_{i+1}^M be the difference between this solution and the exact solution to the discrete equilibrium equation 6.7 which can be written as [91],

$$F^N(U_i^M + (\Delta U)_{i+1}^M) = 0. \quad (6.11)$$

Expanding this equation about the approximate solution u_i^M using the Taylor's series gives

$$F^N(U_i^M) + \frac{\partial F^N}{\partial U^P}(U_i^M)(\Delta U_{i+1}^P) + \frac{\partial^2 F^N}{\partial U^P \partial U^Q}(U_i^M)(\Delta U_{i+1}^P)(\Delta U_{i+1}^Q) + \dots = 0. \quad (6.12)$$

If the approximation U_i^M is close to the actual solution, then the magnitude of ΔU_{i+1}^P will be small and hence the third and higher order terms can be neglected to get a linear system of equations

$$K_i^{NP}(\Delta U)_{i+1}^P = -F_i^N \quad (6.13)$$

where

$$K_i^{NP} = \frac{\partial F^N}{\partial U^P}(U_i^M) \quad (6.14)$$

is the Jacobian matrix and

$$F_i^N = F^N(U_i^M) \quad (6.15)$$

is the residual vector. The next approximation to the solution is then

$$U_{i+1}^M = U_i^M + (\Delta U)_{i+1}^M. \quad (6.16)$$

In general, for implicit dynamic analysis, the contribution of UEL to the Jacobian matrix is given by,

$$K_i^{NP} = \frac{\partial F^N}{\partial U^P} + \frac{\partial F^N}{\partial \dot{U}^P} \left(\frac{d\dot{U}}{dU} \right)_{t+\Delta t} + \frac{\partial F^N}{\partial \ddot{U}^P} \left(\frac{d\ddot{U}}{dU} \right)_{t+\Delta t} \quad (6.17)$$

where

$$\left(\frac{d\dot{U}}{dU} \right)_{t+\Delta t} = \frac{\gamma}{\beta \Delta t}, \quad \left(\frac{d\ddot{U}}{dU} \right)_{t+\Delta t} = \frac{1}{\beta \Delta t^2}, \quad (6.18)$$

for HHT implicit operator. The term $\partial F^N / \partial \dot{U}^M$ is the user-element's damping matrix and $\partial F^N / \partial \ddot{U}^M$ is the mass matrix. Since there is no mass and damping associated with a cohesive element, the last two terms in Eq. 6.17 vanish and only the first term (stiffness matrix) needs to be provided to the overall system of equations.

6.4 Cohesive element formulation

Figure 6.1(a) shows finite element mesh with embedded cohesive elements along a potential failure path. The deformed mesh is shown in Fig. 6.1(b). Let A and B be two coincident material points on a potential crack path in the undeformed configuration. (see

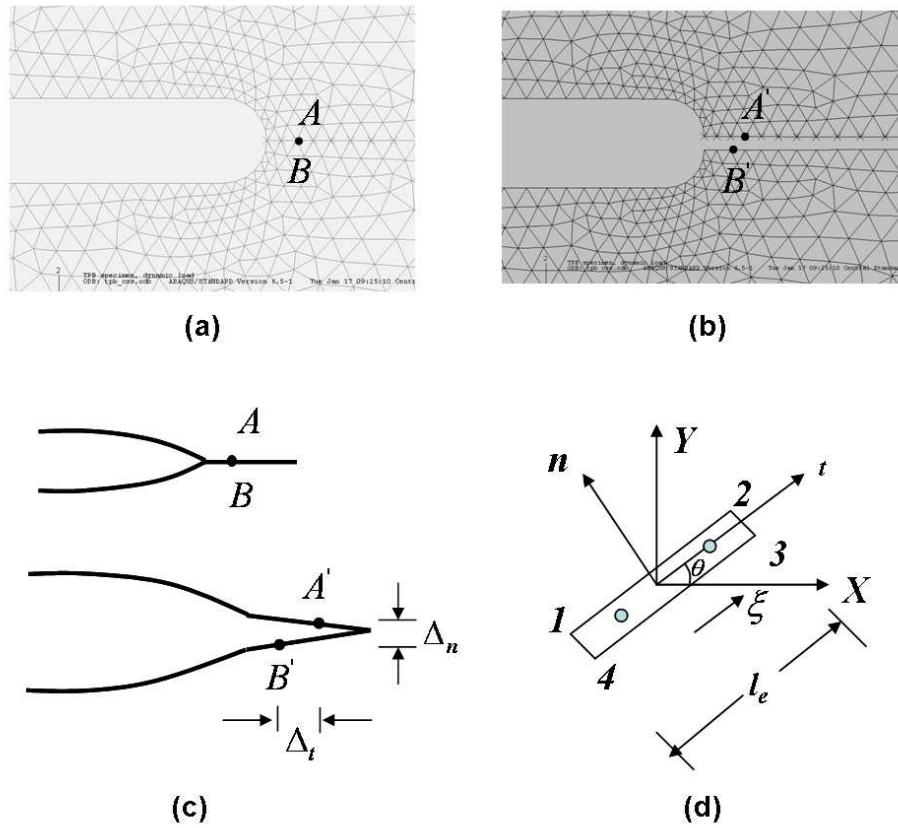


Figure 6.1: (a) Undeformed and (b) deformed finite element mesh near a notch tip, (c) Schematic showing separation of nodes in a cohesive element and (d) local and global coordinate system used for a cohesive element.

Figs. 6.1(a) and (c). As deformation occurs, the new positions of these points be A' and B' as shown in Fig. 6.1(c). Let Δ_n and Δ_t be the normal and tangential components of separation between points A' and B' . Let a cohesive element shown in Fig. 6.1(b) and (c) be present on this potential crack path. Then the separation in the X - and Y -directions at

a Gauss point can be computed from nodal displacements $[U]$ available from ABAQUS

$$\begin{bmatrix} U_X \\ U_Y \end{bmatrix} = [N][U], \quad (6.19)$$

where

$$[N] = \begin{bmatrix} N_1 & 0 & N_2 & 0 & -N_2 & 0 & -N_1 & 0 \\ 0 & N_1 & 0 & N_2 & 0 & -N_2 & 0 & -N_1 \end{bmatrix} \quad (6.20)$$

and

$$[U] = [U_1 \quad V_1 \quad U_2 \quad V_2 \quad U_3 \quad V_3 \quad U_4 \quad V_4]^T. \quad (6.21)$$

Here $N_1 = (1-\xi)/2$ and $N_2 = (1+\xi)/2$ are linear shape functions and $\xi = \pm 1/\sqrt{3}$ is the sampling location. The length of a cohesive element is given by $l_e = \sqrt{(X_2 - X_1)^2 + (Y_2 - Y_1)^2}$.

The tangential and normal separations are given by,

$$\begin{bmatrix} \Delta_t \\ \Delta_n \end{bmatrix} = [Q] \begin{bmatrix} U_X \\ U_Y \end{bmatrix}, \quad \text{where} \quad [Q] = \begin{bmatrix} \cos \theta & \sin \theta \\ -\sin \theta & \cos \theta \end{bmatrix}. \quad (6.22)$$

6.4.1 Exponential traction-separation law

Once separations are computed in a cohesive element, the next step is to evaluate tractions arising due to these separations. This needs a constitutive law for the cohesive surface. In this section, a phenomenological mechanical relation between traction and displacement jumps across the cohesive surface is considered to be in the form of an exponential relation [58]. The traction vector $\mathbf{T} = (T_n, T_t)$ at the cohesive surface is derived from an interfacial

potential given by Xu and Needleman [58]

$$\mathbf{T} = \frac{\partial \phi}{\partial \mathbf{\Delta}} \quad (6.23)$$

with $\mathbf{\Delta} = (\Delta_n, \Delta_t)$, and

$$\phi(\Delta_n, \Delta_t) = \phi_n + \phi_n e^{-\frac{\Delta_n}{\delta_n}} \left[\left\{ 1 - r + \frac{\Delta_n}{\delta_n} \right\} \left\{ \frac{1-q}{r-1} \right\} - \left\{ q + \left(\frac{r-q}{r-1} \right) \frac{\Delta_n}{\delta_n} \right\} e^{-\frac{\Delta_t^2}{\delta_t^2}} \right], \quad (6.24)$$

where δ_n and δ_t represent characteristic separations (maximum values of Δ_n and Δ_t) in such a way that $T_n(\delta_n) = \sigma_{max}$ and $T_t(\delta_t/\sqrt{2}) = \tau_{max}$. Further, $q = \phi_t/\phi_n$ and $r = \Delta_n^*/\delta_n$, where Δ_n^* is the value of Δ_n when complete shear separation has taken place without resulting in normal tension ($T_n = 0$). In the current work, q is assumed as one and r as zero. The expressions for normal and shear tractions can be obtained by differentiating ϕ with respect to Δ_n and Δ_t ,

$$T_n = \frac{\phi_n}{\delta_n} e^{-\frac{\Delta_n}{\delta_n}} \left[\frac{\Delta_n}{\delta_n} e^{-\frac{\Delta_t^2}{\delta_t^2}} + \frac{1-q}{r-1} \left\{ 1 - e^{-\frac{\Delta_t^2}{\delta_t^2}} \right\} \left\{ r - \frac{\Delta_n}{\delta_n} \right\} \right], \quad (6.25)$$

$$T_t = 2 \left(\frac{\phi_n \Delta_t}{\delta_t^2} \right) \left\{ q + \left(\frac{r-q}{r-1} \right) \frac{\Delta_n}{\delta_n} \right\} e^{-\frac{\Delta_n}{\delta_n}} e^{-\frac{\Delta_t^2}{\delta_t^2}}. \quad (6.26)$$

In the above equation, ϕ_n is the work of normal separation, ϕ_t is the work of tangential separation. They represent the amount of work needed for complete separation. This can be seen for $q = 1$, $r = 0$, and assuming that $T_n = T_n(\Delta_n, \Delta_t = 0)$, $T_t = T_t(\Delta_n = 0, \Delta_t)$, for which case uncoupled tractions are obtained. Using $T_n(\delta_n) = \sigma_{max}$ and $T_t(\delta_t/\sqrt{2}) = \tau_{max}$, the following relations

$$\phi_n = e \sigma_{max} \delta_n, \quad \phi_t = \sqrt{\frac{e}{2}} \tau_{max} \delta_t, \quad (6.27)$$

are obtained for ϕ_n and ϕ_t . Here σ_{max} and τ_{max} are cohesive surface normal strength and shear strength, respectively. The normalized traction curves for uncoupled separations are shown in Fig. 6.2. The variation of pure normal traction (in the absence of tangential separation, $\Delta_t = 0$) with normal separation is shown in Fig. 6.2(a). Similarly, the variation of tangential traction with tangential separation (in the absence of normal separation, $\Delta_n = 0$) is shown in Fig. 6.2(b). In these figures, the tractions are normalized with respect to their maximum values (σ_{max} and τ_{max}). The normal traction monotonically increases with normal separation until a maximum value is reached at δ_n . After that cohesive force decreases until the cohesive zone no longer has any stiffness in the normal direction. When the normal separation becomes negative (interpenetration), the traction rapidly becomes more negative to discourage inter-penetration. The shear tractions do not show such a variation. The tangential separation in the negative direction results in shear traction in the negative direction.

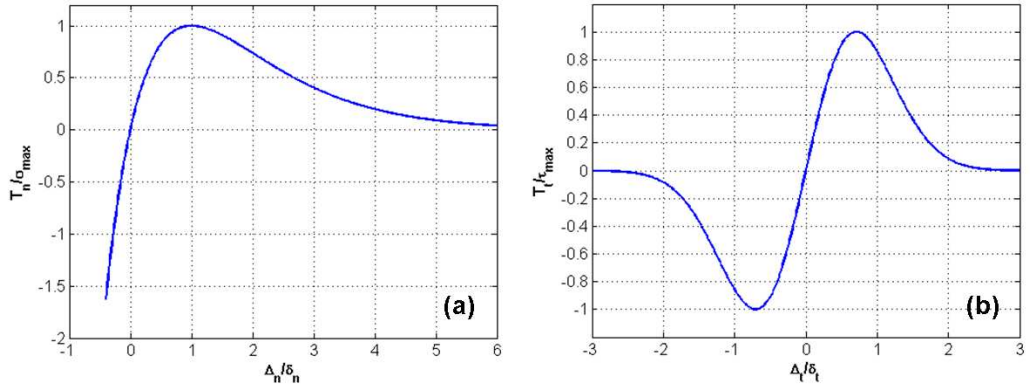


Figure 6.2: Exponential traction-separation law showing uncoupled loading: variations of (a) pure normal traction with normal separation and (b) pure tangential traction with tangential separation.

In Figs. 6.2, uncoupled relations are illustrated. But in reality, the Eqs. 6.25 and 6.26 are indeed surfaces which are illustrated in Figs. 6.3(a) and (b). In Fig. 6.3(a), it can be seen that a non-zero value of Δ_t causes lower values for the curve $T_n(\Delta_n)$ relation. Similarly a non-zero value of Δ_n results in lower values for the curve $T_t(\Delta_t)$. The expressions for stiffness coefficients are obtained by differentiating tractions with respect to separations. The details for the same are provided in Appendix B.

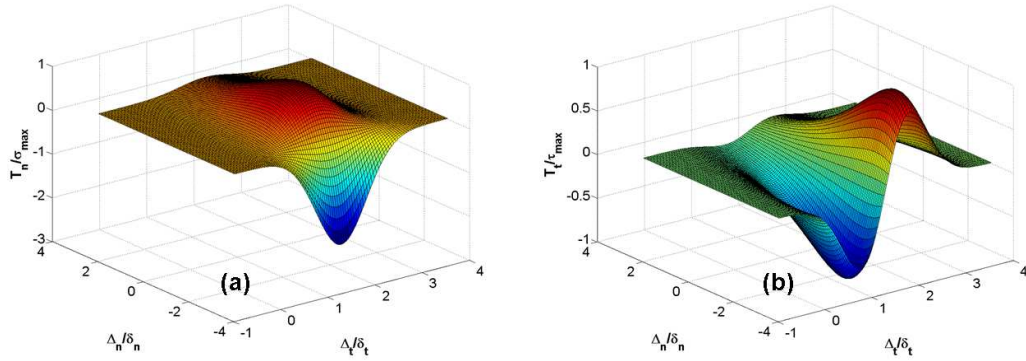


Figure 6.3: Exponential traction-separation law showing coupled loading: variations of (a) normal traction and (b) tangential traction.

6.4.2 Bilinear traction-separation law

The exponential traction-separation law (TSL) has continuous normal to the traction surface and hence easy to implement. However, the initial slope of the traction-separation surface can not be changed for a given set of values of cohesive properties. This introduces an artificial compliance into the finite element model and results in overall structure becoming softer than what it actually is. In case of bilinear TSL, the initial slope can be adjusted (to be discussed in section 7.4.2). Therefore in this work, bilinear TSL is chosen and its initial slope is set to a very high value so that the artificial compliance effects are minimized.

After evaluating normal and tangential separations (as explained in section 6.4), a non-dimensional effective separation parameter λ is computed by,

$$\lambda = \sqrt{\left(\frac{\Delta_n}{\delta_n}\right)^2 + \beta_c^2 \left(\frac{\Delta_t}{\delta_t}\right)^2}. \quad (6.28)$$

Here δ_t and δ_n are critical values of tangential and normal separations respectively. The parameter $\beta_c^2 = G_{IIC}/G_{IC}$ is the ratio between mode-I and mode-II fracture energies. At time $t = 0$, λ takes the value of zero. As the cohesive element separates, λ increases in magnitude and attains a value of unity when the separation complete.

The variation of pure normal traction (in the absence of tangential separation, $\Delta_t = 0$) with normal separation is shown in Fig. 6.4(a). Similarly, the variation of tangential traction with tangential separation (in the absence of normal separation, $\Delta_n = 0$) is shown in Fig. 6.4(b). The critical values of normal and tangential separations are computed by equating the area under $T - \Delta$ curves to mode-I and mode-II fracture energies,

$$G_{IC} = \frac{1}{2}\delta_n T_{max}, \quad G_{IIC} = \alpha_c \frac{1}{2}\delta_t T_{max} \quad (6.29)$$

where ($\alpha_c = \beta_c^2 \delta_n / \delta_t$) is a parameter coupling normal and shear tractions. Traction-separation relations for various portions of the triangle are given as follows: For loading/unloading in the range $0 \leq \lambda \leq \lambda_{cr}$,

$$T_t = \alpha_c \frac{T_{max} \Delta_t}{\lambda_{cr} \delta_t}, \quad T_n = \frac{T_{max} \Delta_n}{\lambda_{cr} \delta_n}. \quad (6.30)$$

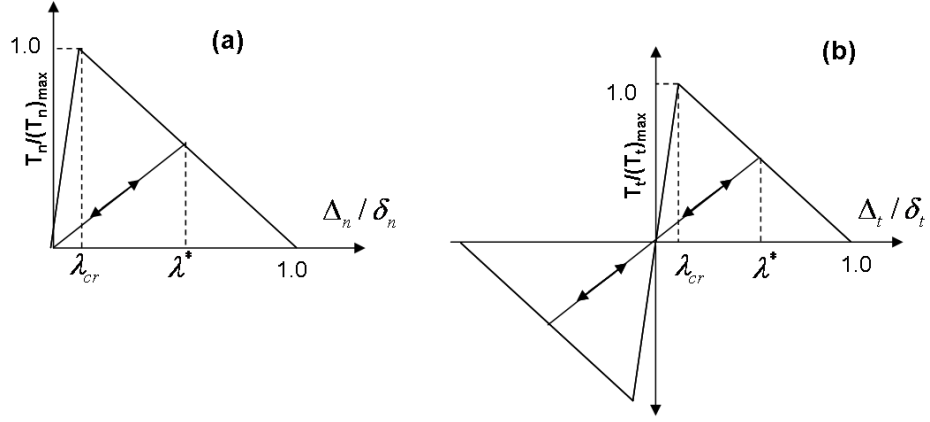


Figure 6.4: Prescribed bilinear traction-separation law for **(a)** pure normal traction versus normal separation and **(b)** pure tangential traction versus tangential separation.

For loading in the range $\lambda_{cr} < \lambda \leq 1$,

$$T_t = \alpha_c \frac{T_{max}(1 - \lambda)\Delta_t}{\lambda(1 - \lambda_{cr})\delta_t}, \quad T_n = \frac{T_{max}(1 - \lambda)\Delta_n}{\lambda(1 - \lambda_{cr})\delta_n}. \quad (6.31)$$

For unloading/reloading in the range $0 < \lambda \leq \lambda^*$ where λ^* is the maximum value of λ after which unloading starts,

$$T_t = \alpha_c \frac{T_{max}\Delta_t}{\lambda^*\delta_t}, \quad T_n = \frac{T_{max}\Delta_n}{\lambda^*\delta_n}. \quad (6.32)$$

For loading in the range $\lambda^* < \lambda \leq 1$,

$$T_t = \alpha_c \frac{T_{max}(1 - \lambda)\Delta_t}{\lambda(1 - \lambda^*)\delta_t}, \quad T_n = \frac{T_{max}(1 - \lambda)\Delta_n}{\lambda(1 - \lambda^*)\delta_n}. \quad (6.33)$$

The stiffness coefficients are determined by differentiating tractions with respect to separations as follows. The details can be found in Appendix B.

$$[SS] = \begin{bmatrix} SS(1,1) & SS(1,2) \\ SS(2,1) & SS(2,2) \end{bmatrix} = \begin{bmatrix} \partial T_t / \partial \Delta_t & \partial T_t / \partial \Delta_n \\ \partial T_n / \partial \Delta_t & \partial T_n / \partial \Delta_n \end{bmatrix}. \quad (6.34)$$

6.5 Implementation details

The element stiffness matrix and internal force vector are computed by performing the usual Gauss-quadrature numerical integration as follows,

$$[S]_{8 \times 8}^e = \int_{-1}^1 [N^T]_{8 \times 2} [Q^T]_{2 \times 2} [SS]_{2 \times 2} [Q]_{2 \times 2} [N]_{2 \times 8} \frac{l_e}{2} d\xi, \quad (6.35)$$

and

$$[P]_{8 \times 1}^e = \int_{-1}^1 [N^T]_{8 \times 2} [Q]_{2 \times 2} [T]_{2 \times 1} \frac{l_e}{2} d\xi. \quad (6.36)$$

The effect of introducing a user-defined element to the finite element model during a non-linear analysis step is that the element should provide its contribution to the *residual force vector* and the *Jacobian matrix* to the overall system of equations (see Ref. [91]). In the current model, since there are no external forces applied to the cohesive elements, the internal force vector (traction forces developed due to separation) as given by Eq. 6.36 becomes the residual force vector. Also, since there is no mass associated with cohesive elements, the stiffness matrix given by Eq. 6.35 becomes the Jacobian matrix. Once these two quantities are computed and passed as arguments in to ABAQUS, the software internally assembles these to formulate the global system of equations and solution proceeds with automatic time stepping.

The flowchart shown in Fig. 6.5 explains all the steps involved in implementing cohesive element as user-defined element (UEL) in ABAQUS/Standard. Using the nodal coordinates available from ABAQUS, length and orientation of an element are computed, transformation matrix from local element coordinate system to global Cartesian system is established. From nodal coordinates, shape functions and Gauss point sampling locations are established. Using nodal displacements, tangential and normal separations are computed. Then damage λ is computed from Eq. 6.28. If $\lambda \geq 1$, then the element is said to have failed and subroutine is exited. Otherwise, tractions are evaluated as explained in section 6.4 and internal force vector is computed. The stiffness coefficients are computed as explained in Appendix B and numerical integration is carried out to compute element stiffness matrix.

6.6 Implicit dynamic scheme and time step control

To integrate the equations of motion, implicit time integration is adopted which uses Hilber, Hughes and Taylor implicit operator [90]. It should be noted that implicit time integration adopted here is unconditionally stable and does not have a stable step size. However, the time step size has to be small enough to capture the transient effects of the problem. The corresponding stable time step size in an explicit dynamic analysis is the time taken by the dilatational wave to travel through the smallest element in the mesh, which is

$$\Delta t \leq \frac{L_c}{C_L}, \quad (6.37)$$

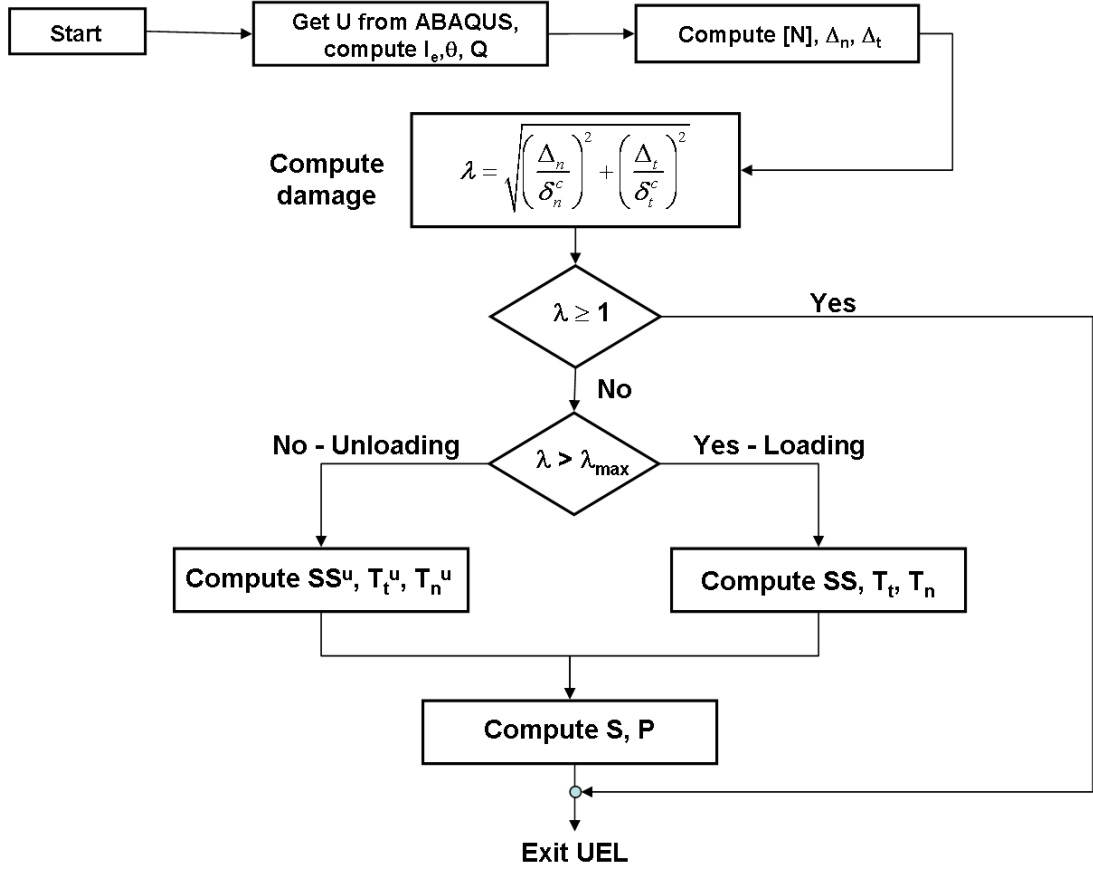


Figure 6.5: Steps involved in implementing a cohesive element as user-defined element in ABAQUS

where L_c is the smallest continuum element length in the mesh ($\sim 230 \mu\text{m}$ in the current work) and C_L , the dilatational wave speed in FGM,

$$C_L(x) = \sqrt{\frac{E(x)}{(1 + \nu(x))(1 - \nu(x))\rho(x)}}, \quad (6.38)$$

for plane stress. Here $E(x)$, $\nu(x)$ and $\rho(x)$ denote elastic modulus, Poisson's ratio and mass density of the material at a location x . The maximum value of C_L for the FGM under

consideration is 2580 m/sec at the stiffer side of the sample. Therefore, the minimum value for Δt is ~ 90 ns. However, it should be noted that implicit solutions are accurate even if the time step size is several orders of magnitude larger than the corresponding stable time step size of the explicit method. In view of this, the upper limit for the time step was set to 200 ns but once the crack initiation occurred, the program internally chose time increments as low as 40 ns. Following values were used for convergence control parameters in ABAQUS/Standard (see Ref. [91] for details). The half step residual tolerance =20, the ratio of largest residual to the corresponding average force norm (R_n^α) = 0.005 and the ratio of the largest solution correction to the largest corresponding incremental solution value (C_n^α) = 0.01.

CHAPTER 7

NUMERICAL SIMULATION OF MODE-I AND MIXED-MODE DYNAMIC FRACTURE IN FGM

In this chapter, details mixed-mode dynamic crack growth simulations in functionally graded materials are provided. Modeling aspects and application of graded material properties to the finite element model are explained. Simulations are carried out for two configurations, a crack on the compliant side and a crack on the stiffer side of the sample, as explained in Chapter 2. The crack opening displacement and crack tip normal stress histories are presented. Crack path histories are compared with those observed from experiments presented in Chapter 2. The finite element simulations of mode-I dynamic fracture of FGM samples made out of syntactic foam material are discussed in Appendix C.

7.1 Modeling aspects

The finite element mesh used in the analysis is shown in Fig. 7.1(a). In mixed mode dynamic crack growth simulations, the crack path is not known *a priori*. Therefore cohesive elements were dispersed in a region where crack propagation is anticipated to occur. Therefore, based on experimental observations, the domain to be discretized was divided into two parts, region 1 in which crack propagation was not anticipated to occur and region 2 where crack propagation was likely to occur (see Fig. 7.1(b)). The region 1 was discretized with three node 2D plane stress continuum elements in ANSYSTM commercial finite element software. The region 2 was discretized using three node plane stress elements with four node cohesive elements dispersed along their boundaries. A computer program was written in MATLABTM environment to generate the necessary mesh. Thus, the boundary

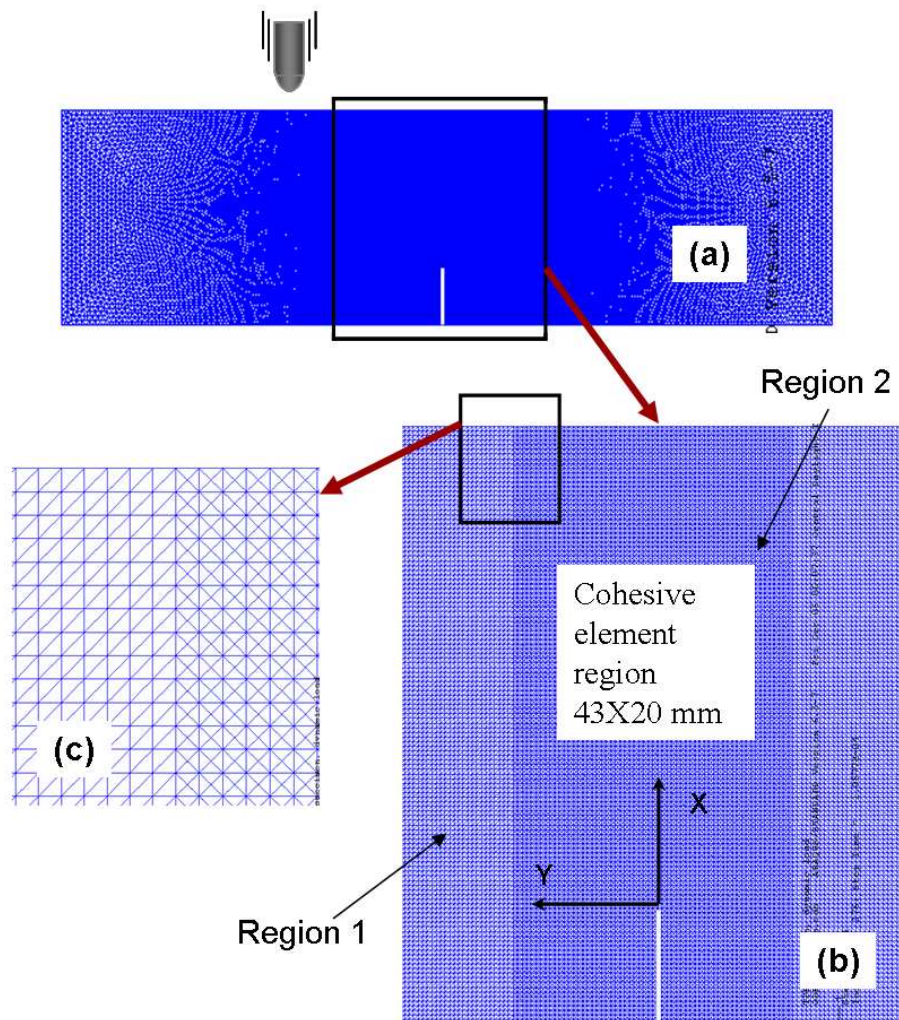


Figure 7.1: (a) Overall view of the finite element mesh used for the analysis (b) Magnified view of mesh showing region 1 and region 2 (c) Enlarged view of the mesh at the interface where the elements from region 1 and region 2 meet.

of every triangular element is a potential crack path. These two mesh patterns were joined by merging the nodes selectively along their boundaries in ANSYS. Dispersion of cohesive elements increases node count dramatically. The model contained roughly 117,000 nodes and 125,000 elements.

It is necessary to ensure that the smallest element used in the mesh is less than the characteristic cohesive length δ so that mesh sensitive results are not obtained. The size of the cohesive zone can be determined from Dugdale and Barrenblatt model [55, 56] for a mode-I crack according to which cohesive stress takes a constant value of T_{ave} up to a critical opening displacement of δ_n and vanishes thereafter. The size of the cohesive zone is given by [93, 94]

$$\delta = \frac{\pi}{8} \frac{E}{1 - \nu^2} \frac{G_{IC}}{T_{ave}^2}. \quad (7.1)$$

Here E is the elastic modulus, G_{IC} is the mode-I fracture energy and $T_{ave} = T_{max}/2$, with T_{max} being the peak stress in a bilinear traction-separation law. A lower bound estimate was made by substituting 4 GPa, 0.49 N/mm and 60 MPa for E , G_{IC} and T_{max} , respectively. The value for δ so obtained is $\sim 900 \mu\text{m}$. The smallest cohesive element size in this work was $\sim 230 \mu\text{m}$, roughly one-fourth of the characteristic cohesive length.

While conducting experiments, the FGM samples were initially rested on soft putty blocks (~ 7 mm thick) placed on supports when impact occurred. This was to preclude support reactions affecting the fracture behavior of the sample. Accordingly the sample was modeled as a free-free beam. The mass of the impactor was large compared that of the sample. Therefore a constant velocity of 5 m/s was imposed on a node located at the impact point.

7.2 Application graded material properties to continuum elements

One of the important aspects in finite element modeling of FGM is the implementation of spatially varying material properties. Anlas *et al.*[95] and Kim and Paulino [96] have developed graded finite elements in order to apply smoothly varying material properties. Rousseau and Tippur [15] used an alternative method to introduce the required spatial variation of material properties using the readily available elements in commercial finite element softwares. Since simulations in the current work were conducted using ABAQUS, it is natural to think of using a user-defined element (UMAT) to apply spatial variations of material properties as done previously by Giannakopoulos and Suresh [93] under static conditions. However, it should be noted that for a dynamic simulation, imposing spatial variation of mass density is also necessary. To authors' knowledge, this is not possible in ABAQUS by using the UMAT option. Therefore in this work, the method suggested by Rousseau and Tippur [15] was extended to mixed-mode crack growth simulation.

Consider the finite element model shown in Fig. 7.2(a). Here it is required to apply the variation of material properties (elastic modulus, mass density and Poisson's ratio) along the height of the sample W . These variations were assumed to be linear as an approximation. In the first step, an uncoupled thermal analysis was conducted with temperature boundary conditions, $T = T_a$ at the bottom edge and $T = T_b$ at the top edge. No convective boundary conditions were imposed so that temperature variation from T_a to T_b across the width W occurred only through conduction. It should be noted here that as for as thermal analysis is concerned, the elements in region 2 (where the cohesive elements are present) are disconnected and no heat flow occurs in this region. In order to overcome this difficulty, first all the cohesive elements were converted into thermally conductive elements (DGAP

in ABAQUS). That is, each four-noded cohesive element was converted into two two-noded DGAP elements. (To be more specific, in Fig. 7.2(b), nodes 1 and 2 are tied to make the first DGAP element and nodes 3 and 4 are tied to make the next element and so on). Next, for DGAP elements, a high value of thermal conductance was assigned. This was to ensure that these elements act as good conductors of heat and both nodes attain the same temperature values. The resulting linearly varying nodal temperature variation following the thermal analysis is shown in Fig. 7.2(a). In the second step, for performing structural analysis using implicit dynamic procedure in ABAQUS/Standard, nodal temperatures from the thermal analysis were imported as initial conditions to the model. When nodal temperatures are applied as boundary conditions, ABAQUS applies them in a ramped fashion over the entire time step and is undesirable. (For a static analysis, however, it does not matter whether temperature field is applied as boundary condition or as an initial condition but for a dynamic analysis, one has to ensure that nodal temperature values remain same throughout the time step.) Now by applying the temperature dependant material properties to the model, a linear variation of elastic modulus and mass density across the sample width W was achieved. Any spurious thermal stresses resulting from the temperature field were avoided by setting thermal expansion coefficient to zero throughout the analysis.

7.3 Application of material properties to cohesive elements

There are five independent properties to be specified for cohesive elements. They are mode-I fracture energy (G_{IC}), the peak cohesive stress (T_{max}), the damage parameter corresponding to the peak stress (λ_{cr}), the ratio between mode-II and mode-I fracture energies (related to β_c^2) and the parameter coupling the normal and shear tractions (α_c).

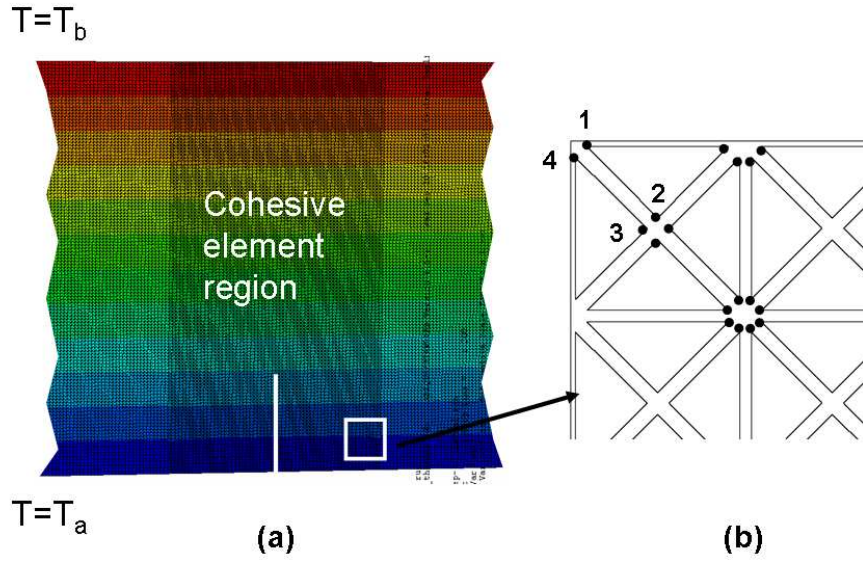


Figure 7.2: (a) Nodal temperature results from thermal analysis, (b) magnified view of the cohesive element region.

In order to model cohesive elements in FGM realistically, spatial variations of G_{IC} and T_{max} have to be incorporated into the model. The spatial variation of $K_{ICR}(X)$ is available from Fig. 3.4(c) from which $G_{IC}(X) = [K_{ICR}(X)]^2/E(X)$ for plane stress conditions was computed. The peak value of the cohesive stress is assumed to be $E(X)/100$. There is no established experimental rationale for selecting this value. For example, Xu and Needleman [58] have used $E/10$ in case of PMMA whereas Camacho and Ortiz [65] have used $E/200$ for ceramics. Accordingly, several simulations were carried out in the current work by varying the peak stress in the range $E(X)/50$ to $E(X)/100$ and the results did not show any significant difference in terms of crack path. The choice of T_{max} is relatively unimportant as long as the artificial compliance is minimum in the model. This can be ensured by specifying a high initial stiffness to the cohesive elements ($\lambda_{cr} = 0.01$). The parameter β_c and α_c were chosen as follows. A mixed-mode dynamic fracture experiment, carried out

by the authors [31] on a homogeneous sample under similar experimental conditions (same impact velocity, specimen dimensions, etc.) was used to benchmark the current model. The crack position history was available for this experiment. Therefore simulations were carried out by changing α_c and β_c values until a close agreement was achieved between the crack path histories obtained from simulations and experiments. The resulting parameters α_c and β_c thus chosen were 1.0 and 1.5, respectively. The crack paths observed in experiments as well as in simulations are shown in Fig. 7.3. Evidently, the initial kink angle observed is $\sim 8.5^\circ$ in the simulations which compares well with the one ($\sim 10^\circ$) observed in experiments.

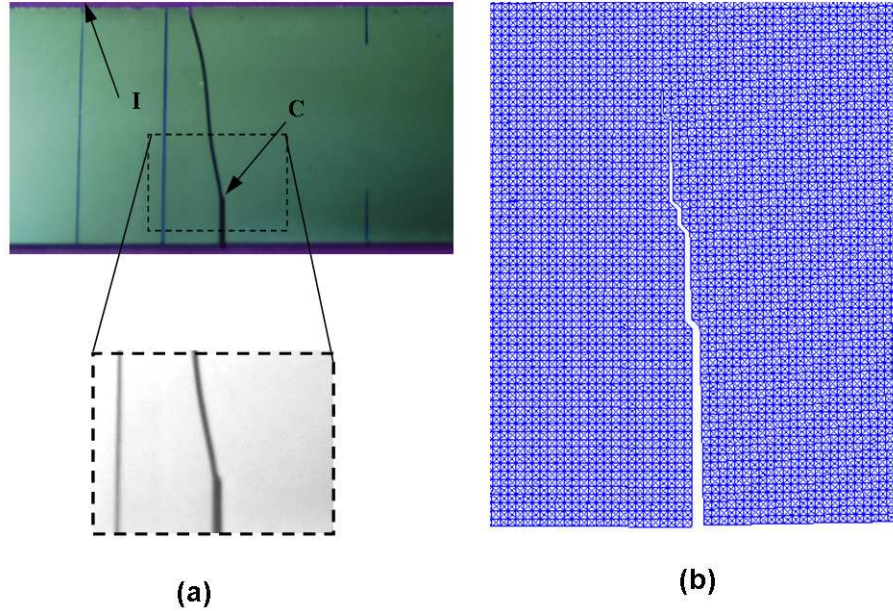


Figure 7.3: Mixed mode dynamic fracture of plexiglas sample. **(a)** Crack path observed in experiments and **(b)** initial crack path from finite element simulations

In this work, the variation of K_{ICR} and E over the sample width was approximated by linear functions. Thus, cohesive element properties for the specimen in Fig. 3.1(a) were

applied in a linearly decreasing fashion as,

$$K_{ICR} = 2.2 - \frac{2.2 - 1.4}{43}X, \quad 0 \leq X \leq 43 \text{ mm} \quad (7.2)$$

and

$$E(X) = 10.0 - \frac{10.0 - 4.0}{43}X, \quad 0 \leq X \leq 43 \text{ mm}. \quad (7.3)$$

The fracture energy and peak cohesive stress were applied as,

$$G_{IC}(X) = \frac{K_{ICR}^2(X)}{E(X)}, \quad T_{max}(X) = \frac{E(X)}{100}. \quad (7.4)$$

The centroidal location of each cohesive element was calculated and the graded cohesive properties were applied according to Eq. 7.4. Similarly, for the other configuration ($E_1 < E_2$) where the crack is situated on the compliant side of the sample, properties were applied using linearly increasing functions.

7.4 Results

The simulations were carried out with material properties applied to continuum and cohesive elements as explained in the previous section. An impact velocity of 5 m/sec was specified to the node located at the impact point.

7.4.1 Energy computations

Additional insight can be gained about the difference in fracture behaviors of the two FGM configurations by studying the evolution of energy during dynamic simulations. At any time instant during the simulation, the total energy needs to be balanced. That is the

sum of all the internal energies need to be equal to the external work done on the system. Mainly three types of energies can be identified here, kinetic energy (U_{KE}), strain energy (U_{SE}) and the energy absorbed by cohesive elements (U_{CE}) which in turn consists of two parts, the energy stored in the cohesive elements and the fracture energy. The external work was computed by multiplying impact load with the load point displacement throughout the history (in the current work, since displacement at the impact point was specified, the resulting nodal force was multiplied by the displacement). Evolution of U_{KE} and U_{SE} are shown in Fig. 7.4(a). A rapid increase in kinetic energy for the case of $E_1 < E_2$ is attributed to the motion of denser material at the upper part of the sample. On a similar note, strain energy is stored rapidly for this case compared to the $E_1 > E_2$ case since stiffer material is located near the impact point. After about 90 μs , for $E_1 < E_2$ (120 μs for $E_1 > E_2$), the stored strain energy is gradually converted into fracture energy. The energy absorbed by the cohesive elements is shown in Fig. 7.4(b). Initially a small portion of the total energy gets stored in the cohesive elements which cause a slow increase of U_{CE} up to 120 μs . A sudden change in the slope of U_{CE} curves at about 125 μs indicates the crack initiation event after which the fracture energy becomes a major portion of U_{CE} . More importantly, it can be observed from this plot that more energy is absorbed throughout the loading history by the cohesive elements for the case of $E_1 < E_2$. This can be directly linked to the higher crack speeds observed in experiments as well as in simulations for this configuration.

7.4.2 Effect of the initial slope of traction-separation law

The cohesive elements are known to introduce artificial compliance [18, 61] into the finite element models and often results in undesirable numerical artifacts. This is especially

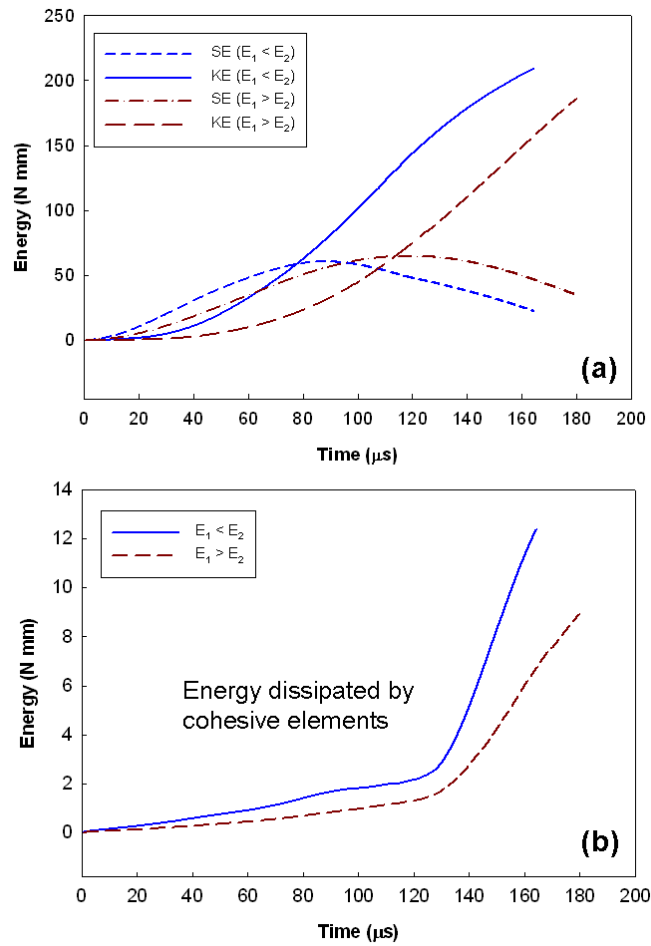


Figure 7.4: Evolution of different energy components in dynamic simulation for both FGM configurations: (a) kinetic energy and strain energy and (b) energy dissipated by cohesive elements

true when a large number of cohesive elements are dispersed in the model as in the current work. In order to realistically simulate the problem on hand, these artifacts have to be minimized. Therefore, a cohesive law having a stiff response initially was required. The initial slope of the traction-separation law can be changed in the bilinear model rather easily and hence it is used in the current work. Simulations were conducted to study the effects of introducing cohesive elements into the model. The geometry considered for this study was same as the one shown in Fig. 7.1(a) except that *it did not have a crack*. Two beam models were created without a crack, first one with cohesive elements (in region 2) and continuum elements (in region 1), as shown in Fig. 7.1(b). The second model had only continuum elements and no cohesive elements. The material properties in each case were $E = 4.2$ GPa, $\nu = 0.34$, $\rho = 1175$ kg/m³ and loaded with an impact velocity of 5 m/sec. Several simulations were conducted (up to 100 μ s after impact) by changing the initial slope of the traction separation law (λ_{cr} in the range 0.05 to 0.005). The crack opening displacement, u_y and stress, σ_y histories (with respect to the coordinate system shown in Fig. 7.1(b)) were collected at a node located at the middle of the bottom edge of the sample from both the models.

The u_y -displacement history is shown in Fig. 7.5(a). For an initial duration of 25 μ s, there are no noticeable displacements because stress waves have not reached the bottom edge of the beam yet. Upon the arrival of stress waves at the bottom edge, u_y monotonically increases up to 100 μ s. From Fig. 7.5(a), it can be seen that the effect of introducing cohesive elements on displacements is relatively small. By comparing u_y values at 100 μ s, a maximum of 4 % difference between models without and with cohesive elements having $\lambda_{cr} = 0.005$ can be noted. The σ_y history is compared between models with and without

cohesive elements in Fig. 7.5(b). The artificial compliance effect, however, can be seen here for larger values of λ_{cr} . For example, when $\lambda_{cr} = 0.05$, the difference in σ_y between the two models is about 16 %. This difference decreases as λ_{cr} is decreased and stress histories for $\lambda_{cr} = 0.005$ are quite close to the model without any cohesive elements. Also it should be noted that there seems to be no significant gain in reducing λ_{cr} beyond 0.01 (the difference in σ_y between the two models is 5.8 % when $\lambda_{cr} = 0.01$ and 4.5 % when $\lambda_{cr} = 0.005$). Therefore a value of $\lambda_{cr} = 0.01$ was selected throughout this work.

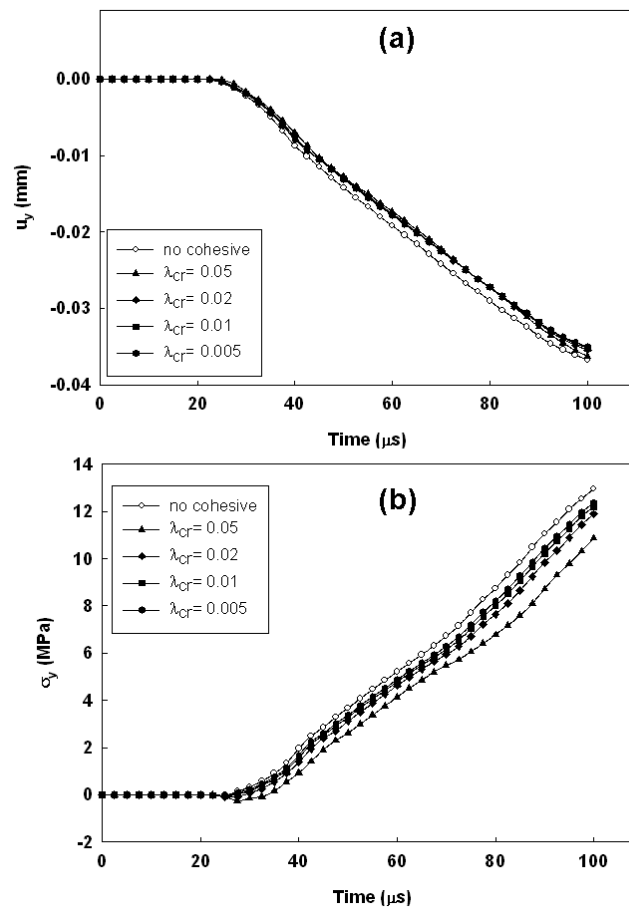


Figure 7.5: Effect of initial slope of the traction-separation law on (a) displacement and (b) on stress results in elastodynamic simulation

7.4.3 Crack path history

Figures 7.6(a) and (c) show snapshots of crack tip normal stress before and after crack initiation, respectively, for the case of a crack on the compliant side ($E_1 < E_2$) of the beam. Similar results for the opposite configuration ($E_1 > E_2$) are shown in Figs. 7.6(b) and (d). The crack initiation times in simulations are nearly same for both the configurations (129 μ s for $E_1 < E_2$ and 130 μ s for $E_1 > E_2$). The similarity in crack paths between the experiments and simulations can be seen for the initial ~ 9 mm of crack growth by comparing figures 7.6(b) with 3.9(a) and 7.6(d) with 3.9(b). When the crack is situated on the compliant side ($E_1 < E_2$) it grows almost like a mode-I crack (crack kink angle α is $\sim 2.4^\circ$ in simulations against 4° in experiments). For the opposite configuration ($E_1 > E_2$), the kink angle α is $\sim 17^\circ$ in simulations and 16° in experiments. It should be noted here that only qualitative comparison of crack path can be made between experiments and simulations because the crack can grow only along element interfaces (in zigzag fashion) in the model. The stress levels are higher at the beginning for $E_1 > E_2$ and they tend to decrease after initiation since crack grows into a progressively compliant region. The opposite trend is observed for the other configuration where lower stresses are seen before crack initiation and they increase after the initiation. Figure 7.7 shows snapshots of crack opening displacements at two time instants, one before and one after the crack initiation. Typical crack opening displacement fields for a mixed-mode problem can be seen from Figs. 7.7(a) and (c). As expected, prior to crack initiation, larger displacements are seen for the case of $E_1 < E_2$ compared to the one with $E_1 > E_2$. Upon comparing Figs 7.7(b) and (d), it can be said that displacements rapidly increase for $E_1 > E_2$ configuration when compared to the $E_1 < E_2$ configuration since the crack grows into a progressively compliant material in the former.

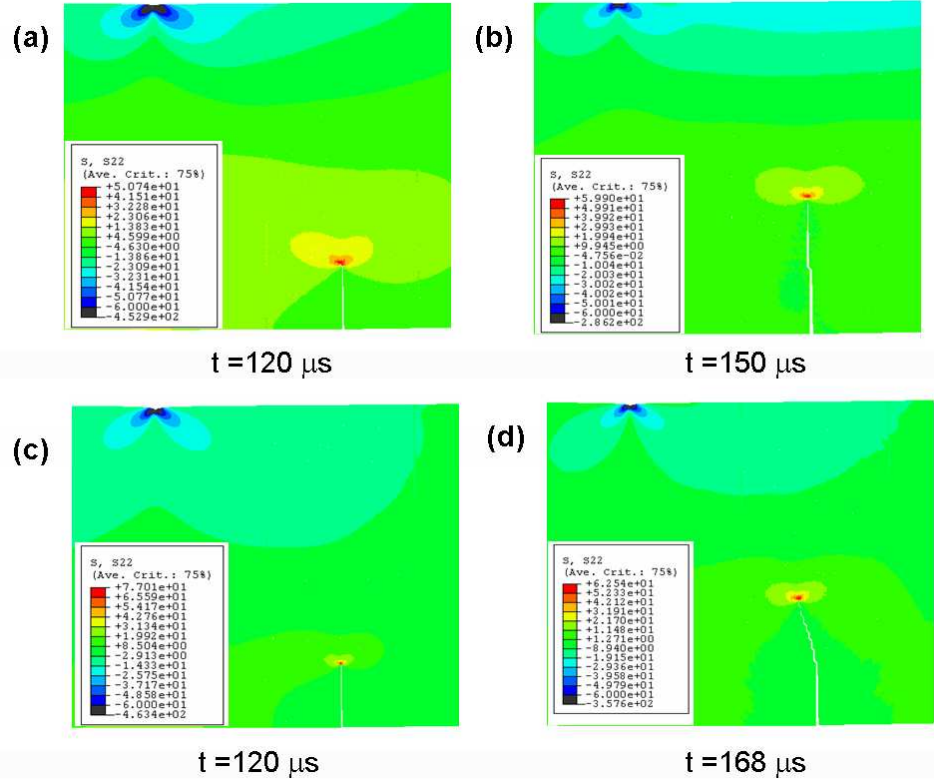


Figure 7.6: Snapshots of σ_{yy} stress field at two different time instants, (a) $120 \mu\text{s}$ and (b) $150 \mu\text{s}$ for $E_1 < E_2$ (crack initiation time = $129 \mu\text{s}$), and (c) $120 \mu\text{s}$ and (d) $168 \mu\text{s}$ for $E_1 > E_2$ (crack initiation time = $130 \mu\text{s}$).

The crack length history from experiments and simulations are plotted in Fig. 7.8(a) and (b) against time $t - t_i$, where t_i is the time at crack initiation. In simulations, the crack initiation takes place at approximately $130 \mu\text{s}$ for both configurations. This is in contrast to the experimental results shown in Fig. 7.8(a) where crack initiation time is in the range $145 \mu\text{s}$ to $155 \mu\text{s}$. This difference is attributed to the fact that in experiments, the initial crack had a finite root radius of $\sim 150 \mu\text{m}$ whereas in finite element simulations, it was modeled as a sharp crack with zero thickness. Therefore, in experiments considerable amount of energy had to accumulate at the notch tip before the crack initiated. Further, the

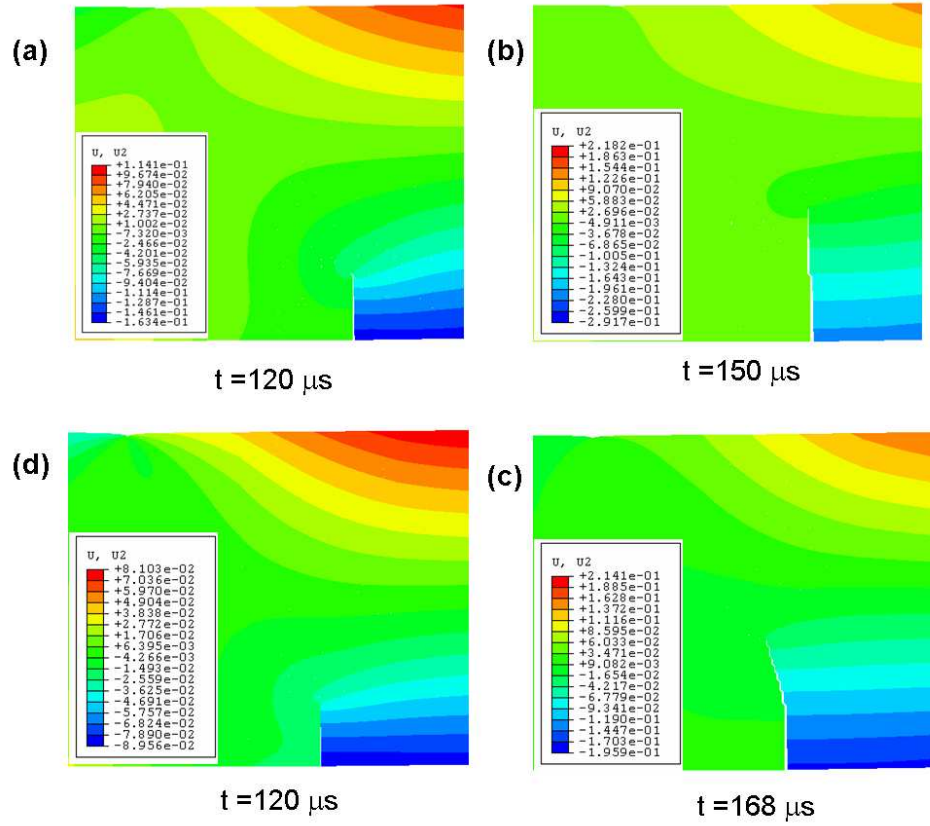


Figure 7.7: Snapshots of u_y displacement field at two different time instants, (a) $120 \mu s$ and (b) $150 \mu s$ for $E_1 < E_2$ (crack initiation time = $129 \mu s$), and (c) $120 \mu s$ and (d) $168 \mu s$ for $E_1 > E_2$ (crack initiation time = $130 \mu s$).

crack propagates at higher speed when it initiates from the compliant side of the sample. This agrees well with the experiments (higher slope for $E_1 < E_2$ in Figs. 7.8(a) and Fig. 7.8(b)). The higher crack speeds lead to greater roughness of the fracture surfaces due to the formation of micro cracks at the main crack tip and hence greater energy dissipation.

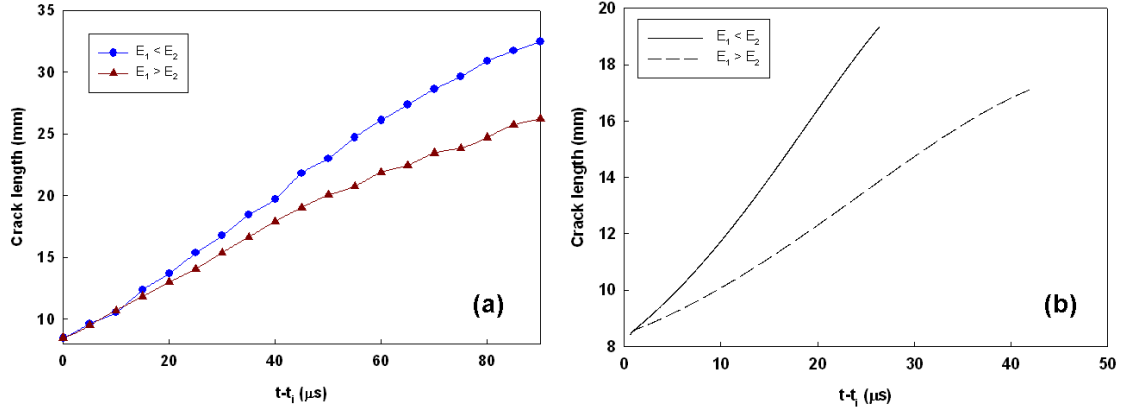


Figure 7.8: Crack growth behavior in FGM sample under mixed-mode loading. Absolute crack length history from (a) experiments and (b) finite element simulations, t_i is crack initiation time ($t_i = 155 \mu\text{s}$ for $E_1 < E_2$ and $145 \mu\text{s}$ for $E_1 > E_2$ in experiments, $t_i \sim 130 \mu\text{s}$ for both $E_1 < E_2$ and $E_1 > E_2$ in simulations).

7.4.4 T -stress history

In order to understand the marked difference in crack paths for the two configurations, a measure of in-plane crack tip constraint, T -stress was computed up to crack initiation. A modified stress difference method [77] was employed where regression of normal stress difference ($\sigma_x - \sigma_y$) ahead of the crack tip was used to find the instantaneous T -stress as

$$(\sigma_x - \sigma_y)_{\theta=0} = T + Dr, \quad (7.5)$$

where D is the higher order coefficient associated with r^1 term in the asymptotic expansion of $(\sigma_x - \sigma_y)$. It can be seen from Fig. 7.9(a) that $(\sigma_x - \sigma_y)$ has an excellent linearity in the range where straight line is fit to the computed data. This process was repeated for all the time steps to get T -stress history of each FGM configurations. The computed T -stress history is plotted in Fig. 7.9(b) up to crack initiation for both configurations. A larger

negative T -stress is observed for the case of $E_1 < E_2$. This indicates that crack is likely to grow in this case in its original direction and has less tendency to kink compared to the other configuration.

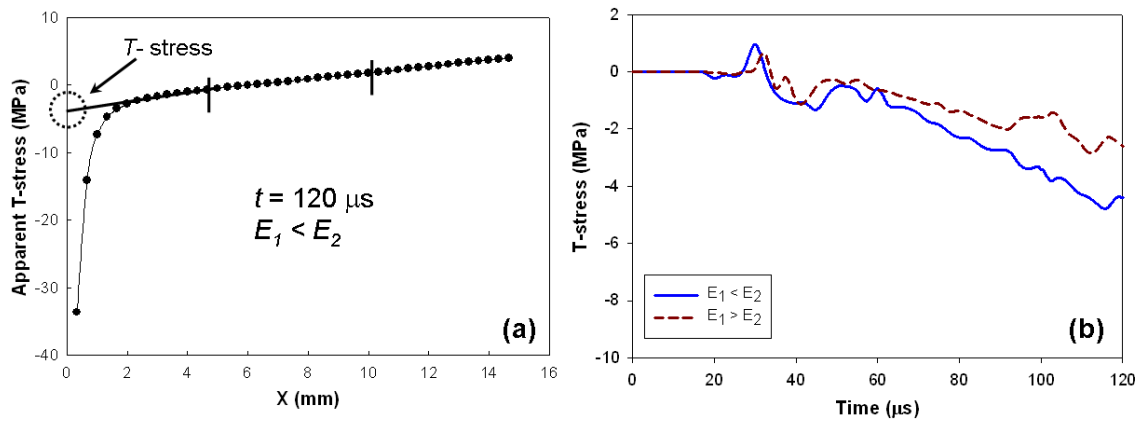


Figure 7.9: (a) Variation of apparent T -stress with crack length at certain time instant before crack initiation (b) T -stress history up to crack initiation for $E_1 < E_2$ and $E_1 > E_2$.

CHAPTER 8

CONCLUSIONS

Mixed-mode dynamic crack propagation in particle filled composites is investigated experimentally and numerically. A Coherent Gradient Sensing (CGS) optical interferometer was used to study mixed-mode dynamic failure of functionally graded materials (FGM). In this technique, the surface slopes (in-plane gradients of out-of-plane displacement) were measured in real-time and fracture parameters were extracted subsequently. A digital image correlation method with high-speed digital imaging technology was also developed to study mixed-mode dynamic failure of syntactic foams. Here, in-plane displacements were measured and strains and fracture parameters were estimated from the measured displacements. Experiments were complemented with finite element simulations of mixed-mode dynamic failure in FGM. Here, a cohesive element formulation was implemented to study formation of new surfaces in nonhomogeneous materials.

In the first part, the optical method of Coherent Gradient Sensing (CGS) was used to investigate the mixed-mode fracture behavior of functionally graded materials. The FGM samples studied were the ones with a continuously varying volume fraction of ceramic filler particles in a polymer matrix having edge cracks initially oriented along the gradient and subjected to impact loading. Mixed-mode loading of the crack was generated by impacting the samples eccentrically relative to the crack plane. The optical method of CGS and high-speed photography were used to map transient crack tip deformations before and after crack initiation. Two configurations, one with a crack on the compliant side of a graded sheet ($E_1 < E_2$) and the second with a crack on the stiff side ($E_1 > E_2$), were

examined experimentally. The differences in both pre- and post-crack initiation behaviors were observed in terms of crack path, crack speed and stress intensity factor histories. Following conclusions were drawn from the study:

- The crack initiates earlier for the case of a crack on the compliant side of the beam ($E_1 < E_2$) compared to the one with a crack on the stiffer side ($E_1 > E_2$). Higher crack speeds were observed in the latter case compared to the former.
- The crack initiation in both the FGM configurations occurred when K_{II} approached values close to zero. Yet, during crack growth K_{II} remained at a small negative value when the crack was on the compliant side but maintained a small positive value when it was on the stiffer side of the FGM sheet. This raises the possibility of a non-zero K_{II} during mixed-mode dynamic crack growth in FGM.
- The crack paths differed significantly for the two FGM configurations studied. That is, the crack kinked less when situated on the compliant side compared to the stiffer side of the FGM sample.
- The initial crack kink angle was predicted for both the configurations using MTS criteria based on the SIF values just prior to crack initiation. Thus predicted crack kink angles agree reasonably well with the observed ones during the early stages of crack growth.

In the second part of this work, the method of digital image correlation was developed to the study of transient deformations such as the one associated with a rapid growth of cracks in materials. Edge cracked polymer beams and syntactic foam samples were studied under low-velocity impact loading conditions. Decorated random speckle patterns in the crack tip

vicinity were recorded using an ultra high-speed digital camera at framing rates of 200,000 frames per second. Two sets of images were recorded, one set before impact and another set after impact. A three-step digital image correlation technique was developed and implemented in a MATLABTM environment for evaluating crack opening/sliding displacements and the associated strains. In the first step, a 2D cross-correlation coefficient was computed to obtain initial estimates of full-field in-plane displacements. In the second step, an iterative technique based on nonlinear least-squares minimization was carried out to refine the estimated displacements from the first step. In the third-step, a regularized restoration smoothing technique, which smoothes the displacements while allowing for discontinuity of displacements across the crack faces was developed and strains were computed.

The current work being the first of its kind using a rotating mirror type multi-channel high-speed digital camera system, calibration tests and procedures were established. A series of benchmark experiments such as intensity variability test, rigid translation and rotation tests were conducted and the accuracy of measured displacements and strains are reported. The accuracy of the measured displacements is in the range 2 to 6 % of a pixel (0.6 to 1.8 μm) and that of dominant strain is about 150 to 300 micro strain.

Using the developed methodology, mode-I dynamic fracture of epoxy and mixed-mode dynamic fracture of syntactic foam samples were studied. The crack opening and sliding displacements and crack tip dominant strain histories from the time of impact upto complete fracture were computed from the speckle images. The crack length and crack speed histories were evaluated. The dynamic stress intensity factors were extracted by performing over-deterministic least-squares analyses on crack opening displacements (in case of mode-I dynamic test) and radial displacement component (in case of mixed-mode dynamic test).

The accuracy of estimated displacements and strains are reported. The mode-mixity history in case of mixed-mode dynamic fracture test and the crack tip T -stress history in case of mode-I dynamic fracture test are also evaluated. The measurements were in very good agreement with companion finite element results. The current approach seems to be a powerful method to investigate dynamic failure events in real time.

In order to understand the marked crack path and other observed differences in fracture parameters between the two FGM configurations from the first part of this research, finite element simulations were undertaken in the last part of this dissertation. An intrinsic cohesive element method with bilinear traction-separation laws were used to model mixed-mode dynamic crack growth. A user subroutine was developed and augmented with ABAQUSTM (Version 6.5) under the ‘user-defined element ’ (UEL) option to implement the cohesive elements. The spatial variation of material properties in continuum elements were incorporated by conducting a thermal analysis and then applying material properties (elastic properties, density and crack initiation toughness) as temperature dependant quantities. The pre-initiation T -stresses were also computed by a modified stress difference method.

The finite element simulations have successfully captured the dominant characteristics of crack kinking under mixed-mode impact loading conditions. The simulated crack paths show a greater kink angle when the crack is on the stiffer side of the FGM. The computed T -stress values prior to crack initiation are more negative when the crack is situated on the compliant side of the sample indicating a greater likelihood of a crack to grow in its original direction and has a lower tendency to kink. Also, as in the experiments, higher crack speeds occur when the crack initiates from the compliant side of the FGM. The computed energy histories reveal greater energy dissipation throughout the observation window by the

cohesive elements for the case of a crack on the compliant side of the FGM. Since higher crack speeds are accompanied by greater fracture surface roughness due to micro-cracking in dynamic fracture events, this observation supports experimental observation of higher crack speed when a crack initiates from the compliant side of the sample.

8.1 Future Directions

The FGM samples used in this research have a shallow gradient (variation in elastic modulus was ~ 2.5 fold 43 mm). The specimens with large material gradients need to be tested experimentally. They are likely to absorb more energy and may delay crack initiation if the initial crack is oriented appropriately with respect to the property gradients). In this work, fracture parameters were extracted for mixed-mode dynamic fracture experiments by measuring transient surface deformations using CGS interferometer. This approach can be extended to a bimaterial systems where the crack is situated close to an interface or the crack running into an interface at an arbitrary angle.

The digital image correlation technique combined with ultra high-speed imaging technology developed in this work promises to be a powerful tool for measuring transient deformations. With the rotating mirror type high-speed digital camera system, displacements as small as 2 to 6% of a pixel have been measured. This can be applied to a number of applications. For example, to understand the dynamic failure characteristics of fiber reinforced composites, cellular materials subjected to stress wave loading, for developing fundamental understanding of nonlinear deformation in rubber like materials subjected to transient loading, to study the damage caused by blast, detonation and shock wave loading in military applications, to name a few.

As a first step, the cohesive element modeling implemented with ABAQUS can be modified to simulate some interesting problems such as interaction of crack with a cylindrical/spherical inclusions. This has great practical applications in understanding toughening mechanisms in particle reinforced composites. As a next step, the cohesive element model can be incorporated with representative volume elements (RVE) for multi-scale modeling of the failure of novel materials such as syntactic foams. The simulation of crack propagation using the current implementation of cohesive element model is computationally intensive. In order to overcome this, an extended finite element method (X-FEM) (which enriches the regular elements selectively with discontinuous shape functions) can be implemented in ABAQUS environment.

BIBLIOGRAPHY

- [1] Kulkarni A., Wang Z., Nakamura T., Sampath S., Goland A., Herman H., Allen J., Ilavsky J., Long G., Frahm J. and Steinbrech R. W. (2003), "Comprehensive microstructural characterization and predictive property modeling of plasma-sprayed zirconia coatings ", *Acta Materialia*; **51**: 2457-2475.
- [2] Kanninen M. F. and Popelar C. H. (1985) *Advanced Fracture Mechanics*, Oxford University Press, New York.
- [3] Hertzberg R. W. (1989) *Deformation and Fracture Mechanics of Engineering Materials*, 3rd Ed. Wiley, New York.
- [4] Freund L. B. (1990) *Dynamic Fracture Mechanics* Cambridge University Press, Cambridge. schen J. W. (1987), "Fracture of non-homogeneous materials ", *International Journal of Fracture*; **34**: 3-22.
- [5] Delale F. Erdogan F. (1983), "The crack problem for a non-homogeneous plane ", *Journal of Applied Mechanics - Transactions of ASME*; **50**:609614.
- [6] Eischen J. W. (1987), "Fracture of non-homogeneous materials ", *International Journal of Fracture*; **34**: 322.
- [7] Jin Z. H. and Batra R. C. (1996), "Some basic fracture mechanics concepts in Functionally graded materials ", *Journal of the Mechanics and Physics of Solids*; **44(8)**: 1221-1235.
- [8] Gu P. and Asaro R. J. (1997), "Cracks in Functionally Graded Materials ", *International Journal of Solids Structures*; **34(1)**: 1-17.
- [9] Konda N. and Erdogan F. (1994), "The mixed-mode crack problem in a nonhomogeneous elastic medium ", *Engineering Fracture Mechanics*; **47(4)**: 533-545.
- [10] Abanto-Bueno J. and Lambros J. (2006), "An experimental study of mixed mode crack initiation and growth in functionally graded materials ", *Experimental Mechanics*; **46(2)**: 179-196.
- [11] Parameswaran V. and Shukla A. (1999), "Crack tip stress fields for dynamic fracture in functionally graded materials ", *Mechanics of Materials*; **31**: 579-596.
- [12] Chalivendra V. and Shukla A. (2005), "Transient Elastodynamic crack growth in functionally graded materials ", *Journal of Applied Mechanics - Transactions of ASME*; **72**: 237-248.

- [13] Jain N., Rousseau C. E. and Shukla A. (2004), "Crack tip stress fields in functionally graded materials with linearly varying properties ", *Theoretical and applied fracture mechanics*; **42**: 155-170.
- [14] Rousseau C. E. and Tippur H. V. (2001), "Influence of elastic gradient profiles on dynamically loaded functionally graded materials: cracks along the gradient ", *International Journal of Solids Structures*; **38**: 7839-7856.
- [15] Rousseau C. E. and Tippur H. V. (2002), "Evaluation of crack tip fields and stress intensity factors in functionally graded elastic materials: Cracks parallel to elastic gradient ", *International Journal of Fracture*; **114**: 87-111.
- [16] Rousseau C. E. and Tippur H. V. (2001) "Dynamic fracture of compositionally graded materials with cracks along the elastic gradient experiments and analysis ", *Mechanics of Materials*; **33**: 403-421.
- [17] Kirugulige M. S., Kitey R. and Tippur H. V. (2004), "Dynamic fracture behavior of model sandwich structures with functionally graded core; a feasibility study ", *Composites Science and Technology*; **65**: 1052-1068
- [18] Wang W. and Nakamura T. (2004), "Simulations of crack propagation in elastic-plastic graded materials ", *Mechanics of Materials*; **36**: 601-622.
- [19] Kim J. H. and Paulino G. H. (2004), "Simulation of crack propagation in functionally graded materials under mixed mode and non-proportional loading ", *International Journal of Mechanics and Materials in Design*; **1**: 63-94.
- [20] Ramaswamy S., Tippur H. V. and Xu L. (1993), "Mixed mode crack tip deformations studies using a modified flexural specimen and Coherent Gradient Sensing ", *Experimental Mechanics*; **33(3)**: pp-218-227.
- [21] Lee H. and Krishnaswamy S. (2000), "Quasi-static propagation of sub interfacial cracks ", *Journal of Applied Mechanics - Transactions of ASME*; **67**: 444-452.
- [22] Mason J. J., Lambros J. and Rosakis A. J. (1992), "The use of a coherent gradient sensor in dynamic mixed-mode fracture mechanics experiments ", *Journal of the Mechanics and Physics of Solids*; **40(3)**: 641-661.
- [23] Prabhu S. and Lambros J. (2000), "A combination optical method of lateral shearing interferometry and Caustics ", *Experimental Mechanics*; **40(4)**: 376-383.
- [24] Butcher R. J., Rousseau C. E. and Tippur H. V. (1998), "A functionally graded particulate composite: Preparation, measurements and failure analysis " *Acta Materialia*; **47(1)**: 259-268.
- [25] Rousseau C. E. and Tippur H. V. (2000), "Compositionally graded materials with cracks normal to the elastic gradient ", *Acta Materialia*; **48**: 4021-4033.

- [26] Marur P. R. and Tippur H. V. (2000), "Dynamic response of bi-material and graded interface cracks under impact loading ", *International Journal of Fracture*; **114**: 87-111.
- [27] de Graaf J. G. A. (1964), "Investigation of brittle fracture in steel by means of ultra high speed photography ", *Applied Optics*; **3(11)**: 1223-1229.
- [28] Dally J. W. (1979), "Dynamic photoelastic studies of fracture ", *Experimental Mechanics*; **19(10)**: 349-361.
- [29] Parameswaran V. and Shukla A. (1998), "Dynamic fracture of functionally gradient materials having discrete property variation ", *Journal of Materials Science*; **33**: 3303-3311.
- [30] Tippur H. V., Krishnaswamy S. and Rosakis A. J. (1991), "Optical Mapping of Crack Tip Deformations using the Methods of Transmission and Reflection Coherent Gradient Sensing: A Study of Crack Tip K-dominance ", *International Journal of Fracture*; **52**: 91-117.
- [31] Kirugulige M. S. and Tippur H. V. (2006), "Mixed mode dynamic crack growth in functionally graded glass filled epoxy ", *Experimental Mechanics*; **46**: 269-281.
- [32] Guo Z. K. and Kobayashi A. S. (1995), "Dynamic mixed mode fracture of concrete ", *International Journal of Solids Structures*; **32(17)**: 2591-2607.
- [33] Flynn E. B., Bassman L. C., Smith T. P., Lalji Z., Fullerton L. H., Leung T. C., Greefield S. R. and Koskelo A. C. (2006), "Three-wavelength ESPI with the Fourier transform method for simultaneous measurement of microstructure scale deformations in three dimensions ", *Applied Optics* **45 (14)**: 3218-3225.
- [34] Fricke-Begemann T. (2003), "Three dimensional deformation field measurement with digital speckle correlation ", *Applied Optics*; **42 (34)**: 6783-6795.
- [35] Feiel R. and Wilksch P. (2000), "High resolution laser speckle correlation for displacement and strain measurement ", *Applied Optics*; **39 (1)**: 54-60.
- [36] Moore A. J., Hand D. P., Barton J. S. and Jones J. D. C. (1999), "Transient deformation measurement with electronic speckle pattern interferometry and a high speed camera ", *Applied Optics*; **38 (7)**: 1159-1162.
- [37] Pedrini G. and Tiziani H. J. (1994), "Double pulse electronic speckle interferometry for vibration analysis ", *Applied Optics*; **33 (34)**: 7857-7863.
- [38] Sirohi R. S., Burke J., Helmers H. and Hinsch K. D. (1997), "Spatial phase shifting or pure in-plane displacement and displacement-derivative measurements in ESPI ", *Applied Optics*; **36(23)**: 5787-5791.

- [39] Duffy D. E. (1972), "Moiré gauging of in-plane displacement using double aperture imaging ", *Applied Optics***11(8)**: 1778-1781.
- [40] Chao Y. J., Luo P. F. and Kalthoff J. F. (1998), "An experimental study of the deformation fields around a propagating crack tip ", *Experimental Mechanics*; **38(2)**: 79-85
- [41] Zhang D., Eggleton C. D. and Arola D. D. (2002), "Evaluating the mechanical behavior of arterial tissues using digital image correlation ", *Experimental Mechanics*; **42(4)**: 409-416.
- [42] Christopher C. B., Jian M. D., Gerard A. A. and Clark T. H. (2002), "An automated approach for direct measurement of two-dimensional strain distributions within articular cartilage under unconfined compression ", *Journal of Biomedical Engineering*; **24**: 557-567.
- [43] Li E. B., Tieu A.K. and Yuen W. Y. D. (2003), "Application of digital image correlation technique to dynamic measurement of the velocity field in the deformation zone in cold rolling ", *Optics and Lasers in Engineering*; **39**: 479-488.
- [44] Jean N. P., Sylain C., Christophe C. and Francois H. (2002), "Analysis of multiaxial test on a C/C composite by using digital image correlation and a damage model ", *Experimental Mechanics*; **42(3)**: 318-328.
- [45] Peters W. H. and Ranson W. F. (1982), "Digital image techniques in experimental stress analysis ", *Optical Engineering*; **21**: 427-431.
- [46] Sutton M. A., Cheng M., Peters W. H, Chao Y. J and McNeil S. R. (1986), "Application of an optimized digital correlation method to planar deformation analysis ", *Image and Vision Computing*; **4(3)**: 133-150.
- [47] Bruck H. A., McNeill S. R., Sutton M. A. and Peters W. H. (1989), "Digital image correlation using Newton-Raphson method of partial differential correction ", *Experimental Mechanics*; **29**: 261-267.
- [48] Chen D. J. and Chiang F. P., Tan Y. S. and Don H. S. (1993), "Digital speckle-displacement measurement using a complex spectrum method ", *Applied Optics*; **32(11)**: 1939-1849.
- [49] Lou P.F., Chao Y.J., Sutton M.A. and Peters W.H. (1993), "Accurate measurement of three-dimensional deformations in deformable and rigid bodies using computer vision ", *Experimental Mechanics*; **33(3)**: 123-132.
- [50] Helm, J. D., McNeill, S. R. and Sutton, M. A. (1996), "Improved three-dimensional image correlation for surface displacement measurement ", *Optical Engineering*; **35(7)**: 1911-1920.

- [51] Bittencourt T. N., Wawrzynek P. A., Ingraffea A. R. and Sousa J. L. (1996), "Quasi-automatic simulation of crack propagation for 2D LEFM problem ", *Engineering Fracture Mechanics*; **55(2)**: 321-334.
- [52] Nishioka T. (1997), "Computational dynamic fracture mechanics ", *International Journal of Fracture*; **86**: 127-159.
- [53] Nishioka T., Tokudome H. and Kinoshita M. (2001), "Dynamic fracture path prediction in impact fracture phenomena using moving finite element method based on Delaunay automatic mesh generation ", *International Journal of Solids Structures*; **38**: 5273-5301.
- [54] Tilbrook M. T., Moon R. J. and Hoffman M. (2005), Finite element simulations of crack propagation in functionally graded materials under flexural loading ", *Engineering Fracture Mechanics*; **72**: 2444-2467.
- [55] Dugdale D. C. (1960), "Yielding of steel sheets containing slits ", *Journal of the Mechanics and Physics of Solids*; **8**: 100-104.
- [56] Barenblatt G. I. (1962), "The mathematical theory of equilibrium cracks in brittle fracture ", *Advances of applied mechanics*; **7**: 55-129.
- [57] Needleman A. (1987), "A continuum model for void nucleation by inclusion debonding ", *Journal of Applied Mechanics - Transactions of ASME*; **54**: 525-531.
- [58] Xu X. P. and Needleman A. (1994), "Numerical simulations of fast crack growth in brittle solids ", *Journal of the Mechanics and Physics of Solids*; **42(9)**: 1397-1434.
- [59] Geubelle P. H. and Baylor J. S. (1998), "Impact induced delamination of composites: a 2D simulation ", *Composites Part B Engineering*; **29**: 589-602.
- [60] Zavattieri P. D., Raghuram P. V. and Espinosa H. D. (2001), "A computational model of ceramic microstructures subjected to multi-axial dynamic loading ", *Journal of the Mechanics and Physics of Solids*; **49**: 27-68.
- [61] Zhang Z. and Paulino G. H. (2005), "Cohesive zone modeling of dynamic failure in homogeneous and functionally graded materials ", *International journal of plasticity*; **21**: 1195-1254.
- [62] Tvergaard V. and Hutchinson J. W. (1994), "The relation between crack growth resistance and fracture process parameters in elastic-plastic solids ", *Journal of the Mechanics and Physics of Solids*; **40**: 1377-1397.
- [63] Madhusudhana K. S. and Narasimhan R. (2002), "Experimental and numerical investigations of mixed-mode crack growth resistance of a ductile adhesive joint ", *Engineering Fracture Mechanics*; **69**: 865-883.

- [64] Geubelle P. H. and Rice J. R. (1995), “A spectral method for three-dimensional elastodynamic fracture problems ”, *Journal of the Mechanics and Physics of Solids*; **43(11)**: 1791-1824.
- [65] Camacho G. T. and Ortiz M. (1996), “Computational modeling of impact damage in brittle materials ”, *International Journal of Solids Structures*; **33(20-22)**: 2899-2938.
- [66] Ortiz M. and Pandolfi A. (1999), “Finite-deformation irreversible cohesive elements for three dimensional crack propagation analysis ”, *International Journal for Numerical Methods in Engineering*; **44**: 1267-1282.
- [67] Ruiz G., Pandolfi A. and Ortiz M. (2001), “Three-dimensional cohesive modeling of dynamic mixed mode fracture ”, *International Journal for Numerical Methods in Engineering*; **52**: 97-120.
- [68] Belytschko T. and Black A. T. (1999), “Elastic crack growth in finite elements with minimal re-meshing ”, *International Journal for Numerical Methods in Engineering*; **45**: 601-620.
- [69] Moes N. and Belytschko T. (2002), “Extended finite elements for cohesive crack growth ”, *Engineering Fracture Mechanics*; **69**: 813-833.
- [70] Rabczuk T. and Belytschko T. (2004), “Cracking particles: a simplified meshfree method for arbitrary evolving cracks ”, *International Journal for Numerical Methods in Engineering*; **61**: 2316-2343.
- [71] Tippur H. V., Krishnaswamy S. and Rosakis A. J. (1992), “Measurement of transient crack tip deformation fields using the method of coherent gradient sensing, K -dominance ”, *Journal of the Mechanics and Physics of Solids*; **40(2)**: 339-372.
- [72] Williams M. L. (1959), *Journal of Applied Mechanics - Transactions of ASME*; **24**: 109-114.
- [73] Sanford R. J. (1989), “Determining Fracture parameters with full-field optical methods ”, *Experimental Mechanics*; **29**: 241-247.
- [74] Freund L. B. and Rosakis A. J. (1992), “The structure of the near-tip field during transient elastodynamic crack growth ” *Journal of the Mechanics and Physics of Solids*; **40(3)**: 699-719.
- [75] Rousseau C. E. (2005), “Critical examination of the use coherent gradient sensing in measuring fracture parameters in functionally graded materials ”, *Journal of Composite Materials*; **40(19)**: 1763.
- [76] Dally J. W. and Sanford R. J. (1987), “Strain gage methods for measuring the opening mode stress intensity factor, K_I ”, *Experimental Mechanics*; **49**: 381-388.

- [77] Maleski M. J., Kirugulige M. S. and Tippur H. V. (2004), “A method for measuring mode-I crack tip constraint under static and dynamic loading conditions ”, *Experimental Mechanics*; **44(5)**: 522-532.
- [78] Erdogan F. and Sih G. C. (1963), “On the crack extension in plates under plane loading and transverse shear ”, *Journal of basic engineering-transactions of the ASME*; **85D(4)**: 519-525.
- [79] Matlab 7.0, The MathWorks, Inc. (2006), (<http://www.mathworks.com>)
- [80] Broyden C. G. (1970), “The convergence of a class of double-rank minimization algorithms ”, *Journal of Inst. Maths. Applics*; 76-90
- [81] Reinsch C. H. (1967), “Smoothing by spline functions ”, *Numerische Mathematik*; **10**: 177-183.
- [82] Craven P. and Grace Wahba (1979), “Smoothing noisy data with spline functions: Estimating the correct degree of smoothing by the method of generalized cross validation ”, *Numerische. Mathematik*; **31**: 377-405.
- [83] Rafael C. Gonzalez, Richard E. Woods and Steven L. Eddins (2004), *Digital image processing using MATLAB*, 1st Edition; Prentice Hall, NJ.
- [84] Lewis J. P. (1995), “Fast template matching ”, *Vision Interface*; **10**: 120-123.
- [85] Nishioka T. and Atluri S. N. (1983), “Path independent integrals, energy release rates, and general solutions of near-tip fields in mixed-mode dynamic fracture mechanics ”, *Engineering Fracture Mechanics*; **18(1)**: 1-22.
- [86] Yoneyama S., Morimoto Y. and Takashi M. (2006), “Automatic evaluation of mixed-mode stress intensity factors utilizing digital image correlation ”, *Strain*; **42(1)**: 21-29.
- [87] Dally J. W. and Riley W. F. (2005), *Experimental Stress Analysis*, 4th Ed, College House Enterprises, LLC.
- [88] Jayadevan K., Narasimhan R., Ramamurthy T. and Dattaguru B. (2001), “A numerical study in dynamically loaded fracture specimens ”, *International Journal of Solids Structures*; **38(5)**: 4987-5005.
- [89] Robert D. Cook, David S. Malkus and Michael E. Plesha (1988) *Concepts and applications of finite element analysis*, John Wiley and Sons, New York.
- [90] Hilber H. M., Hughes T. J. R. and Taylor R. L. (1978), “Collocation, dissipation and overshoot for time integration schemes in structural dynamics ”, *Earthquake engineering and structural dynamics*; **6**: 99-117.

- [91] ABAQUS Version 6.5 (2004), “Theory and users manuals ”, Hibbit, Karlsson and Sorenson, RI, USA.
- [92] Rene Kregting (2005), “Cohesive zone models: towards a robust implementation of irreversible behavior ”, Philips Applied Technologies.
- [93] Giannakopoulos A. E. and Suresh S. (1997), “Indentation of solids with gradients in elastic properties: Part-I. Point force ”, *International Journal of Solids Structures*; **34**: 2357-2392
- [94] Rice J. R. (1968), “Mathematical analysis in the mechanics of fracture ”, *Ed. H. Liebowitz, Fracture, an advanced treatise*; **vol 2**: Academic Press, New York pp 191-311.
- [95] Anlas G., Santare M. H. and Lambros J. (2000), “Numerical calculation of stress intensity factors in functionally graded materials ”, *International Journal of Fracture*; **104**: 131-143.
- [96] Kim J. H and Paulino G. H. (2002), “Isoparametric graded finite elements for non-homogeneous isotropic and orthotropic materials ”, *Journal of Applied Mechanics - Transactions of ASME*; **69**: 502-514.

APPENDIX A

A NOTE ON ACCURACY OF STRAINS AND TIME RESOLVED DISPLACEMENTS

A.1 A note on accuracy of strains

Since the materials tested using DIC in the current work are epoxy and syntactic foam made from glass microballoons with epoxy matrix, strains observed in the crack tip vicinity were relatively small and elastic. The strains presented here were obtained by differentiating displacements estimated from DIC. Therefore greater errors in the strains when compared to displacements are to be expected. It has been shown in Section 4.5.2 that the accuracy of displacements is in the range of 2 to 6% of a pixel. The accuracy of strains can be estimated by conducting benchmark tests at different stages/levels, as discussed below. The central requirement of these tests is to generate a known constant strain for the entire image and then try to estimate it using the computational methodology:

- Generate a synthetic image mathematically (speckle image can be generated by adding random noise of zero mean and a constant variance to a uniform image). Then apply a known strain to this image mathematically and measure the same using the image correlation program.
- Acquire an image of a speckle pattern, then deform it mathematically by applying uniform strain and estimate the same.
- Acquire two images back to back without any deformation between them and then deform one of the images mathematically and estimate the strains between them.

- Acquire an image, subject the sample to a uniform mechanical load to impart a constant strain and then estimate that strain.

Out of these four possible approaches, the results of (a) will be highly accurate but may not be realistic as it cannot be achieved in practice. Even the accuracy of results in (b) is seldom achieved because the random errors associated while acquiring an image, twice by a CCD camera, are not modeled in such an exercise. The exercise of type (d) takes all experimental errors into account but the results will depend on the characteristics of the mechanical device used as well as inherent experimental complexities due to rotation of the sample, slip in the grips, etc. Considering all the above, benchmark test of type (c) is proposed to assess the accuracy of strains in the current work.

Two images of a random speckle pattern were recorded back to back without any deformation. The full-field (horizontal) displacement data between these two images is presented in Fig. A.1(a) which has a mean of 0.039 pixels and a standard deviation of 0.0015 pixels (Ideally, these values should be all zeros). One of these images is mathematically stretched by imposing a strain of 2500 $\mu\epsilon$ in the horizontal direction and the displacements were extracted. The resulting linearly varying u -displacement field can be seen from Fig. A.1(b). This displacement was smoothed using the restoration method explained in Section 4.1.3 and normal strain ϵ_{xx} was computed. The smoothed displacement field is shown in Fig. A.1(c) and the strain plot is shown in Fig. A.1(d). It can be seen from Fig. A.1(d) that ϵ_{xx} oscillates about 2500 $\mu\epsilon$ and has a standard deviation of about 142 $\mu\epsilon$. Thus it can be said that the strains estimated in this work have errors approximately equal to 142 $\mu\epsilon$.

A.2 Time resolved displacements

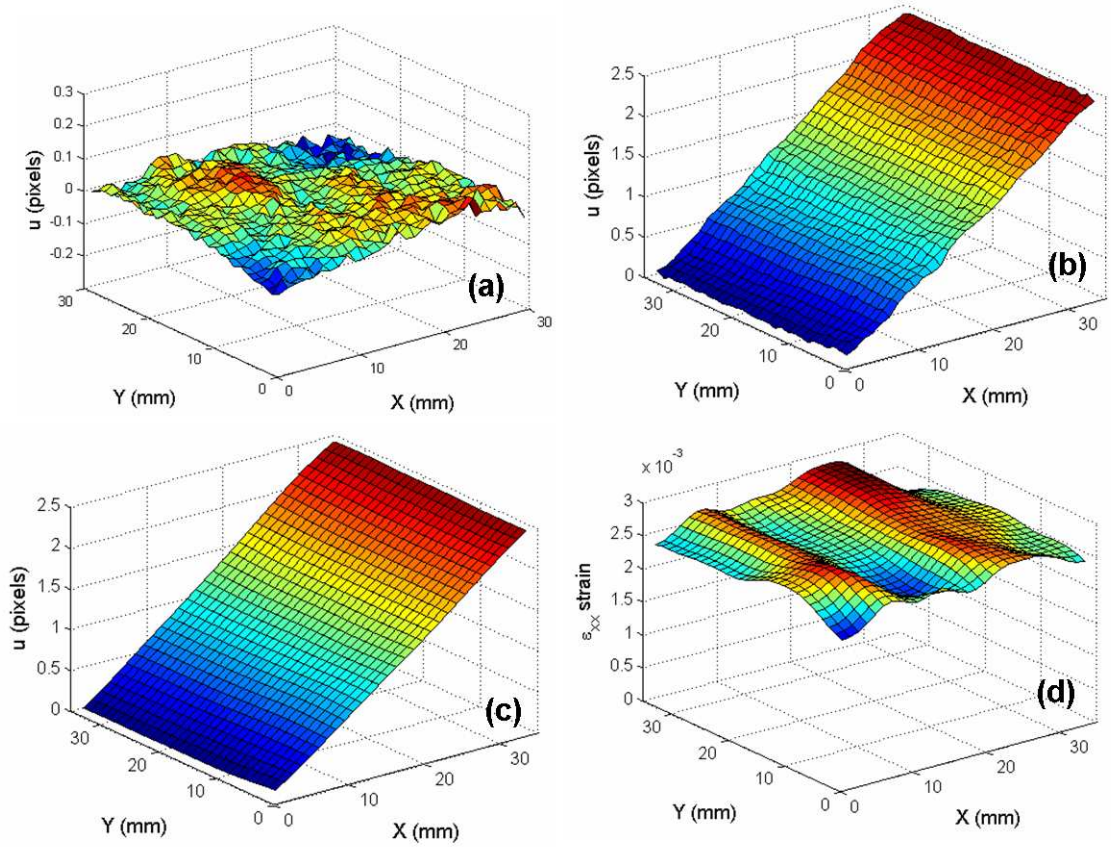


Figure A.1: Results of benchmark experiment conducted to estimate the accuracy of displacements and strains. **(a)** full-field u -displacement between image 1 and image 2 before deforming image 2 (ideally u -displacement should be zero). **(b)** u -displacement after applying a constant strain to image 2 but before smoothing, **(c)** u -displacement after smoothing and **(d)** normal strain after stretching image 2 uniformly.

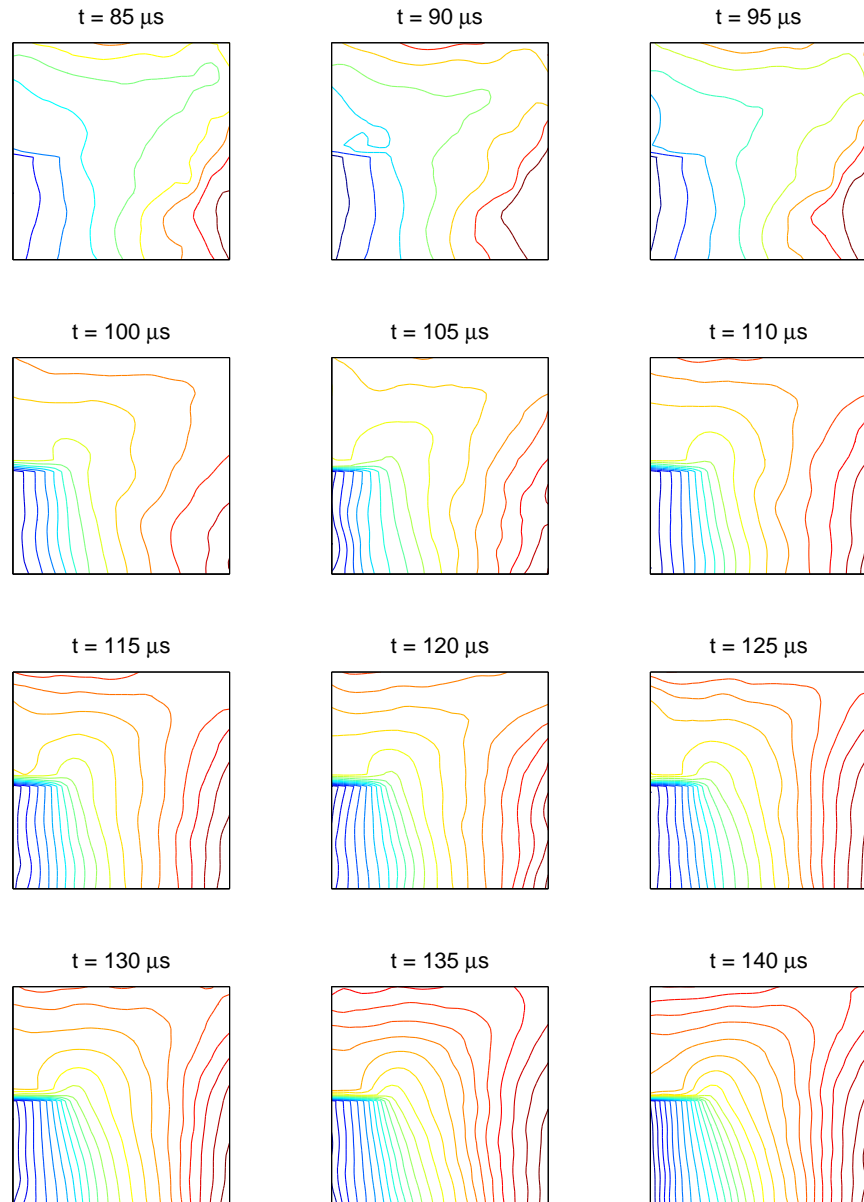


Figure A.2: Time resolved crack opening displacements for image # 1 to 12. Time at which each image was acquired after impact, is indicated above each figure. The interval between each contour is $3.5 \mu\text{m}$.

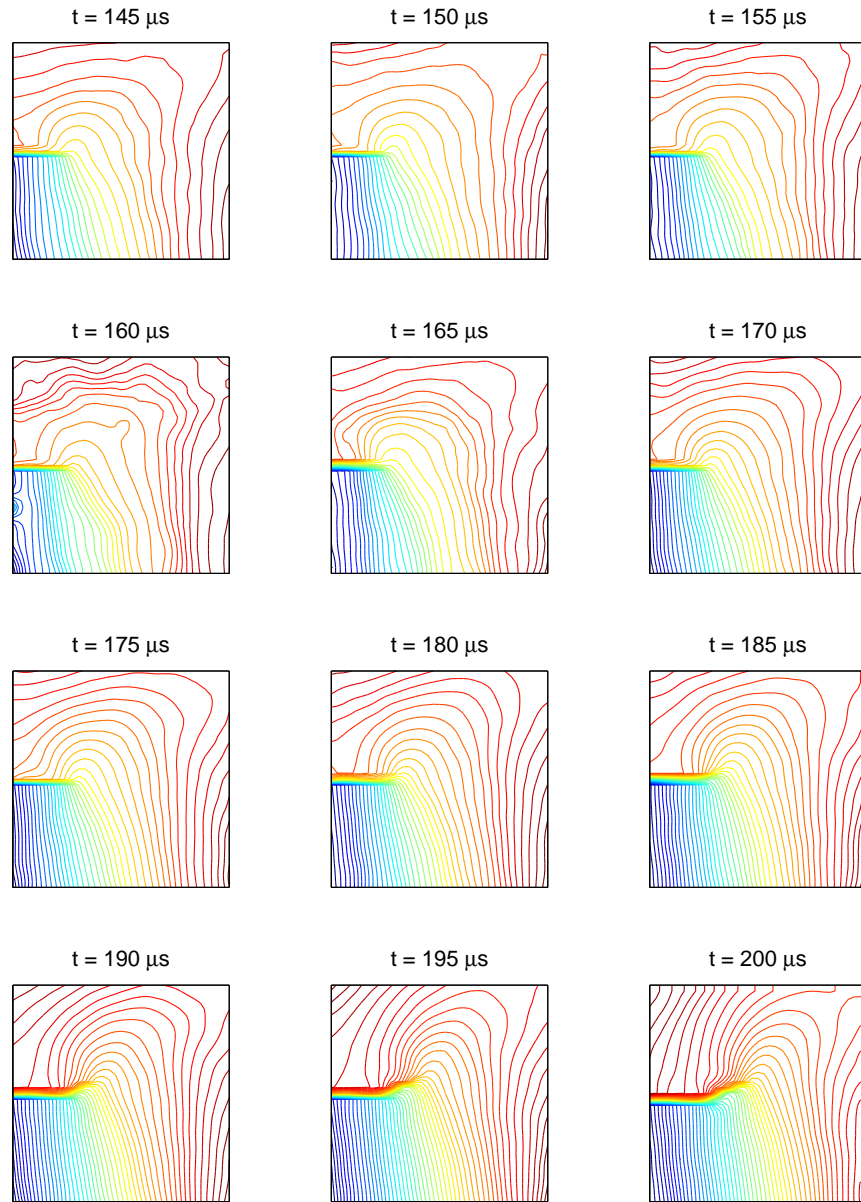


Figure A.3: Time resolved crack opening displacements for image # 13 to 24. Time at which each image was acquired after impact, is indicated above each figure. The interval between each contour is $3.5 \mu\text{m}$.

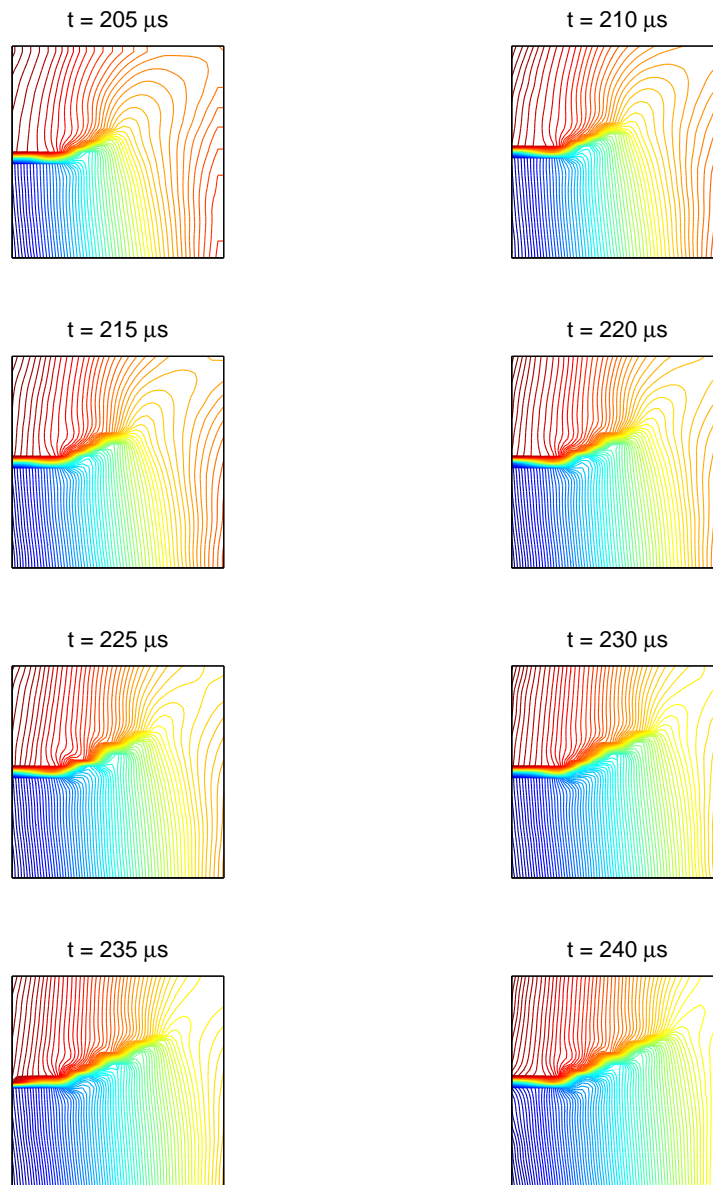


Figure A.4: Time resolved crack opening displacements for mixed-mode dynamic test, image # 25 to 32. Time at which each image was acquired after the impact, is indicated above each figure. The interval between each contour is $3.5 \mu\text{m}$.

APPENDIX B

COMPUTATION OF STIFFNESS COEFFICIENTS IN TRACTION-SEPARATION LAWS

B.1 Exponential traction-separation law

While deriving expressions for stiffness coefficients, the history dependency needs to be taken into account. Referring to Fig. B.1, if the history dependency is not taken into account and if there is an unloading at point 'C', then the same traction curve is followed as during the loading. This implies that to achieve unloading, traction need to be increased which is not realistic. Therefore unloading path should be linear leading to the origin as shown in broken line in Fig. B.1. This means that the stiffness matrix need to be different for loading and unloading part of the traction-separation curve. Thus defining the effective separation parameter, λ as,

$$\lambda = \sqrt{\left(\frac{\Delta_n}{\delta_n}\right)^2 + \beta_c^2 \left(\frac{\Delta_t}{\delta_t}\right)^2} \quad (\text{B.1})$$

with $\beta_c = (0, \infty)$. In the current work, history dependency is taken care by defining a single history dependent damage parameter λ_{max} as,

$$\lambda_{max} = \max\{\lambda(\tau) \mid 0 \leq \tau \leq t\} \quad (\text{B.2})$$

Loading is said to occur when $\lambda = \lambda_{max}$ and $\dot{\lambda} \geq 0$, and unloading/reloading when $\lambda < \lambda_{max}$. Stiffness coefficients for loading are obtained by differentiating Eqs. 6.25 and 6.26 with respect to Δ_n and Δ_t

$$SS_{11} = \frac{\partial T_t}{\partial \Delta_t} = 2 \frac{\phi_n}{\delta_t^2} e^{\left(-\frac{\Delta_n}{\delta_n}\right)} \left[q + \left\{ \frac{r-q}{r-1} \right\} \frac{\Delta_n}{\delta_n} \right] \left[1 - \frac{2\Delta_t^2}{\delta_t^2} \right] e^{\left(-\frac{\Delta_t^2}{\delta_t^2}\right)}, \quad (\text{B.3})$$

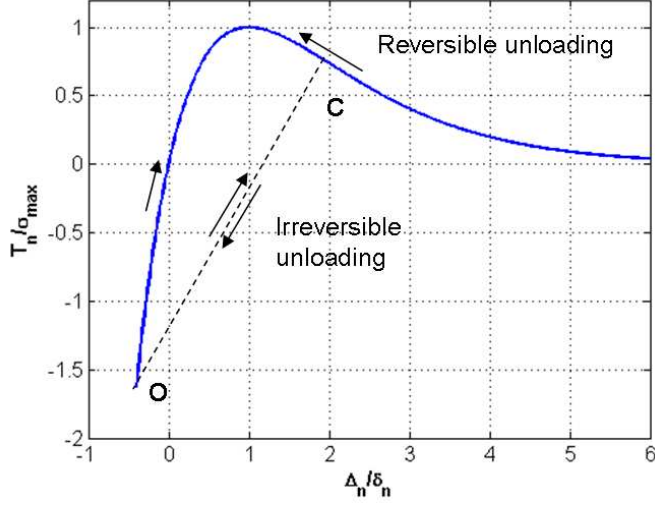


Figure B.1: Reversible and irreversible unloading

$$SS_{12} = \frac{\partial T_t}{\partial \Delta_n} = 2 \frac{\phi_n}{\delta_t^2} \frac{\Delta_t}{\delta_n} e^{-\frac{\Delta_n}{\delta_n}} e^{-\frac{\Delta_t^2}{\delta_t^2}} \left[\left\{ \frac{r-q}{r-1} \right\} \left\{ 1 - \frac{\Delta_n}{\delta_n} \right\} - q \right], \quad (\text{B.4})$$

$$SS_{21} = \frac{\partial T_n}{\partial \Delta_t} = 2 \frac{\phi_n}{\delta_t^2} \frac{\Delta_t}{\delta_n} e^{-\frac{\Delta_n}{\delta_n}} e^{-\frac{\Delta_t^2}{\delta_t^2}} \left[\left\{ \frac{1-q}{r-1} \right\} \left\{ 1 - \frac{\Delta_n}{\delta_n} \right\} - \frac{\Delta_n}{\delta_n} \right]. \quad (\text{B.5})$$

$$SS_{22} = \frac{\partial T_n}{\partial \Delta_n} = \frac{\phi_n}{\delta_n} e^{-\frac{\Delta_n}{\delta_n}} \left[\left\{ \frac{1}{\delta_n} - \frac{\Delta_n}{\delta_n^2} \right\} e^{-\frac{\Delta_t^2}{\delta_t^2}} + \left\{ \frac{1-q}{r-1} \right\} \left\{ 1 - e^{-\frac{\Delta_t^2}{\delta_t^2}} \right\} \left\{ \frac{\delta_n}{\delta_n^2} - \frac{1}{\delta_n} - \frac{r}{\delta_n} \right\} \right]. \quad (\text{B.6})$$

The unloading stiffness matrix is calculated as follows. The separations Δ_n and Δ_t are first scaled by a factor λ_{max}/λ , the tractions associated with these scaled separations are computed, and these tractions are scaled back by multiplying them by λ/λ_{max} [92]. Thus,

$$T_n^u = \frac{\lambda}{\lambda_{max}} T_n \left(\frac{\lambda_{max}}{\lambda} \Delta_n, \frac{\lambda_{max}}{\lambda} \Delta_t \right) = \frac{\lambda}{\lambda_{max}} T_n(\Delta_n^*, \Delta_t^*), \quad (\text{B.7})$$

$$T_t^u = \frac{\lambda}{\lambda_{max}} T_t \left(\frac{\lambda_{max}}{\lambda} \Delta_n, \frac{\lambda_{max}}{\lambda} \Delta_t \right) = \frac{\lambda}{\lambda_{max}} T_t(\Delta_n^*, \Delta_t^*). \quad (\text{B.8})$$

where

$$\Delta_n^* = \frac{\lambda_{max}}{\lambda} \Delta_n, \quad \Delta_t^* = \frac{\lambda_{max}}{\lambda} \Delta_t. \quad (\text{B.9})$$

In the above, T_n^u and T_t^u are unloading tractions in normal and tangential directions respectively. The variation of λ is required in order to differentiate T_n^u and T_t^u which is given as,

$$\begin{aligned} \lambda^2 &= \left(\frac{\Delta_n}{\delta_n} \right)^2 + \beta_c^2 \left(\frac{\Delta_t}{\delta_t} \right)^2 \\ 2\lambda\delta\lambda &= \frac{2\Delta_n}{\delta_n^2} \delta\Delta_n + \frac{2\beta_c^2 \Delta_t}{\delta_t^2} \delta\Delta_t \\ \delta\lambda &= \frac{\Delta_n}{\lambda\delta_n^2} \delta\Delta_n + \frac{\beta_c^2 \Delta_t}{\lambda\delta_t^2} \delta\Delta_t \end{aligned} \quad (\text{B.10})$$

The variation of traction in normal direction is given by,

$$\begin{aligned} \delta(T_n^u) &= \frac{1}{\lambda_{max}} T_n(\Delta_n^*, \Delta_t^*) \delta\lambda + \frac{\lambda}{\lambda_{max}} \delta[T_n(\Delta_n^*, \Delta_t^*)] \\ &= \frac{1}{\lambda_{max}} T_n \delta\lambda + \frac{\lambda}{\lambda_{max}} \left(\frac{\partial T_n}{\partial \Delta_n^*} \delta\Delta_n^* + \frac{\partial T_n}{\partial \Delta_t^*} \delta\Delta_t^* \right) \\ &= \frac{1}{\lambda_{max}} T_n \delta\lambda + \frac{\lambda}{\lambda_{max}} \left[\frac{\partial T_n}{\partial \Delta_n^*} \left\{ \frac{\lambda_{max}}{\lambda} \delta\Delta_n - \frac{\lambda_{max} \Delta_n}{\lambda^2} \delta\lambda \right\} \right. \\ &\quad \left. + \frac{\lambda}{\lambda_{max}} \left[\frac{\partial T_n}{\partial \Delta_t^*} \left\{ \frac{\lambda_{max}}{\lambda} \delta\Delta_t - \frac{\lambda_{max} \Delta_t}{\lambda^2} \delta\lambda \right\} \right] \right]. \end{aligned} \quad (\text{B.11})$$

Substituting for $\delta\lambda$ and simplifying we get,

$$\begin{aligned} \delta(T_n^u) &= \left[\frac{T_n \Delta_n}{\lambda_{max} \lambda \delta_n^2} + \left(1 - \frac{\Delta_n^2}{\lambda^2 \delta_n^2} \right) \frac{\partial T_n}{\partial \Delta_n^*} - \frac{\Delta_n \Delta_t}{\lambda^2 \delta_n^2} \frac{\partial T_n}{\partial \Delta_t^*} \right] \delta\Delta_n \\ &\quad + \left[\frac{\beta_c^2 T_n \Delta_t}{\lambda_{max} \lambda \delta_t^2} + \left(1 - \frac{\beta_c^2 \Delta_t^2}{\lambda^2 \delta_t^2} \right) \frac{\partial T_n}{\partial \Delta_n^*} - \frac{\beta_c^2 \Delta_n \Delta_t}{\lambda^2 \delta_t^2} \frac{\partial T_n}{\partial \Delta_t^*} \right] \delta\Delta_t. \end{aligned} \quad (\text{B.12})$$

Similarly the variation of traction in tangential direction can be simplified to,

$$\begin{aligned} \delta(T_t^u) = & \left[\frac{T_t \Delta_n}{\lambda_{max} \lambda \delta_n^2} + \left(1 - \frac{\Delta_n^2}{\lambda^2 \delta_n^2} \right) \frac{\partial T_t}{\partial \Delta_n^*} - \frac{\Delta_n \Delta_t}{\lambda^2 \delta_n^2} \frac{\partial T_t}{\partial \Delta_t^*} \right] \delta \Delta_n \\ & + \left[\frac{\beta_c^2 T_t \Delta_t}{\lambda_{max} \lambda \delta_t^2} + \left(1 - \frac{\beta_c^2 \Delta_t^2}{\lambda^2 \delta_t^2} \right) \frac{\partial T_t}{\partial \Delta_t^*} - \frac{\beta_c^2 \Delta_n \Delta_t}{\lambda^2 \delta_t^2} \frac{\partial T_t}{\partial \Delta_n^*} \right] \delta \Delta_t. \end{aligned} \quad (\text{B.13})$$

Finally the stiffness coefficients for unloading are given by [92],

$$SS_{11}^u = \frac{\delta T_t^u}{\delta \Delta_t} = \left[\frac{\beta_c^2 T_t \Delta_t}{\lambda_{max} \lambda \delta_t^2} + \left(1 - \frac{\beta_c^2 \Delta_t^2}{\lambda^2 \delta_t^2} \right) \frac{\partial T_t}{\partial \Delta_t^*} - \frac{\beta_c^2 \Delta_n \Delta_t}{\lambda^2 \delta_t^2} \frac{\partial T_t}{\partial \Delta_n^*} \right], \quad (\text{B.14})$$

$$SS_{12}^u = \frac{\delta T_t^u}{\delta \Delta_n} = \left[\frac{T_t \Delta_n}{\lambda_{max} \lambda \delta_n^2} + \left(1 - \frac{\Delta_n^2}{\lambda^2 \delta_n^2} \right) \frac{\partial T_t}{\partial \Delta_n^*} - \frac{\Delta_n \Delta_t}{\lambda^2 \delta_n^2} \frac{\partial T_t}{\partial \Delta_t^*} \right], \quad (\text{B.15})$$

$$SS_{21}^u = \frac{\delta T_n^u}{\delta \Delta_t} = \left[\frac{\beta_c^2 T_n \Delta_t}{\lambda_{max} \lambda \delta_t^2} + \left(1 - \frac{\beta_c^2 \Delta_t^2}{\lambda^2 \delta_t^2} \right) \frac{\partial T_n}{\partial \Delta_t^*} - \frac{\beta_c^2 \Delta_n \Delta_t}{\lambda^2 \delta_t^2} \frac{\partial T_n}{\partial \Delta_n^*} \right], \quad (\text{B.16})$$

$$SS_{22}^u = \frac{\delta T_n^u}{\delta \Delta_n} = \left[\frac{T_n \Delta_n}{\lambda_{max} \lambda \delta_n^2} + \left(1 - \frac{\Delta_n^2}{\lambda^2 \delta_n^2} \right) \frac{\partial T_n}{\partial \Delta_n^*} - \frac{\Delta_n \Delta_t}{\lambda^2 \delta_n^2} \frac{\partial T_n}{\partial \Delta_t^*} \right]. \quad (\text{B.17})$$

B.2 Bilinear traction-separation law

Stiffness coefficients can be calculated by differentiating the tractions with respect to separations from Eq. 6.30 through 6.33. For loading/unloading in the range $0 \leq \lambda \leq \lambda_{cr}$,

$$S_{11} = \frac{\partial T_t}{\partial u_t} = \frac{\alpha_c T_{max}}{\delta_t \lambda_{cr}}, \quad S_{22} = \frac{\partial T_n}{\partial u_n} = \frac{1}{\delta_n} \frac{T_{max}}{\lambda_{cr}}, \quad S_{12} = S_{21} = 0. \quad (\text{B.18})$$

for loading in the range $\lambda_{cr} < \lambda \leq 1$,

$$\begin{aligned} S_{11} &= \frac{\partial T_t}{\partial u_t} = \frac{\alpha_c T_{max}}{\delta_t (1 - \lambda_{cr})} \left(\frac{1 - \lambda}{\lambda} - \frac{\beta_c^2 u_t^2}{\lambda^3 \delta_t^2} \right), \\ S_{22} &= \frac{\partial T_n}{\partial u_n} = \frac{T_{max}}{\delta_n (1 - \lambda_{cr})} \left(\frac{1 - \lambda}{\lambda} - \frac{u_n^2}{\lambda^3 \delta_n^2} \right), \end{aligned}$$

$$S_{12} = S_{21} = \frac{\partial T_n}{\partial u_t} = \frac{\partial T_t}{\partial u_n} = \frac{-\alpha_c T_{max} u_t u_n}{\delta_t \delta_n^2 (1 - \lambda_{cr}) \lambda^3} = \frac{-\alpha_c T_{max} u_t u_n \beta_c^2}{\delta_n \delta_t^2 (1 - \lambda_{cr}) \lambda^3}. \quad (\text{B.19})$$

for unloading/reloading in the range $0 < \lambda \leq \lambda^*$ where λ^* is the maximum value of λ after which unloading started,

$$S_{11} = \frac{\partial T_t}{\partial u_t} = \frac{\alpha_c T_{max}}{\delta_t \lambda^*}, \quad S_{22} = \frac{\partial T_n}{\partial u_n} = \frac{1}{\delta_n} \frac{T_{max}}{\lambda^*}, \quad S_{12} = S_{21} = 0. \quad (\text{B.20})$$

For loading in the range $\lambda^* < \lambda \leq 1$,

$$\begin{aligned} S_{11} &= \frac{\partial T_t}{\partial u_t} = \frac{\alpha_c T_{max}}{\delta_t (1 - \lambda^*)} \left(\frac{1 - \lambda}{\lambda} - \frac{\beta_c^2 u_t^2}{\lambda^3 \delta_t^2} \right), \\ S_{22} &= \frac{\partial T_n}{\partial u_n} = \frac{T_{max}}{\delta_n (1 - \lambda^*)} \left(\frac{1 - \lambda}{\lambda} - \frac{u_n^2}{\lambda^3 \delta_n^2} \right), \\ S_{12} = S_{21} &= \frac{\partial T_n}{\partial u_t} = \frac{\partial T_t}{\partial u_n} = \frac{-\alpha_c T_{max} u_t u_n}{\delta_t \delta_n^2 (1 - \lambda^*) \lambda^3} = \frac{-\alpha_c T_{max} u_t u_n \beta_c^2}{\delta_n \delta_t^2 (1 - \lambda^*) \lambda^3}. \end{aligned} \quad (\text{B.21})$$

APPENDIX C

FINITE ELEMENT SIMULATION OF MODE-I DYNAMIC FRACTURE OF FGM

In this section, finite element simulations of mode-I dynamic fracture of FGM samples are discussed. The numerical model is validated against experiments [17] on mode-I dynamic fracture of monotonically graded FGM made of a syntactic foam. In the following, a few experimental details are provided. Additional details can be found in [17].

C.0.1 Material preparation and characterization

Syntactic epoxy foams of various volume fractions of microballoons were used to make FGM samples. Homogeneous syntactic epoxy foam sheets with randomly distributed microballoons were first prepared. The microballoons used in this investigation were commercially available hollow glass spheres (Untreated type $K - 1$ hollow microballoons from 3M Inc., USA) of mean diameter $\sim 60 \mu\text{m}$ and wall thickness $\sim 600 \text{ nm}$. Low-viscosity epoxy resin (Reformulated (2003) Epo-ThinTM from Beuhler Inc., resin to hardener ratio of 100:36 by weight) was used as the matrix material.

The material preparation consisted of mixing a predetermined amount of microballoon volume fraction into the epoxy material. Several different homogeneous epoxy-microballoon mixtures were prepared for processing graded foams. Nine different mixtures with volume fraction of microballoons V_F ranging from 5 % to 45 % in steps of 5 % were prepared separately. The microballoons were carefully stirred into the epoxy resin while avoiding air bubbles and agglomeration. Stirring the mixture was continued until the mixture showed a tendency to gel and then poured into molds. This helped to eliminate any buoyancy

induced floatation of microballoons during subsequent curing. The mixture with the lowest volume fraction of microballoons was poured first into the mold followed by the next higher volume fraction, and so on. Each layer was nominally 5 mm thick. A complex interplay of buoyancy and viscous forces on the microballoons along with thermal convection during polymerization resulted in a nearly linear volume fraction gradient. The gradient extended over approximately 45 mm, between a region of nearly pure epoxy at one end and microballoon-rich epoxy on the other. The overall specimen dimensions were 152 mm x 45 mm x 8 mm.

The schematic of the sample is shown in Fig. C.1(a). The longitudinal (C_L) and shear (C_S) wave speeds of these sheets were determined using ultrasonic pulse-echo method, (see Ref. [24] for details). The values of elastic moduli (E) and Poisson ratio (ν) were then determined using measured wave speeds and mass density. The resulting elastic modulus and mass density variations with volume fraction of microballoons are shown in Fig. C.1(b). Both quantities reduce monotonically with microballoon volume fraction over the entire range. The values of Poisson's ratio in these compositions were found to be nearly constant ($\nu = 0.35 \pm 0.02$).

Mode-I crack initiation toughness tests were also conducted on homogeneous compositions. Beam samples (152 mm \times 27 mm and 7.5 mm thickness) were prepared from homogeneous syntactic foam sheets with different microballoon volume fractions (0, 5 %, 15 %, 25 %, 35 % and 45 %). Edge crack of length 5.4 mm ($a/W=0.2$) was cut along the mid-span in each of these samples. The Dally-Sanford single strain gage method [76] was used to obtain dynamic stress intensity factor for each homogeneous syntactic foam sample. A strain gage of gage length 0.8 mm (CEA-13-032WT-120 from Vishay-Micromeritics

Group, Inc.) was located radially at a distance of 4 mm from the crack tip and at an angle of 60° to the crack orientation. These specimens were impact loaded (impact velocity = 2 m/s) in 3-point bend configuration. The strain history recorded by the strain gage is used to obtain the crack initiation toughness value of each sample. Details are avoided here for brevity and can be found elsewhere [77]. Figure C.1(c) shows the variation of mode-I dynamic initiation toughness (K_{ICR}) with microballoon volume fraction. A monotonic reduction in the crack initiation toughness values with volume fraction can be seen from this figure. Approximately a 50% reduction in fracture toughness can be noted when microballoon volume fraction increases from 0 to 45%.

C.0.2 Experimental results

Experiments on graded foam FGM samples included two types, (a) a crack on the compliant side of the sample with impact occurring on the stiffer side and (b) a crack on the stiffer side of the sample with impact occurring on the compliant side. Denoting the elastic modulus of the edge of the cracked sheet behind the crack tip as E_1 , and the one ahead of the crack as E_2 , the former corresponds to $E_1 < E_2$ and the latter to $E_2 > E_1$. The Coherent Gradient Sensing (CGS) method was used in conjunction with high-speed photography [30] in this study to perform real-time measurements of instantaneous surface deformations around the crack tip. The details about the method are explained in Chapter 2.

The resulting interference fringes for the two cases are shown in Fig. C.2(a) and (b). For each case, the representative interferograms corresponding to pre- and post-initiation time instants are included. The crack initiation occurred at $t = 115 \mu\text{s}$ after impact for

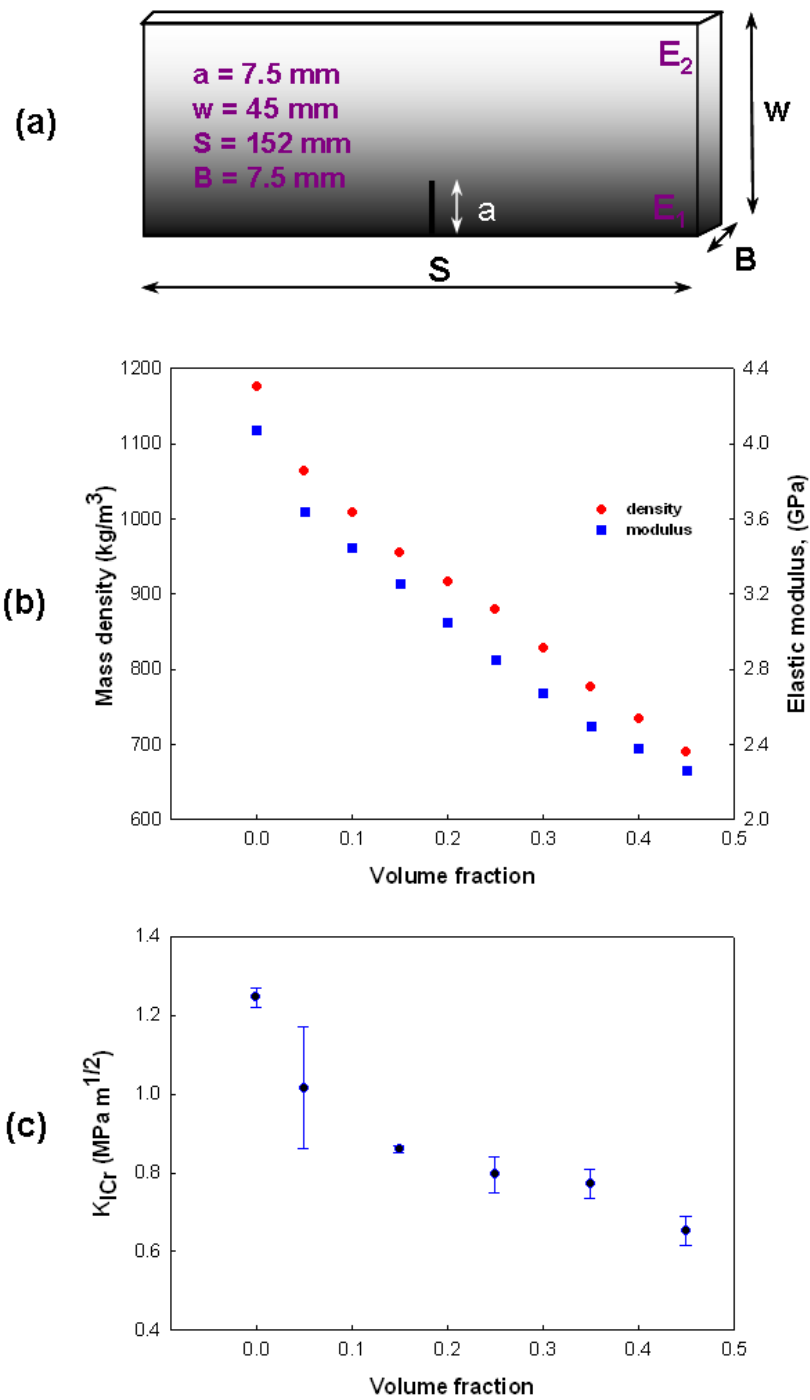


Figure C.1: (a) Schematic of the FGM specimen, (b) Material properties variation along the width of the sample and (c) Variation of dynamic crack initiation toughness along the width of the sample.

$E_1 < E_2$ and $t = 135 \mu\text{s}$ after impact for $E_1 > E_2$. The legends correspond to the time instant at which the image was recorded after impact. At earlier times severe concentration of interference fringes are seen at the impact location (near the top edge) while only a few fringes are seen at the crack tip (near the bottom edge). With the passage of time crack tip deformations increase, as evidenced by an increasing number of fringes at the crack tip, followed by crack initiation and growth. The fringe pattern in each case is symmetric on either side of the crack, indicating mode-I crack tip deformations.

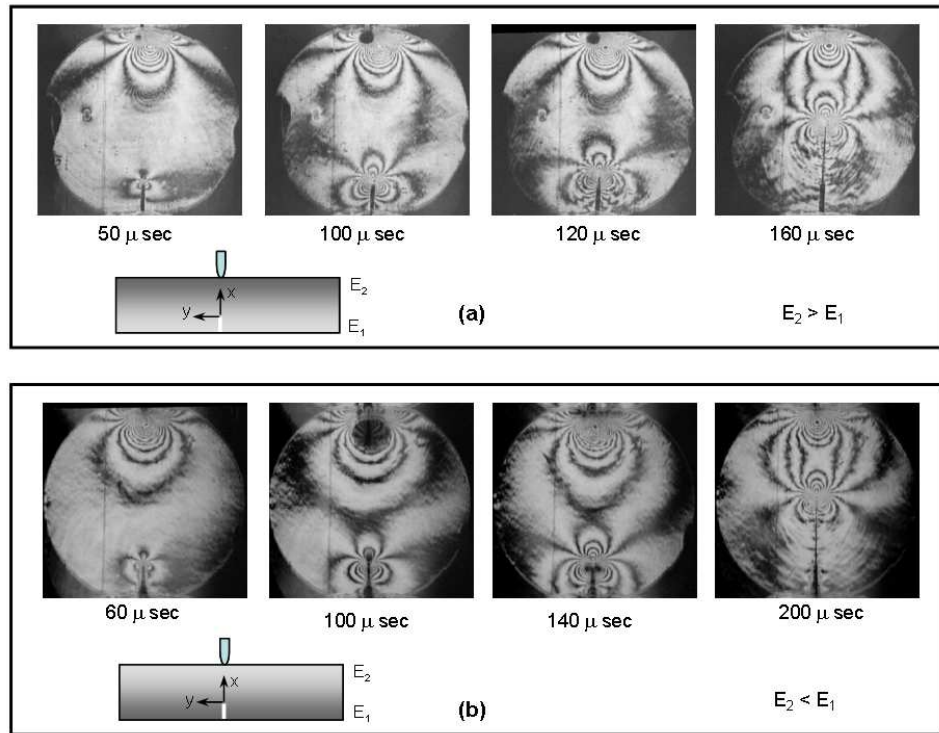


Figure C.2: Selected CGS interferograms representing contours of $\delta w/\delta x$ in functionally graded epoxy syntactic foam sheet impact loaded on the edge opposing the crack tip. (The vertical line is at a distance of 10 mm from the crack.) (a) Crack on the compliant side $E_1 < E_2$, (b) crack on the stiffer side $E_1 > E_2$. Fringe sensitivity $\sim 0.015^\circ$ /fringe.

C.0.3 Modeling details

The overall view of the finite element mesh is shown in Fig. C.3(a). The dimensions of the notch (150 μm root radius) was also modeled in the simulations as can be seen from Fig. C.3(b). The cohesive elements were inserted along a line in which the crack is allowed to propagate can be seen from this figure. The smallest element size used in the mesh was less than the characteristic cohesive length scale (see Section 7.1). The sample was modeled as a free-free beam and a velocity of 5 m/sec was imposed on the node located at the impact point. The variations of elastic modulus, E (4.2 GPa to 2.1 GPa) and mass density ρ (1175 kg/m³ to 690 kg/m³) were approximated by linear functions and applied to the model as explained in Section 7.2. The variation of mode-I fracture energy G_I computed from experimentally obtained variation of crack initiation toughness was applied to cohesive elements as detailed in Section 7.3. The peak stress T_{max} was assumed as $E(X)/100$, and the values for α_c and β_c are chosen as 1.0.

C.0.4 Finite element results

Snapshots of crack tip normal stresses before and after crack-initiation are shown in Figs. C.4(a) and (c) for the case of a crack on the compliant side ($E_1 < E_2$). Similar results for the opposite configuration are shown in Figs. C.4(b) and (d). The stress contours are symmetric on either side of the crack indicating mode-I deformation in both cases. The stress levels seem to decrease once the crack initiates in case of $E_1 > E_2$ since the crack is growing into a microballoon-rich region in this case. The opposite trend is observed in the other configuration. Instantaneous crack length histories for both cases of monotonically graded foam sheets are shown in Figs. C.5(a) and (b). The crack initiation occurs earlier

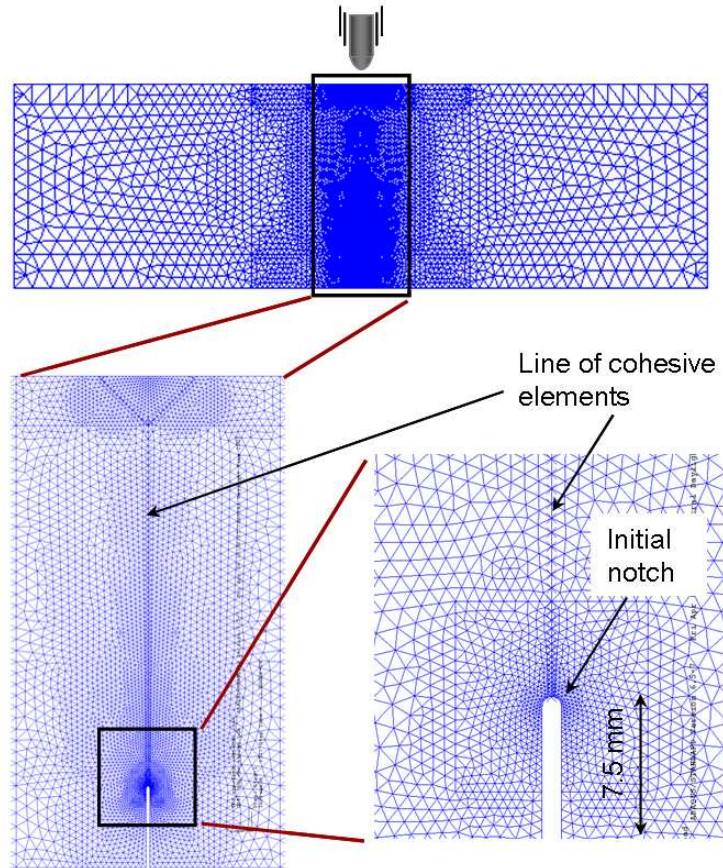


Figure C.3: Finite element mesh used for the analysis

in case of the specimen with a crack on the compliant side ($E_1 < E_2$) when compared to the one with a crack on the stiffer side ($E_1 > E_2$). The crack initiation times in simulations are $106 \mu\text{s}$ and $127 \mu\text{s}$ for $E_1 < E_2$ and $E_1 > E_2$, respectively against $115 \mu\text{s}$ and $135 \mu\text{s}$ observed experimentally. Higher crack speeds were observed for the case of $E_1 < E_2$ both in experiments as well as in simulations. The crack speeds observed in experiments (calculated from the central difference method) are 357 m/s and 273 m/s for the case of $E_1 < E_2$ and $E_1 > E_2$, respectively. The corresponding values in simulations are 385 m/s and 278 m/s . Thus, the trends observed in crack speeds are preserved in simulations.

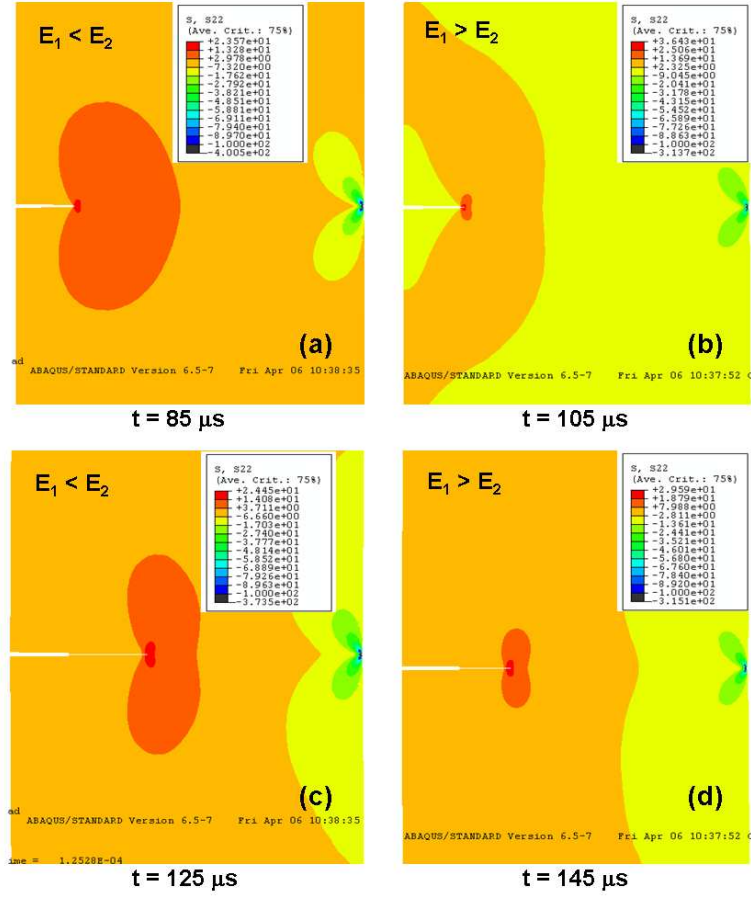


Figure C.4: Snapshots of σ_{yy} stress field at two different time instants, (a) $85 \mu\text{s}$ and (b) $125 \mu\text{s}$ for $E_1 < E_2$ (crack initiation time = $106 \mu\text{s}$), and (c) $105 \mu\text{s}$ and (d) $145 \mu\text{s}$ for $E_1 > E_2$ (crack initiation time = $127 \mu\text{s}$).

The evolutions of various energy components was also studied. The evolution of strain energy (U_{SE}) and kinetic energy (U_{KE}) are shown in Fig. C.6(a). Similar to the results presented in Section 7.4.1, both U_{SE} and U_{KE} increase rapidly for the case of $E_1 < E_2$. The energy dissipated by the cohesive elements (U_{CE}) is shown in Fig. C.6(b). A rapid change in the slope of U_{CE} curve at $t \sim 106 \mu\text{s}$ for $E_1 < E_2$ ($t \sim 127 \mu\text{s}$ for $E_1 > E_2$)

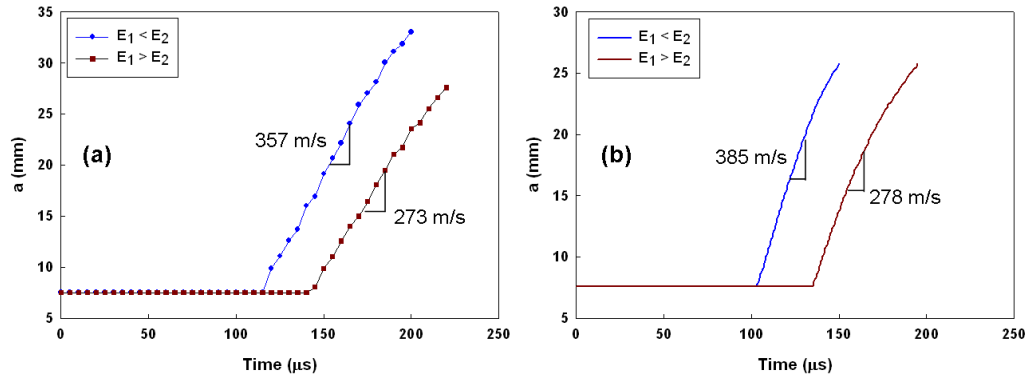


Figure C.5: Crack growth behavior in syntactic foam FGM samples under mode-I loading. absolute crack length history from (a) experiments and (b) finite element simulations.

signifies crack initiation. Also as noted earlier in the Section 7.4.1, the higher crack speed for the case of $E_1 < E_2$ is associated with a rapid accumulation of energies U_{SE} and U_{KE} .

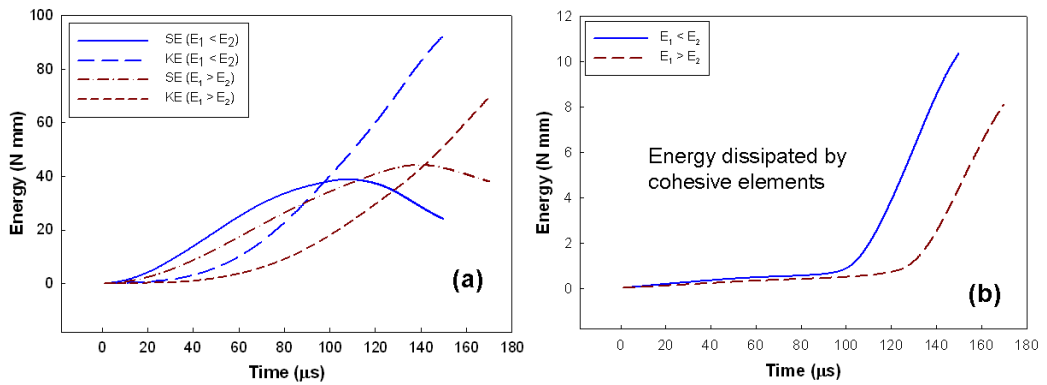


Figure C.6: Evolution of various energies in mode-I dynamic simulation for both FGM configurations: (a) kinetic energy and strain energy and (b) energy dissipated by cohesive elements